



CHALMERS
UNIVERSITY OF TECHNOLOGY

Novel Dilute Bismide, Epitaxy, Physical Properties and Device Application

Downloaded from: <https://research.chalmers.se>, 2024-04-23 12:48 UTC

Citation for the original published paper (version of record):

Wang, L., Zhang, L., Yue, L. et al (2017). Novel Dilute Bismide, Epitaxy, Physical Properties and Device Application. Crystals, 7(3): Article no 63 -. <http://dx.doi.org/10.3390/cryst7030063>

N.B. When citing this work, cite the original published paper.

Review

Novel Dilute Bismide, Epitaxy, Physical Properties and Device Application

Lijuan Wang ^{1,*}, Liyao Zhang ¹, Li Yue ¹, Dan Liang ², Xiren Chen ³, Yaoyao Li ¹, Pengfei Lu ², Jun Shao ³ and Shumin Wang ^{1,4,*}

¹ Shanghai Institute of Microsystem and Information Technology, Chinese Academy of Sciences, 865 Chang Ning Road, Shanghai 200050, China; lyzhang@mail.sim.ac.cn (L.Z.); yueli@mail.sim.ac.cn (L.Y.); yyli@mail.sim.ac.cn (Y.L.)

² Beijing University of Posts and Telecommunications, Xitucheng Road, Haidian District, Beijing 100089, China; liangdan@bupt.edu.cn (D.L.); photon@bupt.edu.cn (P.L.)

³ Shanghai Institute of Technical Physics, Chinese Academy of Sciences, 500 Yu Tian Road, Shanghai 200083, China; xrchen@mail.sitp.ac.cn (X.C.); jshao@mail.sitp.ac.cn (J.S.)

⁴ Department of Microtechnology and Nanoscience, Chalmers University of Technology, Gothenburg 458 93 58-34, Sweden

* Correspondence: wangljmbe@163.com (L.W.); shumin@mail.sim.ac.cn (S.W.)

Academic Editor: Paul J. Simmonds

Received: 1 December 2016; Accepted: 15 February 2017; Published: 24 February 2017

Abstract: Dilute bismide in which a small amount of bismuth is incorporated to host III-Vs is the least studied III-V compound semiconductor and has received steadily increasing attention since 2000. In this paper, we review theoretical predictions of physical properties of bismide alloys, epitaxial growth of bismide thin films and nanostructures, surface, structural, electric, transport and optic properties of various binaries and bismide alloys, and device applications.

Keywords: dilute bismide; III-N-Bi; III-P-Bi; III-As-Bi; III-Sb-Bi; MBE; MOCVD; surfactant; droplet; bandgap reduction; GaAsBi lasers; In(Ga)AsBi detectors; InSbBi detectors

1. Brief History of Epitaxial Growth of Dilute Bismides

Bismuth (Bi) has been known since ancient times but was identified for the first time as a distinct element from lead and tin by Claude Francois Jeoffroy in 1753. It possesses an atomic number of 83 in the Periodic Table and has been considered to be non-radioactive until 2003 when French astrophysicists discovered an extremely long half-life of 1.9×10^{19} years (the age of our universe is about 1.4×10^9 years for comparison) via-decay [1]. Bismuth has been used traditionally in fuse, thermoelectric products, cosmetics and medicine, etc. Surprisingly, the toxicity of Bi is even less than table salt (NaCl) [2] and it is therefore regarded as green element compared with its neighboring heavy metals like lead (Pb), antimony (Sb), arsenic (As) and mercury (Hg), etc. [3]. For this sustainability reason, Bi has recently attracted great attention to replace the toxic lead products in industry [4], and the price for Bi mine production has increased five times since 2000 [1]. While Bi is the last element in the group-V column in the Periodic Table, it has been largely neglected as a member of the III-V compound semiconductor family which plays a significant role in modern electronic and optoelectronic device applications nowadays. This is, to large extent, due to the difficulties in synthesizing high quality binary III-Bi crystals and alloying Bi into host III-Vs, which will be one of the main topics of this review paper. Synthesis of InBi alloy dates back to 1950s [5,6] and the X-ray crystallographic analysis revealed a PbO crystal structure, in contrast to the zinc-blende (ZB) structure found in majority III-V crystals. Perhaps the first interest to incorporate Bi into III-Vs was stimulated by the isoelectronic trap discovered in O-doped ZnTe in 1962 [7] and later in N-doped GaP in 1965 [8]. When the substituted

Group-V element has a large difference in electronegativity (3.04, 2.19, 2.18, 2.05 and 2.02 in Pauling scale for N, P, As, Sb and Bi, respectively) with respect to the host Group-V element, isoelectronic traps can be formed. The incorporation of N in GaP forms traps for electrons with an impurity energy level close to the GaP conduction band (CB) [8]. The charged N_P can bind a hole through Coulomb interaction forming a bound exciton emitting bright orange luminescence with energy below the bandgap of GaP. When Bi is incorporated in GaP, the Bi_P isoelectronic atom traps a hole with a trapping energy close to valence band (VB) and becomes charged [9]. It then attracts an electron forming a bound exciton and showing the similar effect in luminescence. Such an isoelectronic trap effect was verified also in Bi-doped InP later [10]. In these samples, the Bi concentration is in the doping level of below 10^{18} cm^{-3} . Sharp bound exciton and phonon assisted photoluminescence (PL) signals are observed at low temperatures.

The discoveries of promising physical properties of InSb [11,12] and HgCdTe [13] with a low bandgap energy for mid- and long-wavelength infrared (IR) photodetector applications in the 1950s had encouraged researchers to seek for other compound semiconductors for $\lambda > 8 \mu\text{m}$. An intuitive strategy is to look at heavy atoms such as Bi and Tl which possess semi-metallic property. Jean-Louis et al. from France Telecom made the first attempt on incorporating Bi into (111) plane InSb of 3 mm in diameter by Czochralski technique using a resistance heating furnace in late 1960s [14–16]. Up to $x = 2.6\%$ Bi was found to be incorporated in $\text{InSb}_{1-x}\text{Bi}_x$. The cutoff wavelength moves from $5.5 \mu\text{m}$ for InSb to $8.3 \mu\text{m}$ for $\text{InSb}_{1-x}\text{Bi}_x$ with $x = 2.2\%$ at 77 K [14]. Polycrystalline InSbBi bulks were also demonstrated later from several groups [17–19]. Zilko and Greene used multitarget RF sputtering to synthesize single-crystal metastable InSbBi bulk on (110) GaAs substrates [20] and studied phase stability. The first InSbBi single crystal thin film evidenced by unambiguous X-ray diffraction was reported by Oe et al. from Japan on (100) InSb substrates using molecular beam epitaxy (MBE) in 1981 [21]. Bismuth was incorporated only under the In-rich growth condition and up to 5% Bi concentration was demonstrated when grown at 250°C . However, crystal surface was covered by In/Bi droplets, and the growth window for achieving InSbBi with both good surface and structural quality is very narrow. Clear wavelength red-shift was observed from InSbBi alloy annealed at 420°C in photovoltaic response at 100 K, confirming the bandgap reduction after Bi incorporation.

Oe's work has unfortunately not received immediate interest in the research community. In the next 20 years or so, only a few works using MBE were sporadically reported [22,23]. There were some investigations using metalorganic chemical vapor deposition (MOCVD) [24–29], starting from ternary $\text{InAs}_x\text{Sb}_{1-x}$, which has the lowest bandgap of 0.1 eV and 0.145 eV at 300 K and 77 K for $x = 0.4$, respectively, and pushing toward long absorption wavelengths by adding Bi. Humphreys et al. from North Carolina State University in US reported the first MOCVD growth of InAsSbBi with a maximum Bi content of 4% in 1988 [24]. Ma et al. demonstrated the first successful growth of $\text{InAs}_{1-x}\text{Bi}_x$ ($x \leq 2.6\%$) [25]. Clear PL peak shifts were observed with Bi composition at 10 K and a bandgap reduction of 55 meV/% Bi was deduced for InAsBi. Lee et al. from Northwestern University in US reported InSbBi/InSb heterostructure photodetectors [30]. The voltage responsivity at $10.6 \mu\text{m}$ was about 1.9 mV/W at 300 K, corresponding to the Johnson noise limited detectivity of $1.2 \times 10^6 \text{ cmHz}^{1/2}/\text{W}$. A comprehensive review on early work on III-Sb(Bi) and device applications can be found in reference [31]. Later, Oe and Okamoto reported the new semiconductor alloy of $\text{GaAs}_{1-x}\text{Bi}_x$ with $x = 2\%$ by MOCVD in 1998 [32]. PL was observed at 10–300 K and the PL peak energy was found to be relatively insensitive to temperature: 0.1 meV/K. Meanwhile, there was also some interest in using Bi to compensate for a high and intrinsic *p*-type background in GaSb substrates due to the defect formation of $\text{Ga}_{\text{Sb}}\text{V}_{\text{Sb}}$ in liquid phase epitaxy (LPE) [33–36]. For example, Chaldishchev et al. from Ioffe Institute in Russia demonstrated a *p*-type background reduction from 10^{17} cm^{-3} to a few 10^{15} cm^{-3} by adding 10^{19} cm^{-3} Bi in GaSb during the LPE growth [35]. The mechanism is that Bi incorporation efficiently reduces Sb-vacancies and thus minimizes the antisite Ga_{Sb} defects which are the origin of the high *p*-type background in GaSb.

A renaissance in dilute bismide research that started in the early 2000s catalyzed by the paper by Mascarenhas et al. addressing the issue of isoelectronic co-doping in GaAs [37]. In 1992 Weyers et al. and Bailargeon et al. discovered a giant bandgap bowing effect in GaAsN [38] and GaPN [39], respectively. A bandgap reduction as large as 150 meV/% N was found [40]. This unusual property was later employed by Kondow et al. Hitachi Central Laboratory in Japan for making uncooled 1.3 and 1.55 μm telecom InGaAs quantum well (QW) lasers on GaAs substrates [41], since commercial telecom lasers based on InGaAsP QWs on InP substrates have a low characteristic temperature and an external cooler is required for laser operation. However, incorporation of N in GaAs significantly degrades transport [42] as well as optical properties [43]. The degradation is associated with the N impurity band formation causing GaNAs behaving like a highly N-doped semiconductor rather than a dilute nitride alloy [37]. In 2001, Mascarenhas et al. [37] proposed using isoelectronic co-doping of N and Bi in GaAs to restore regular alloy behavior, thus overcoming limitations of semiconductor alloy design. One year later, Tixier et al. successfully demonstrated strong room temperature PL from $\text{GaAs}_{1-x}\text{Bi}_x$ ($x \leq 3.1\%$) grown by MBE and discovered a giant bandgap reduction of 84 meV/% Bi [44]. The promising results mimicking that found in GaNAs [38] and GaNP [39] has spurred research community to pay attention to this novel bismide alloys. As N and Bi mainly affect CB and VB of III-Vs, respectively, it is convenient to tune electronic property of electrons and holes independently. Compensation of atomic size of N and Bi in III-Vs mitigates the lattice mismatch problem and offers a large degree for strain engineering. The interest for GaAs(N)Bi alloy has increased since 2005, with extensive investigations of GaAs(N)Bi followed by searching for other dilute bismide in recent years. Figure 1 shows number of publications on dilute bismide since 1997. The number has increased at an accelerated pace in recent years. An annual dedicated international workshop on Bi containing compounds was initiated in 2010, and the first book specialized on Bi containing compounds was published in 2013 [45].



Figure 1. Chronic evolution of number of publications on dilute bismide since 1997.

Initial interest in dilute bismide for device applications focused on InSbBi and InAsSbBi with the hope of making mid-wavelength IR photodetectors in the 1970s–90s. After the discovery of the giant energy bowing effect in GaAsBi [44], it was realized that Bi incorporation can effectively reduce the bandgap of GaAsBi and increase VB offset of GaAsBi/GaAs. When both N and Bi are used, it is possible to independently control CB and VB in GaAsNBi, and thus extend light emission wavelength very efficiently. Other beneficial properties when using Bi include large spin-orbit (SO) split

band [46,47], less temperature sensitive bandgap [32,48,49], minor influence on both electron [50] and hole mobility [51] for small Bi concentrations, enhancement of PL intensity [44] and surfactant effect ensuring smooth surface [52], etc. Sweeney and Jin proposed theoretically that GaAsNBi is promising for efficient near IR light emitting devices [53]. When the SO split energy is larger than the bandgap, Auger recombination involving holes in the SO and the heavy-hole band and inter-valence band absorption (IVBA) will be suppressed, which is expected to improve high-temperature performance and thermal stability of light emitting devices. This is of technological importance for making uncooled telecom lasers on GaAs substrates. Current commercial telecom lasers employ InGaAsP QWs on InP substrates and require external coolers which significantly increase energy consumption and are also expensive. When incorporating Bi into InGaAsSb, it is beneficial to increase VB offset to avoid hole leakage, which is a severe problem limiting wavelength extension in the regime of $>3\ \mu\text{m}$ in type-I InGaAsSb QW lasers used for various gas sensing. The first electrically pumped GaAsBi QW laser was demonstrated within the EU FP-7 BIANCHO project in 2013 [54]. The lasing wavelength was 947 nm at 300 K.

In this paper, we intend to provide an overview of recent advancements on dilute bismide and influence of Bi on III-V alloys. In the following sections, we will present theoretical modeling of crystal and electronic properties of dilute bismide and Bi clusters, epitaxial growth and physical properties of various III-V-Bi alloys, influence of Bi on III-V surface and nanostructures and device applications using dilute bismide. A conclusion with some future outlooks will be given at the end.

2. Theoretical Prediction

For III-V compounds, there are a variety of theoretical models and simulations about predicting their physical properties. Comprehensive researches on III-V ZB and wurtzite (WZ) compound semiconductors have been performed over the years and reviewed in plenty of existing literatures [55–57]. This Section mainly focuses on theoretical simulations of structural and electronic properties of dilute bismides which have provided valuable understandings and insights for explaining many phenomena observed in dilute bismides. Among those reliable computational methods, the most popular one is the first principle calculation. Besides, empirical models, such as $\mathbf{k}\cdot\mathbf{p}$ band method, tight binding (TB) model and band anticrossing (BAC) theory, are also effective to give explanations in practice. All these methods and computational techniques have been used to various types of Bi-containing structures including surfaces, thin films, nanostructures and clusters. In Section 2.1, empirical models for electronic band properties are presented. In Section 2.2, we discuss structural, electronic and optical predictions by first principle calculations. In Section 2.3, some other methods are presented.

2.1. Empirical Models for Electronic Band Properties

This section is limited to describe different empirical models such as BAC or valence-BAC (VBAC), TB and $\mathbf{k}\cdot\mathbf{p}$ band models, which are all based on solving the Hamiltonians. Briefly speaking, the BAC (VBAC) model is mostly used when impurity states are involved, and the TB model is constructed using the atomic orbitals while the $\mathbf{k}\cdot\mathbf{p}$ band model includes the CB, heavy hole (HH), light hole (LH) and SO split-off band around some high symmetry points in reciprocal space, e.g., the Γ -point. More detailed descriptions of these models can be found elsewhere. A brief summary of the practical usage in Bi-containing III-V systems is given in Table 1.

Table 1. Summary of the empirical models and their usages in Bi-containing III-V systems.

Method	Electronic Properties	Optical Properties
BAC/VBAC Model	GaAs _{1-x} Bi _x [58–60]	GaAs _{1-x} Bi _x [58,59] GaAsBiN=
	GaAsBiN [53]	InGaAs _{1-x} Bi _x [61,62]
	GaBi _x As _{1-x} /GaAs [63]	In _{0.53} Ga _{0.47} Bi _x As _{1-x} /InP [64]
	InP _{1-x} Bi _x [65]	
	InSb _{1-x} Bi _x [66]	
	InGaAs _{1-x} Bi _x [61,62] In _{0.53} Ga _{0.47} Bi _x As _{1-x} /InP [64]	
TB Model	GaP _{1-x} Bi _x , GaAs _{1-x} Bi _x [67] GaAs _{1-x} Bi _x [68,69]	GaAs _{1-x} Bi _x [67]
k·p Model	GaAs _{1-x} Bi _x [58,70]	
	GaBi _x As _{1-x} /GaAs [63]	
	InGaAs [71]	
	InGaAs _{1-x} Bi _x [72]	

2.1.1. BAC/VBAC Model

The BAC/VBAC model has been successfully used in dilute isoelectronic semiconductors with a large difference in electronegativity to explain large energy bandgap bowing and provides a useful and reliable basis for describing a variety of material properties, based on an interaction between the CB or VB edge and the higher-lying localized isoelectronic resonant states. This model always combines with experimental data to give the interaction strength. For example, the experimental data of GaAsBiN alloys on GaAs [53,59] and that of InGaAsBi alloys on InP [61,62] were used in the model to account for the reduction of bandgap as well as an increase in the SO split energy with increasing Bi concentration. Such a reduction results from interaction between extended states of the host alloy and the localized states of the Bi impurities [59]. The dilute bismide alloys can present $\Delta_{SO} > E_g$ condition, which is an optimal condition to suppress non-radiative CHSH (Conduction-Heavy hole Spin-orbit-Heavy hole) Auger recombination and IVBA, and to improve the performance in high temperature and thermal stability of light emitting devices [53,59,61,62]. Carrier mobility and concentrations for the In_yGa_{1-y}Bi_xAs_{1-x} system have also been computed with this model [62].

The VBAC model is obtained by using the BAC model to the VB structure. This model predicts that the extended states of the host semiconductor hybridize with the localized defect states introduced by the minority species of large atomic radii and induce a restructuring of the VB. Bismuth, as the largest stable group-V element, is expected to introduce impurity levels, as in the case of the BAC model mentioned above. If an anticrossing interaction occurs, it will be between the Bi-related impurity levels and the VB edge of the host matrix. It has been proposed that the band structure of GaBi_xAs_{1-x} can be explained in terms of a VBAC interaction by Alberiet et al. [59]. Wu et al. [65] have investigated the bandgap bowing and SO split energy of InP_{1-x}Bi_x using the VBAC model and the results show a good agreement with the experimental data.

2.1.2. TB Model

The tight binding model naturally deals with finite device sizes, alloy disorder, and hetero-interfaces due to the local basis representation which results in very sparse matrices and minimal requirements of storage and processor communication. Usman et al. [67] have developed a model based on the valence force field (VFF) and sp^3s^* TB methods to calculate dilute bismide alloys GaBi_xAs_{1-x} and GaBi_xP_{1-x}. Their results show the evolution of the highest valence state in GaBi_xY_{1-x} (Y = P, As). Strong bandgap reduction and change of CB edge energy could be predicted using a BAC model. Virkkala et al. [68] have investigated GaAs_{1-x}Bi_x alloys including the SO coupling in the TB model for directional Bi-Bi interaction. The results indicate that Bi states mix with host material states.

The states near the VB edge agglomerate along the zigzag chains which are due to Bi-Bi interactions in a random alloy, an energy broadening in these states and the bandgap narrowing.

By comparing atomistic TB results with room temperature (RT) photorefectance (PR) measurements, Usman et al. [69] investigated alloy disorder effect on electronic structure of compressively strained $\text{GaAs}_{1-x}\text{Bi}_x$ samples on GaAs (100) substrate. The atom positions in alloy are determined using a VFF strain energy minimization scheme. Their theoretical results are in good agreement with the experimental data and reproduce the crossover at 9% Bi composition, beyond which Δ_{SO} exceeds the bandgap, E_g , and suggests a type-I band alignment at the interface between $\text{GaAs}_{1-x}\text{Bi}_x$ and GaAs.

2.1.3. The $\mathbf{k}\cdot\mathbf{p}$ Model

Typical eight-band $\mathbf{k}\cdot\mathbf{p}$ model is used to analyze the electronic structure of conventional semiconductor lasers, which includes the CB, HH, LH and SO split-off bands. By adding additional spin-degenerate impurity-related states to the eight-band $\mathbf{k}\cdot\mathbf{p}$ model, the 10-band, 12-band and 14-band $\mathbf{k}\cdot\mathbf{p}$ models can be obtained, which are used for GaInNAs with 10 bands [71], $(\text{In})\text{GaBi}_x\text{As}_{1-x}$ with 12 bands [72] and $\text{GaBi}_x\text{N}_y\text{As}_{1-x-y}$ with 14 bands [73] models, respectively. Fluegel et al. [70] studied electron effective mass of *n*-type $\text{GaAs}_{1-x}\text{Bi}_x$ in the range of $0\% < x < 0.88\%$ using magnetic field and temperature dependent resistivity measurements and the $\mathbf{k}\cdot\mathbf{p}$ formalism. The overall decrease in electron effective mass is obtained and giant bandgap bowing and giant SO bowing effects agree with the perturbation theory.

2.1.4. Combination of Empirical Models

Combining the BAC model with the $\mathbf{k}\cdot\mathbf{p}$ theory [58], a rapid reduction in bandgap with increasing Bi concentration and a very large SO split energy is predicted, and the gain and loss characteristics of ideal dilute nitride and bismide lasers should be at least as good as those of conventional InP-based telecom lasers for $\text{GaAs}_{1-x}\text{N}_x$ and $\text{GaAs}_{1-x}\text{Bi}_x$. Experimentally, optical spectroscopic techniques were used to explore the optical properties of $\text{In}_{0.53}\text{Ga}_{0.47}\text{Bi}_x\text{As}_{1-x}/\text{InP}$. Trying to achieve $\Delta_{\text{SO}} > E_g$ and a reduced temperature dependence of E_g are of great significance for suppressing recombination losses and improving performance in mid-IR photonic devices.

Samajdar et al. [66] used the VBAC model combining with the $\mathbf{k}\cdot\mathbf{p}$ formalism to investigate VB structure of $\text{InAs}_{1-x}\text{Bi}_x$ and $\text{InSb}_{1-x}\text{Bi}_x$ alloy systems. The bandgap reduction results agree fairly well with the experimental data. The upward shifts in the heavy/light hole E_+ level and SO split-off level $E_{\text{SO}+}$ are observed in both cases. This upward movement of the E_+ band is primarily responsible for the bandgap reduction in these Bi containing alloys. Later they [74] used a mathematical model based on Quantum Dielectric Theory (QDT) to calculate the direct bandgap, E_0 , of Bi-containing ternary alloys. The variation of E_0 with x for $\text{InSb}_{1-x}\text{Bi}_x$ and $\text{GaSb}_{1-x}\text{Bi}_x$ is in a good agreement with the experimental results. The composition dependence of E_0 at different temperatures is also found for some other ternary alloys like InPBi and AlSbBi.

2.2. Structural, Electronic and Optical Properties Predicted by First Principle Calculations

2.2.1. Structural Property

Thin Films—Binary III-Bi Compounds

The cubic III-Bi compounds: BBi, AlBi and GaBi have been studied extensively. Belabbes et al. [75] computed structural and lattice-dynamic properties for these alloys using a plane wave ultrasoft Vanderbilt pseudopotential as implemented in the PWscf code. Besides, the computed born effective charge and longitudinal optical-transverse optical (LO-TO) splitting of BBi show an increase trend with rising pressure. Madouri et al. [76] performed first principle calculations using the full potential linearized augmented plane wave (FP-LAPW) method as implemented in the WIEN2k code to

investigate structural and electronic properties. The ground state of ZB structure phase and band structure of BBi show unique features like a strong p - p mixing of the VB maximum (VBM).

GaAs_{1-x}Bi_x

Cubic GaAsBi ternary alloys were studied by Reshak et al. [77] with varying Bi concentrations. The structural and electronic properties were calculated using the FP-LAPW method. Nonlinear variation with Bi concentration is found for lattice constant, bulk modulus, bandgap and SO split-off band. Besides, the SO coupling effect is significant for the bowing but negligible for the bonding. The same properties with the ZB type structure of GaAs_{1-x}Bi_x were also calculated by Abdiche et al. [78], where the strong nonlinear dependence of the Bi composition was also shown.

Study of thermodynamics of Bi incorporation into GaAs lattice structure was performed by Jacobsen et al. [79] using the Vienna Ab-initio Simulation Package (VASP). The formation energy of Bi in both bulk and epitaxial GaAs are obtained by local density approximation (LDA), generalized gradient approximation (GGA), the hybrid function of Heyd, Scuseria and Ernzerhof (HSE) with and without SO coupling included. If Bi metal formation is inhabited and the system is forced to remain constrained to the GaAs_{1-x}Bi_x structure, the equilibrium solubility of epitaxial GaAs_{1-x}Bi_x could be greatly enhanced, yielding a Bi solubility of $x = 0.083$.

InAs_{1-x}Bi_x and InSb_{1-x}Bi_x

The Bi-containing narrow-gap III-V semiconductors are potential candidates for near and mid-IR optoelectronic device applications. Many theoretical works have been carried out for these materials such as InPBi, InAsBi and InSbBi. In 1988, Berding et al. [80] used Harrison's model to study the above mentioned ternary bismides. The bond length, bond energy, elastic constants are estimated and scaled. The mixing enthalpy, miscibility gaps, and critical temperatures are obtained and the prediction that InPBi is the hardest and the most difficult material to synthesize is concluded.

AlN_{1-x}Bi_x

Mbarki et al. investigated structural, electronic and optical properties of AlN_{1-x}Bi_x [81,82] alloys using the WIEN2k code. With increasing Bi composition, the lattice constant deviates from the value obtained by Vegard's law and the bandgap decreases. It remains a semiconductor until $x = 0.5$ and becomes a semimetal for x greater than or equal to 0.625. It displays a strong bandgap bowing parameter and a transition from indirect (AlN) to direct (AlNBi) band gap at x close to 0.02.

InP_{1-x}Bi_x

Structural and electronic properties of InPBi alloys have been systematically investigated by Lu et al. [73] using the first-principle calculations. The alloys with seven different configurations are considered and the formation energy is studied to investigate the relative stability. The insertion of Bi atoms leads to hybridization of s - p among In-5s, P-3p and Bi-6p states and In/P/Bi p states which have significant contributions to the strength of covalent bonding and around the Fermi level. The bandgap of InPBi shrinks clearly with increasing Bi concentration and the band edge shifts when the SO coupling is considered. In addition, their results show that the biaxial strain is an effective method to tune the electronic properties of the system. Later they also investigate the hetero-antisite defects in InP:Bi alloy. The results show that the hetero-antisite defects Bi_{In} is energetically easier than Bi_P and has not significantly contributed to the reduction of the bandgap of InP:Bi alloy [83].

Surface

The initial incorporation processes of Bi on GaAs (100) (2×1) and (2×4) surfaces [84], and GaAs (001)-c(4×4) surface [85] were studied using the ab initio-based approach. For Bi/GaAs(100) (2×1) and (2×4) surfaces, the band structure, density of states (DOSs), and the surface core-level

shifts (SCLS) for the group-V dimers (Bi-Bi, Bi-As and As-As) are all calculated and analyzed to give a stabilizing mechanism responsible for formation of the peculiar (2×1) reconstruction, and to conform the building blocks (corresponding to Bi-As and Bi-Bi dimers) and the atomic origins of the SCLS of the Bi 5*d* photoemission spectra for the Bi/GaAs(100) (2×4) - $\alpha 2$ surface. All of these effects are due to the relatively large size of the Bi atom. The absence of the common Bi/GaAs(100) (2×4) - $\beta 2$ surface is also analyzed. For Bi/GaAs(001)- $c(4 \times 4)$ surface, the absorption energy for different kinds of dimers (Ga-Ga, Ga-As, Ga-Bi, As-As, As-Bi and Bi-Bi) is calculated and the surface phase diagram is constructed for desorption of Ga-Bi dimer and Bi-Bi dimer. The adsorption of Bi-Bi dimer accompanied with Ga-As dimer desorption process is an important elemental process during MBE growth of GaAsBi on a GaAs (001) surface.

Nanostructures

Achour et al. [86] have investigated structural and electronic properties of $\text{GaAs}_{1-x}\text{Bi}_x$ alloys and $(\text{GaAs})_m/(\text{GaBi})_n$ superlattices (SLs) using full potential linear augmented plane wave (FPLAPW) method as implemented in the LmtART code and the full potential linear muffin-tin orbital (FPLMTO) method as implemented in the WIEN97 code. In both cases, they are possibly semiconductors when the proportion of GaBi is no more than that of GaAs and the semi-metallic property appears if the proportion of GaAs is lower.

The first-principle calculations of bismuth nanowires (NWs) and Bi nanotubes (NTs) with the [012] crystalline direction were performed by Qi et al. [87] to investigate the relative stability and electronic properties. Bismuth NWs are indirect bandgap semiconductors, which have most stable core-shell structure and the bandgap decreases with increasing diameter, while Bi NTs prefer square cross-sections to circular ones and are more sensitive to wall thickness than diameters.

The investigation of Bi clusters has attracted great attention ever for the decades. Gupta et al. did a series of work on the Bi containing neutral, ionic clusters such as In_xBi ($x = 1-4$) [88], BiGa_y [89] and Bi_xIn_y [90], using experimental results (photoelectron spectroscopy, velocity map imaging) and first principle theoretical methods. The results of structures, electronic energy levels, molecular orbitals and photoelectron spectra for all the Bi containing clusters are obtained. Thorough studies on Bi_n ($n = 2-12$) clusters from both experiments and theoretical computations have been carried out by lots of researchers [91].

2.2.2. Electronic and Optical Properties

III-Bi Compound

The electronic properties of binary III-Bi have been investigated in detail [55]. BBi, AlBi, and GaBi in the ZB structure [75] are calculated using a PWscf code. For phonon properties, it is found that the born effective charge and LO-TO splitting of BBi increase with rising pressure. Furthermore, the ZB structure phase is the ground state of BBi and the band structure of BBi shows unique features like a strong *p-p* mixing of the VBM using WIEN2k code [76]. The calculated charge density shows an anomalous behavior, characterized by a charge transfer towards the “cation” B atom.

Amrani et al. [92] have applied the first principle of FPLAPW method as implemented in a WIEN2k code and the quasi-harmonic Debye model to investigate structural, elastic, electronic and thermal properties of AlBi, which was confirmed to have a semiconducting nature with a small and direct bandgap. For the properties such as volume, bulk modulus, thermal expansion, Debye temperature and heat capacity, the dependence on temperature in the range of 0–1200 K at different pressures as well as on pressure at different temperatures are successfully obtained by considering the phononic effects based on the quasi-harmonic Debye model.

GaAsBi

GaAsBi has many possible technical applications, including solar cells, lasers, transistors and spintronic devices, due to the unusual properties of this highly mismatched alloy. Therefore, a large number of calculations have been performed to reveal electronic properties of GaAsBi alloy. Typical density functional theory (DFT) calculations [60,77,78,93] show that with increase of Bi concentrations, the bandgap shows a substantial decrease and a strong nonlinear dependence is also observed. It is suggested that the bowing parameter has a marked contribution from structural effects.

The electronic and optical properties of $\text{GaAs}_{1-x}\text{Bi}_x$ NWs are investigated. The SO corrected bandgap of NWs decreases clearly with increasing Bi concentration. Optical properties, such as dielectric function, optical absorption spectra and reflectivity, enhance in the low energy range when the Bi concentration in GaAs is increasing. Besides, the Bi doped GaAs NW represents stability in the absorption coefficient at higher energies compared with the Bi doped GaAs bulk material [94].

GaNBi

Mbarki et al. [82] calculated the structural and electronic properties of $\text{GaN}_{1-x}\text{Bi}_x$ alloys employing the FP-LAPW as implemented in the WIEN2k package. The lattice parameter of the alloys increases with increasing Bi concentrations. The band structure for different Bi compositions and effective masses of electrons are also calculated. It is found that the material remains a semiconductor until $x = 0.5$ and becomes a semimetal for x greater than or equal to 0.625. And GaNBi shows a giant and composition dependent optical bandgap bowing, and also has a phenomenal bowing of the SO split energy [95].

AlNBi

Mbarki et al. [81] performed first principle study for structural and electronic properties of AlNBi alloy employing the pseudopotential method as implemented in the Quantum-Espresso code. The lattice parameter of the ternary alloy increases with increasing Bi composition while the bandgap decreases displaying a strongly dependent bowing parameter. At nearly 2%, there is a transition between indirect (AlN) and direct (AlNBi) semiconductor, and the electron effective masses of the binary compounds and their ternary alloy as a function of Bi content have been calculated.

Here, the structural, electronic and optical properties of III-V bismides predicted by first principles method were summarized in Table 2.

Table 2. Summary of the first-principles method used for predicting properties in III-V bismides.

Structure	Structural Properties	Electronic Properties	Optical Properties
Thin Film	BBi/GaBi/AlBi [75,76,92] $\text{AlN}_{1-x}\text{Bi}_x$ [81] $\text{GaN}_{1-x}\text{Bi}_x$ [82] $\text{GaAs}_{1-x}\text{Bi}_x$ [77,78,86,93,96]	BBi/GaBi/AlBi [75,76,92] $\text{AlN}_{1-x}\text{Bi}_x$ [81] $\text{GaN}_{1-x}\text{Bi}_x$ [82] $\text{GaAs}_{1-x}\text{Bi}_x$ [60,68,69,77–79,86,93,96,97] $\text{InP}_{1-x}\text{Bi}_x$ [73,83] $\text{InSb}_{1-x}\text{Bi}_x$ [74,80]	$\text{GaAs}_{1-x}\text{Bi}_x$ [93,96,97]
Surface		Bi/GaAs(001)-c(4 × 4)surface [85] Bi/GaAs(100) (2 × 1) and (2 × 4) surfaces [84]	
Nanostructure	Bi-doped GaAs NWs [94] Bi^{4+} ions [98] Bi-NWs, Nanotubes [87] Bicluster [88–91]	Bi doped GaAs NWs [94] Bi^{4+} ions [98] Bi NWs, Nanotubes [87] Bi cluster [88–91]	Bi-doped GaAs NWs [94]

2.3. Other Methods

Dai et al. [99] proposed a theoretical model of classical mechanical atom-surface scattering which includes both single and double collisions from a many-body target to determine the surface composition of molten Ga-Bi alloys by rare gas Ar atoms scattering. These calculations indicate that rare gas scattering can provide a precise measure of surface segregation in the outermost layer of dilute liquid alloys. Imhof et al. [100] modelled temperature-dependent PL in a Ga(AsBi) structure in an excitonic hopping model and compared to experiment. When using a single energy scale, the theory and experiment cannot be brought into agreement. Thus, a second energy scale is introduced, resulting in a good agreement between theory and experiment. The two scales are identified with spatially large alloy disorder and additional cluster states subdivide this first scale.

3. Binary Bismides

To fully understand the properties of ternary III-V-Bi compounds like GaAsBi and InAsBi, both binary endpoints (GaAs and GaBi, InAs and InBi) need to be analyzed. Traditional III-V compounds like III-P, III-As and III-Sb have been well studied theoretically and experimentally, but for III-Bi compounds, a lack of experimental results make theoretical models for binary bismide critically important. As is known, no natural III-Bi exists on earth, the only successfully synthesized one among the III-Bi family (BBi, AlBi, GaBi and InBi) was InBi by Keen et al. [101]. However, InBi was not synthesized as a thin film, but existed in bulk crystal form. Attempts have been also made to grow GaBi and AlBi, and still no epitaxial growth is found.

3.1. Theoretical Predictions

As the last element in group-V in the Periodic Table, Bi has a large atomic size. Consequently, III-Bi is expected to differ from conventional III-V compounds in structural and electronic properties. Theoretical calculations indicate that the 6s orbital contraction of Bi significantly affects the band structure of III-Bi compounds, resulting in a small or even negative bandgap [102]. Additionally, stable phase configuration for BBi, AlBi, GaBi and InBi have also been calculated using first principle calculation based on FP-LAPW or PW-PP (plane-wave pseudopotential) methods [102,103]. Table 3 summarizes band structure, lattice constant, bandgap and band type of BBi, AlBi, GaBi and InBi obtained from different calculations.

Table 3. Calculation results for structural and electronic parameters of III-Bi compounds. I = indirect band, D = direct band and C = conductor.

	Stable Phase	a (Å)	c (Å)	E _g (eV)	Band Type
BBi	ZB [102]	5.390 ~5.529 [102]	— —	−0.085 (FP-LAPW) [102] 1.134 (PW-PP) [103]	I [103]
AlBi	ZB [102]	6.266 ~6.460 [102]	— — —	−1.81 (FP-LAPW) [102] 0.042 (PW-PP) [103] 0.02 (FP-LAPW) [92]	D [103]
GaBi	ZB [102]	6.178 ~6.470 [102]	— —	−2.91 (FP-LAPW) [102] 0 (PW-PP) [103]	C [103]
InBi	PbO [102]	5.000 [102]	4.800 [102]	−4.75 (FP-LAPW) [102] 0 (PW-PP) [103]	C [103]

From Table 3, we can conclude that BBi, AlBi, GaBi all tend to crystallize in ZB structure, similar to conventional III-P, III-As and III-Sb compounds, while for the heavy InBi, the most stable phase configuration is PbO when the relativistic effect is considered [102,104]. Ferhat et al. calculated the lattice constant of these four bulk materials using first principle study based on the FP-LAPW method, seen in Table 3. In addition, they calculated bandgap of the four binaries showing a negative value

respectively. By more accurate calculation modification, the bandgap of GaBi is revised from -2.91 to -1.45 eV. In this case, we can expect a moderately negative bandgap of BBi and AlBi, yet GaBi and InBi still remain semimetallic [102]. This is consistent with Wang and Ye's calculations carried out by first principle DFT calculations based on PW-PP, that BBi and AlBi are semiconductors with a positive bandgap, while both GaBi and InBi exhibit semimetallic characteristics. In detail, BBi has an indirect bandgap with a value of 1.134 eV, AlBi still holds for a positive bandgap of 0.042 eV but the band type has changed to a direct one. Nevertheless, GaBi and InBi exhibit semimetallic characteristics similar to Ferhat's results [103]. The heavy Bi atom not only causes the crystalline and band structure of III-Bi compounds to be different from common III-V compounds, but also largely influences the valence charge density distribution due to the relativistic contraction of the 6s orbital of Bi. Consequently, the charge density of BBi remarkably shifts towards the boron atom, suggesting a weak ionic B-Bi bonding, totally different from the conventional III-V compounds like GaAs where the charge density is towards the anion (As) exhibiting the covalent bonding nature [75].

3.2. Growth of Binary III-Bi

For thin film synthesization of BBi, AlBi, GaBi and InBi, InBi is the only one known to exist in bulk crystal form, grown on a (100) GaAs substrate using MBE by Keen et al. [101]. Growth temperature and In:Bi flux ratio were found to influence the crystallinity of InBi film significantly. At 400 °C above the melting point of Bi, no crystalline InBi was fabricated because of the relatively high vapor pressure. In addition, droplets consisted of In_2Bi and In appeared. Decreasing the growth temperature to 100 °C when the Bi:In flux ratio was fixed at 3.7, droplet formation was still not avoided. However, polycrystalline InBi began to form rather than previous In_2Bi . Considering the excess Bi droplets on the surface, a reduced Bi flux was required to achieve good crystalline film. Further decreasing the growth temperature to 80–90 °C together with a reduced In:Bi flux ratio to 1.5, crystallinity of InBi was improved, accompanied with a poorly epitaxial InBi. Even at such a low Bi flux, Bi droplets on the surface were still not eliminated. Thus, it is concluded that InBi film growth should be operated at a low temperature below 100 °C and also at a Bi:In flux ratio <1 . This growth parameter differs largely from traditional III-V compound growth, which needs a group-V overpressure condition. Keen et al. also attempted to grow GaBi and AlBi, but regrettably, no epitaxial growth was found.

4. Epitaxial Growth of GaAsBi

4.1. Bi-Induced Surface Reconstruction, Segregation and Surfactant Effect

4.1.1. Surface Reconstruction

Bismuth is confirmed to be an excellent surfactant in III-V compound growth, which influences the surface reconstruction of matrix materials during epitaxy process. Bismuth induced GaAs (100) (2×1) , (2×4) , (4×3) and (4×4) reconstruction have been investigated [84,85,105].

According to the electron counting model, GaAs (100) (2×1) reconstruction is usually unstable [84]. However, Bi can stabilize this Bi/GaAs (100) (2×1) reconstruction due to a larger size of Bi atoms comparing to that of As atoms, which reduces surface adsorption energy and forms a pseudogap at Fermi energy [84]. Moreover, this reconstruction is only observed when the As_2 :Ga flux ratio is around 0.5. With more Bi atoms incorporated, the as grown GaAsBi layer shows large uniformity and strong PL intensity [106]. Also, this huge difference in atomic size causes Bi atoms to form clusters, phase separation and atomic ordering during epitaxial growth [107]. For GaAsBi alloys with a Bi content up to 10%, CuPt-type ordering of As and Bi atoms on $\{111\}\text{B}$ planes are observed through TEM, but when Bi content is increased to 13%, phase separation occurs instead of the pronounced atomic ordering.

On Bi/GaAs (001) (2×4) surface, Bi induced (2×1) and (2×4) reconstruction depend on surface annealing temperature. The Bi/GaAs (001) (2×4) reconstruction is similar to GaAs (001) (2×4)

with the top dimers replaced by Bi deduced from scanning tunneling microscope (STM) images [108]. Deposit of 1 ML Bi on GaAs (001) can temporarily make the surface staying in (2×1) and (1×3) reconstruction but soon change into a more stable (4×3) reconstruction, losing $1/3$ ML of Bi [109]. When Bi atoms are deposited onto a surface with a (1×3) reconstruction, they tend to form droplets due to surface Bi-Bi interaction, while depositing on a (2×1) surface produces a flat layer and causes As rich, Bi deficiency in the $[-110]$ direction and Bi clusters. Deposition of 2.4 ML and 6 ML of Bi onto the β_2 (2×4) reconstruction produces a surface with a (1×3) and (4×3) RHEED pattern, respectively. With adding more Bi atoms, the surface morphology changes from terraces to short and meandering steps [105].

4.1.2. Segregation

The Bi-GaAs equilibrium phase diagram shows a huge miscibility gap, so GaAsBi is synthesized under a non-equilibrium dynamic process. Even if it is synthesized successfully, the distribution of Bi is sometimes non-uniform, such as composition fluctuations, clusters and/or surface droplets. Norman et al. theoretically predicted Ga-Bi bonding was quite weak in a ZB structure and phase segregation tended to occur in GaAsBi. They found that Bi atoms segregated to form anisotropic microstructures like pannikins [107]. Luna et al. found lateral composition modulations (LCMs) by means of transmission electron microscope (TEM) [110]. The TEM images show that Bi atoms segregate to form quasi-periodical nano-columns along the growth direction. Wu et al. also used TEM to observe phase segregation phenomenon in GaAsBi during annealing and found Bi clusters [110]. The phase was found to transform from ZB Bi-rich to rhombohedral-Bi in $\{111\}$ continually until all the Bi atoms were consumed in the matrix.

4.1.3. Surfactant Effect

Because of the large atomic size, Bi would increase the surface tension [111] and enhance the adatom diffusion [112,113], making itself a good surfactant for III-V alloy growth. Acting as a surfactant, Bi atoms can smoothen surface and interface of GaAs and its heterostructures during growth. They also reduce point defects and impurities in the matrix, thus decrease non-radiative recombination centers [114] and improve optical properties of the matrix materials. However, incorporation of Bi is usually non-uniform in the matrix, which makes PL quite broad. Enhancement of PL intensity accompanied by a broadening effect of full-width at half-maximum (FWHM) has been observed in InGaAsBi/GaAs QWs [115], InPBi [116], InGaPBi [117] and InAlPBi [118].

Except for Bi atoms, trimethylbismuth (TMBi) is also used as surfactant in GaAs and InAs QDs growth by MOCVD [119]. Bismuth islands will be formed when the surface is covered with more than 1 ML Bi controlled by the flux of TMBi vapor. The stability of the Bi covered surface is strongly affected by temperature. When temperature is below 500°C , the Bi covered surface remains stable, however, when the temperature exceeds 550°C [119], Bi atoms desorb rapidly. Beside TMBi vapor and temperature, substrate orientation also affects the distribution of formed Bi islands. The Bi island density on GaAs (511) is observed to be the highest [120].

4.2. Bi Surface Droplets, Incorporation and Growth Model

Among all dilute III-V bismide alloys, GaAsBi is the most studied material system due to its unique physical properties and potentials for making energy efficient and uncooled telecom lasers on GaAs. However, incorporating even a small amount of Bi into GaAs is rather challenging due to the weak Ga-Bi bonding energy, the large miscibility gap and the large difference in lattice constant between GaBi and GaAs. The weak Ga-Bi bonding energy requires a low growth temperature to prevent Bi adatoms from evaporating from surface and a low As flux as well to enhance the Bi incorporation probability. Non-incorporated Bi atoms will form a wetting layer to lower surface energy (surfactant effect) while excess Bi atoms can diffuse on the growing surface and form Bi droplets as schematically shown in Figure 2. Employing a low As flux may also risk for nucleation of Ga

droplets. Therefore, a stringent control of both As and Bi flux is essential to obtain droplet free GaAsBi. These growth requirements are in general valid for other dilute bismides like InAsBi, III-PBi and III-SbBi. Even if Bi is incorporated, a low Bi solubility may cause Ga-Bi phase separation and Bi clustering [2]. The strain induced by Bi incorporation makes thick GaAsBi film energetically unstable forming dislocations eventually, while the weak Ga-Bi bond facilitates Bi atoms to easily segregate onto the GaAsBi surface at high temperatures, forming Bi droplets, which may badly impact on crystal as well as optical property of the material. Apparently, the traditional epitaxial growth method of GaAs with an As overpressure can no longer be applied to GaAsBi growth. Attempts to explore influence of growth parameters on surface morphology and Bi incorporation, and to develop a valid growth model that can describe how the incorporated Bi content varies with growth parameters seem to be urgent so as to achieve high quality GaAsBi material with a high Bi content. The behavior of Bi atoms is the most decisive factor in the whole growth process undoubtedly, and figuring out Bi behaviors during growth can help us better understand the growth mechanism of GaAsBi. In the following part, we shall focus on epitaxial growth of GaAsBi by MBE. Detailed interpretation of Bi behaviors, dependence of Bi content on growth parameters and growth models will be reviewed.

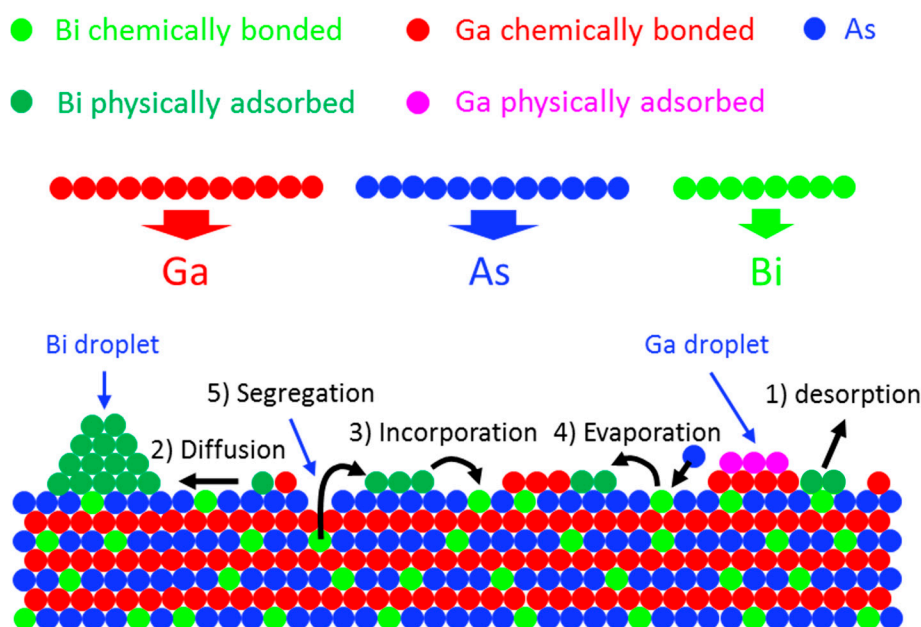


Figure 2. Schematic illustration of various physical processes of Bi atoms (surface is not fully covered with Bi adatoms).

4.2.1. State of Bi Adatoms during Epitaxial Growth

Although MOCVD and LPE have been successfully used to grow dilute bismides, MBE, in particular the solid source MBE, is the dominating technique in the research community for growth of GaAsBi due to its superior advantages of low growth temperature, precise control of element flux and the non-equilibrium growth condition. During MBE growth, the existing form of Bi adatoms is strongly dependent on growth conditions: As/Ga flux ratio, Bi/Ga flux ratio, growth temperature and growth rate. Thus, any change of the above growth parameters can result in different surface morphology, Bi content and its distribution in GaAsBi. Such a complex GaAsBi epitaxial growth is different from that of GaAs in many ways. Trying to figure out the behavior of the impinging Bi atoms is the first step to grasp the GaAsBi growth mechanism. Figure 2 gives a schematic illustration describing three existing forms of impinging Bi atoms and two physical processes of incorporated Bi atoms during GaAsBi growth.

When Bi atoms are impinging onto GaAs surface in an MBE growth chamber, they will undergo three different processes: (1) physically adsorbed Bi atoms evaporate from the GaAs surface (desorption); (2) physically adsorbed Bi atoms diffuse on the GaAs surface, then agglomerate and finally form Bi droplets; (3) Bi atoms are successfully incorporated into GaAs forming chemical Ga-Bi bonds. Physical adsorption means that Bi atoms are loosely bonded with the underneath As atoms or Ga atoms through weak van der Waals force. The strength of such a weak bonding is in the order of meV, in contrast to the order of eV for a typical chemical bond. These three processes will be elucidated in detail below. In addition, the incorporated Bi atoms at lattice sites can be ejected into surface and become physically adsorbed through: (4) thermal evaporation by breaking the Ga-Bi bond with the left sites often replaced by As atoms and (5) surface segregation.

Bi Desorption

As illustrated in Figure 2, when Bi atoms are impinging onto GaAs, they will stay on GaAs surface and be physically adsorbed to the underneath As layer if not incorporated in GaAs forming chemical bonds. The physically adsorbed Bi atoms have a possibility to be evaporated whose process depends on the growth temperature which determines the saturated vapor pressure, and the incoming Bi flux. The higher the growth temperature, the larger the saturated vapor pressure. The ultrahigh vacuum in an MBE growth chamber implies that the relation between Bi adsorption and desorption will not be in balance. If there is no local pressure built-up close to the GaAs surface, Bi desorption will continue with time and eventually all the physically adsorbed Bi atoms will leave the GaAs surface. However, due to the collision between desorbed Bi atoms and the incoming atoms, a local pressure will be built-up, which will decelerate the Bi desorption through Bi re-condensation. The value of the local pressure is proportional to the sum of the incoming flux of various species. If the value reaches the saturated Bi vapor pressure, Bi surface desorption will eventually stop.

There is a secondary effect for Bi desorption in which the desorbed Bi atoms are not from the physically adsorbed surface Bi atoms, rather from the incorporated Bi atoms underneath. For a Bi atom incorporated at a lattice site in GaAs, it may be thermally ejected back onto the surface and replaced by an As atom due to the weak Ga-Bi reactivity [121] or by surface segregation as illustrated in Figure 2. The ejected Bi atoms will be physically adsorbed and can eventually be evaporated as discussed above. Lu et al. [122] assume this thermal ejection process to follow $P \propto F_{As} e^{-U_1/KT} x$, where P , F_{As} , x and U_1 represent Bi desorption rate, As flux, incorporated Bi content and activation energy, respectively.

Bi Droplets

For Bi atoms not evaporated from GaAs surface, they will be either physically adsorbed on surface or incorporated to form GaAsBi alloy. As described before, coverage of Bi atoms on GaAs can lower the overall surface energy, i.e., the surfactant effect. Therefore, physically adsorbed Bi atoms will initially fill the whole GaAs surface as surfactant. The weak van der Waals bonding of physical adsorption ensures easy Bi surface diffusion with a long diffusion length. With more and more Bi fraction being incorporated, a metallic Bi film forms on the surface. Metal droplets finally emerge until the Bi metal film exceeds a critical thickness. Further deposit of Bi atoms on surface leads to droplet coalescence. In reference [123], the droplet coalescence process was explained by Ostwald ripening [124]. Formation of Bi droplets indicates that it is a thermodynamically driven process. Therefore, kinetic factors such as growth temperature, growth rate and growth interruption, etc., can be manipulated to delay or even hinder formation of Bi droplets.

Since growth of dilute bismides often requires a low group-V flux to facilitate Bi incorporation, this increases risk for formation of group-III droplets like Ga and In droplets on the surface. Therefore, even a small deviation from the optimal growth condition can result in coexistence of both Bi and group-III droplets on the surface. Droplet formation also depends on film thickness as a result of adatoms accumulation with time. A small deviation from the optimal growth condition leads to a thick droplet-containing film. In this sense, it is practically advantageous to grow droplet-free GaAsBi

QWs instead of thin films for device applications. Metallic Bi does not mix with Ga but can mix with In with a varied composition. Diffuse light scattering is an in-situ measurement technique which can monitor surface morphology during GaAsBi growth. The scattered light is sensitive to droplets since metallic droplets scatter light intensively [125].

In order to understand droplet behaviors, various simulations and experiments are carried out. The theoretical model using Monte Carlo simulation to analyze the Ga droplet formation on GaAs surface was discussed in reference [126]. Experiment in reference [127] confirmed that the Ga-Bi droplets coexist under a Ga-rich growth regime of GaAsBi. Further selective etching process also confirms that the surface droplets often include Ga as well as Bi. Figure 3 shows SEM image and EDX mapping of GaSbBi surface droplets. Both small droplets with a diameter less than 1 μm and large droplets with a diameter of 1.5–2.5 μm are observed. EDX mapping unambiguously shows chemical compositions of these droplets. Small droplets are overwhelmingly composed of Bi while large droplets contain both Bi and Ga. No pure Ga droplet is found. It is evident that Ga atoms adhere to the edge of Bi droplets or on top of the Bi droplets, but do not uniformly mix with Bi.

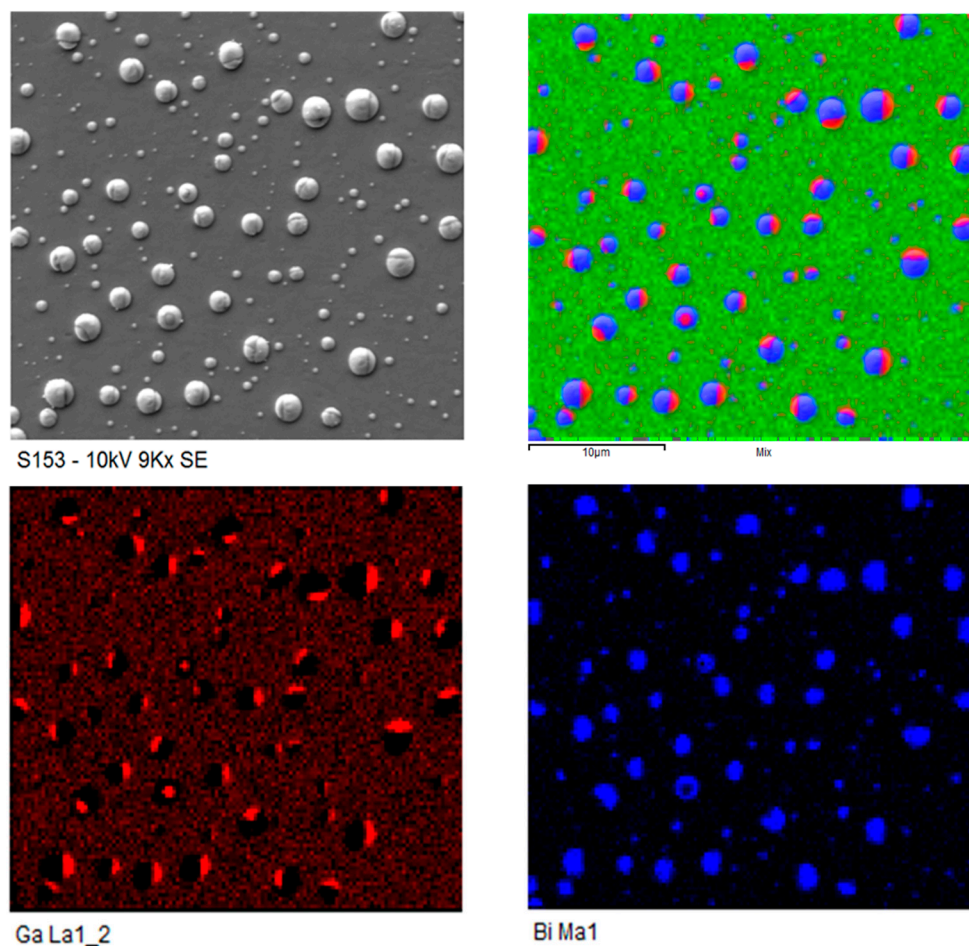


Figure 3. SEM image and EDX mapping of GaSbBi surface droplets.

Undoubtedly, growth condition is closely related to droplet formation, and careful control of growth parameters like growth temperature, Bi, As or Ga flux and growth rate, is necessary in order to grow droplet free films with a uniform Bi content. These growth parameters are not independent from each other but rather interrelated. At a low growth temperature, metal droplets distribute unevenly on surface and cluster in group probably because of low atom diffusivity compared with the condition at a high growth temperature. It is stringent to finely tune Bi, Ga and As flux to avoid both

Bi and Ga droplets in this case and the flux parameter window is narrow. Bismuth droplets can be completely removed with high temperature annealing due to significant Bi evaporation rate at high temperatures [128]. Ga-Bi droplet size and density can also be related to the amount of supplied Ga or As. With more Ga or little As supplied, Ga-Bi droplets become larger but the density shrinks. Growth rate has also a strong impact on droplet formation. Ptak's group [129] considers growth rate is a key factor that affects Bi accumulation on GaAsBi surface. A high growth rate can facilitate Bi incorporation and avoid Bi saturation that eventually leads to droplets on GaAsBi surface, because a high growth rate reduces the amount of time for Bi surface diffusion. Contrary to Ptak's results, Lu et al. [122] believe a low growth rate is necessary to incorporate Bi into GaAsBi with a low droplet density, since a low growth rate gives Bi atoms in droplets more time to be evaporated. Interestingly, both groups can quantitatively fit very well their experiment data when properly choosing fitting parameters in each model. This is likely related to different growth conditions as will be discussed below. There exists a strong competition for Bi adatoms to diffuse forming Bi droplets and to be desorbed. If the Bi surface diffusion is facilitated, e.g., under a high Bi flux, or Ga flux or at a high growth temperature, Ptak's argument is correct. When the Bi surface diffusion is suppressed, e.g., under high As flux or at low growth temperature with a rough surface, Bi evaporation will be dominant and Lu's conclusion is valid. It should be mentioned that Krotkus' group [130] realized a droplet free film by capping Be-doped GaAs on GaAsBi without giving any interpretation. We believe that the small size of Be atoms can compensate the large atomic size of Bi and thus enabling more Bi incorporation in the Be-doped GaAs and the surface becomes droplet-free.

For the Bi atoms already incorporated at lattice sites, there is a high probability to be ejected to the surface. The first route is through the As-Bi exchange during the growth of GaAsBi. Since the As-Ga bonding is stronger than the Bi-Ga bonding, an As atom is likely to replace an incorporated Bi atom when they meet. The second route is through Bi surface segregation. The accumulated strain in GaAsBi and the Bi surfactant effect favor incorporated Bi atoms to segregate toward surface to lower the overall energy. In both routes, the underlying GaAsBi layer will persistently provide as the Bi source for Bi droplet formation. There even exists another route which is somewhat unexpected. Duzik and Millunchick [131] theoretically predicted that once the Bi droplet is large enough, they will drain the underneath incorporated Bi atoms toward the droplets. This will result in a non-uniform distribution of Bi content along the growth direction, and sometimes a multi-layer structure, with a small Bi content close to surface and a large Bi content close to the bottom interface. Giatto et al. [132] found droplet formation was also related to the incorporated Bi content. With a Bi content below 3%, Bi short range order is observed; while for a Bi content above 5.4%, random anion distribution occurs accompanied with Bi droplets appearing on the sample surface despite the bulk material is highly crystalized.

Bi Incorporation

Bismuth atoms tend to surface segregate during GaAsBi epitaxial growth due to its larger atomic size compared with Ga and As. Almost no Bi can be incorporated under a typical growth condition for GaAs with As overpressure, that is $\text{As}_2:\text{Ga}$ of $\sim 7:1$ at 580°C . The fact that Bi is isoelectronic with As makes Bi not to create any defects but a good surfactant with trace Bi incorporation [133]. As a general guideline already realized in the very early stage of InSbBi growth using MBE by Oe et al. in 1981, a low growth temperature and an V/III ratio close to unity are needed so as to obtain a significant Bi content using MBE [113,134]. The real picture of growth parameters on Bi incorporation is more complicated and we shall give more elucidation below. However, we will now introduce two growth models developed from Tiedje's group on the modeled GaAsBi system under two typical growth conditions. Understanding the involved physical processes during MBE growth has great significance on precise control of growing desired films with specific compositions and material properties.

4.2.2. GaAsBi Growth Model

The two GaAsBi growth models hold the viewpoint that the source for Bi incorporation originates from the Bi surface wetting layer. The Bi surface coverage, θ_{Bi} , can be modeled with a Langmuir adsorption isotherm [133] and its model curve can be derived from reflection high-energy electron diffraction (RHEED) [133]. Langmuir isotherm assumes bonding of adsorbate atoms to themselves is much weaker than the bonding to surface. Incorporated Bi content is associated with the Ga-Bi bond.

Lu's GaAsBi Growth Model

Lu et al. proposed the first GaAsBi growth model [122] that attempts to systematically explain dependence of Bi content on the growth conditions from the physics perspective. In this model, three processes are identified to account for the Bi incorporation. Figure 4 schematically illustrates the three processes.

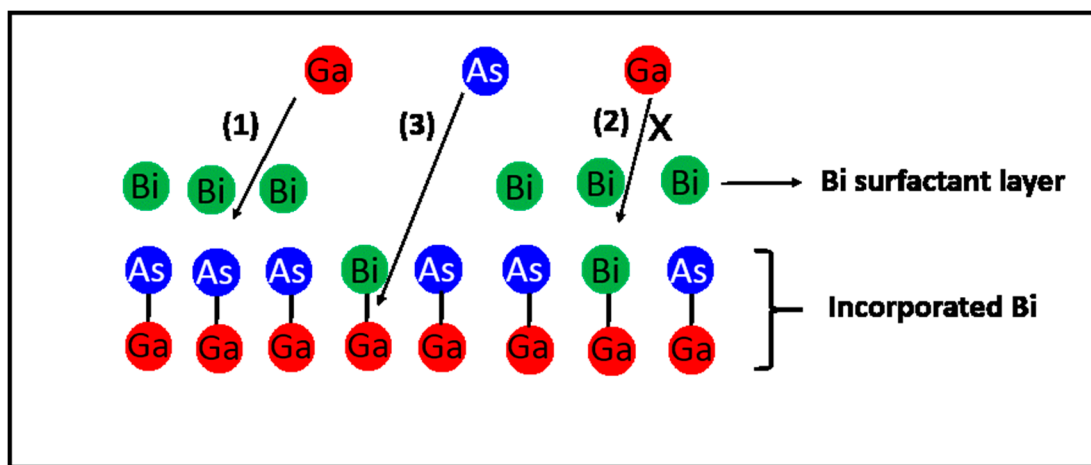


Figure 4. Schematic illustration of three processes in Lu's GaAsBi growth model. Reproduced from Reference [122].

The first process is the Bi incorporation process in which a Ga atom is inserted between the Bi surface wetting layer and the As-terminated film layer, forming a Bi-Ga-As bond. The incorporated Bi atoms come from the Bi surface wetting layer which originates from a metallic Bi surface accumulation due to the strong Bi segregation effect to surface and rather low Bi vapor pressure at the growth temperature of interest. The rate of this process is proportional to $\theta_{Bi}F_{Ga}(1-x)$, where F_{Ga} and x is Ga flux and Bi content, respectively. The second process presents that a Ga atom is inserted between two Bi atoms: one is bonded to a Ga atom and the other adheres on the surface. They assumed that the second process is forbidden due to that the form of Bi-Ga-Bi is not favorable because large strain may be induced in this kind of next-neighbor Bi atoms combination. That explains why the incorporation rate in the first process has a factor $(1-x)$ in it, meaning the second process is excluded. The third process is actually the Bi evaporation process which shows that the incorporated Bi is ejected back onto the surface and is replaced by an As atom. They assume that breakdown of the Ga-Bi bond in this process is thermally activated with a rate proportional to $F_{As}e^{-U_1/KT}x$, where F_{As} and U_1 is As flux and thermal activation energy for the replacement of a Bi atom by an As atom, respectively. Combining the first and the third processes together, they got the following rate equation:

$$\frac{dx}{dt} = \theta_{Bi}F_{Ga}(1-x) - aF_{As}e^{-U_1/KT}x \quad (1)$$

where the constant α is a fitting parameter. Under the steady state condition: $\frac{dx}{dt} = 0$, and solve the above equation, one obtains:

$$x = \frac{\theta_{Bi} e^{U_1/KT} F_{Ga}}{a F_{As} + \theta_{Bi} e^{U_1/KT} F_{Ga}} \quad (2)$$

where the Bi surface coverage, θ_{Bi} , is given by a revised function based on Langmuir model [135]. In the present case, the Bi flux in the Langmuir isotherm is substituted by the net flux, in which the corresponding Bi surface coverage can be presented as follows:

$$\theta_{Bi} = \frac{b(F_{Bi} - x F_{Ga}) e^{U_0/KT}}{1 + b(F_{Bi} - x F_{Ga}) e^{U_0/KT}} \quad (3)$$

where F_{Bi} is Bi flux, U_0 is desorption energy of Bi adatoms and b is a fitting constant. Equation (2) gives dependence of the incorporated Bi concentration on the growth parameters and fits very well with their experimental results. The various solid and broken lines in Figure 5 are computed from Equation (2) with a certain value of α , b , U_0 and U_1 which can be inferred from change in RHEED intensity [135]. The solid lines in Figure 5 show that Bi concentration increases with decreasing As flux, when holding Bi flux and growth temperature constant. This is easy to comprehend because As and Bi are always competing for Ga sites. Thus, too many As atoms will undoubtedly reduce the Bi concentration. Broken lines in Figure 5 reveal Bi concentration dependence on growth temperature and Bi flux. When keeping other parameters fixed, the Bi concentration initially increases with increasing Bi flux and finally saturates at a high Bi flux. In addition, the Bi content can also be enhanced by lowering growth temperature as shown in Figure 5, in agreement with the model.

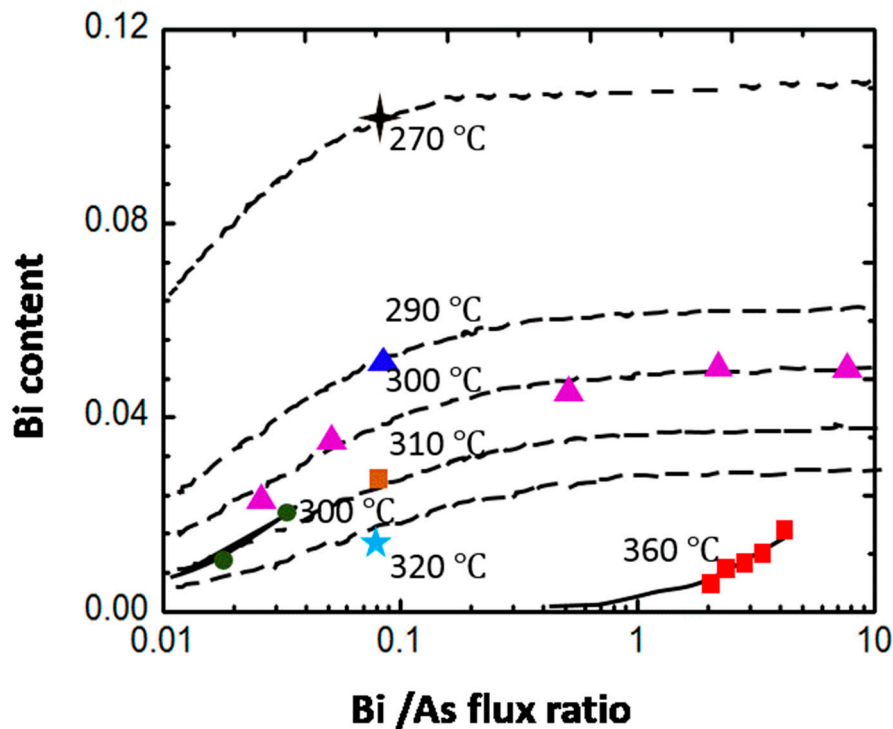


Figure 5. Comparison of the experimental results (symbols) with the Lu's model (dashed lines). Reproduced from Reference [122].

Lu's model is of great significance to explain the effect of changing Bi flux, As flux and growth temperature on Bi incorporation. The Bi incorporation is balanced by the process of As replacing Bi atoms. This is the scenario when the As flux is high and excess As adatoms are found to exist on the growing surface. Experimentally, the As:Ga flux ratio has been identified as the most sensitive

parameter in GaAsBi growth. For large Bi incorporation which often requires an As:Ga flux ratio close to or below unity, there will be no excess As adatoms and the growing surface can be group-III terminated. Lu's model is thus no longer valid as it has obeyed the major premise that the growing surface is group-V terminated. Based on the above argument, a new growth model is proposed by Lewis' et al. [136] to account for Bi incorporation when the As:Ga flux ratio is ~ 1 .

Lewis' GaAsBi Growth Model

Lewis et al. developed a new model which deemed that the Bi incorporation depended on the As₂:Ga surface coverage ratio on the growing film instead, and the As₂:Ga flux ratio should be carefully controlled during GaAsBi growth since a little fluctuation of As₂:Ga flux near 0.5 can cause a big change on Ga coverage. With this insight, Equation (4) is proposed to describe the Bi incorporation rate on the surface:

$$\frac{dx}{dt} \propto \theta_G \theta_B - a_1 x F_G - a_1 x e^{\frac{-U_1}{k_B T}} \quad (4)$$

where x is incorporated Bi content in the crystal termination layer which is assumed to be equal to that of the bulk, θ_{Ga} is Ga-terminated surface coverage, a_1 and a_2 are two constants. Interestingly, in both Lu' and Lewis' model, U_1 is used in the model but has a different meaning. From the physical process assumed in both model, U_1 should be considered as the difference of As-Ga and Bi-Ga bonding energy in Lu's model and the activation energy for a Bi atom to break the Bi-Ga bond and to form a surfactant atom in Lewis' model as will be discussed below.

Three terms in Equation (4) correspond to the three processes illustrated in Figure 6. The first process corresponds to Bi incorporation which is assumed to be proportional to $\theta_{Bi} \theta_{Ga}$. In the second process an incorporated Bi atom is attached by a free Ga atom, thus the surface Bi content being reduced. This term was neglected in Lewis' paper [136] as they claimed that it was a minor effect compared with the first and the third process. The third process represents the incorporated Bi atoms are thermally ejected back onto the surfactant layer. The activation energy, U_1 , is the energy difference between an incorporated Bi atom and a surfactant Bi atom. Analogy with Lu's model, θ_{Bi} is assumed to obey the Langmuir isotherm, which is described by Equation (3).

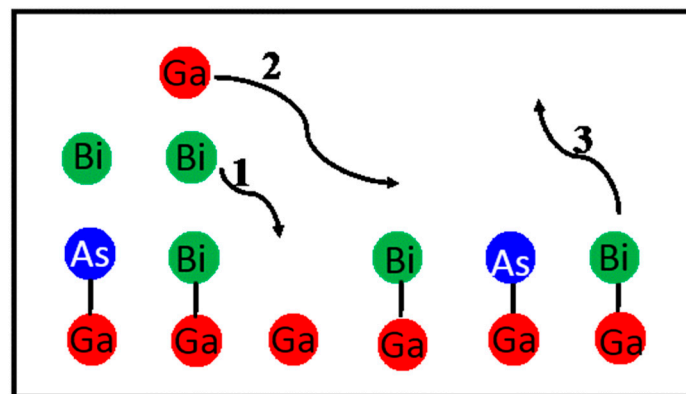


Figure 6. Schematic illustration of three processes in Lewis' GaAsBi growth model. Reproduced from Reference [136].

In Lewis' model, the Ga surface coverage θ_{Ga} is important and can affect Bi incorporation. Firstly, a model which allows Ga and As atoms hopping on GaAs surface is proposed. Without Bi, As atoms will permanently attach with Ga if they land on a Ga site, otherwise will either be evaporated with a probability of P_A or hopping to a new site if they land on an As site. Ga atoms experience a similar process that will attach when they land on an As site, or will be lost to form droplets with a small probability (P_G). This becomes extremely important at relatively low As:Ga ratios since Ga atoms will experience more hopping events until they can find an As site. With the presence of Bi, As and Ga

atoms can also stick to the incorporated Bi sites. It is assumed in this model that when an As atom lands on a Bi site, the Bi site will behave like an As which means As will not displace Bi. Similarly, Bi is assumed to behave like a Ga site when Ga lands on it. Considering these assumptions, the rate of change of As coverage, θ_A , can be described by Equation (5):

$$\frac{d\theta_A}{dt} = F_A(1 - \theta_A - x) \sum_{n=0}^{\infty} [(\theta_A + x)(1 - P_A)]^n - F_G\theta_A \sum_{n=0}^{\infty} [(1 - \theta_A)(1 - P_G)]^n \quad (5)$$

Thus, θ_G can be derived from Equation (5) by substituting the normalization condition of the termination layer: $\theta_G + \theta_A + x = 1$. This is plotted as a function of As₂:Ga flux ratio as represented by the dashed line in Figure 7 with $P_A = 0.12$ and $P_G = 0.001$.

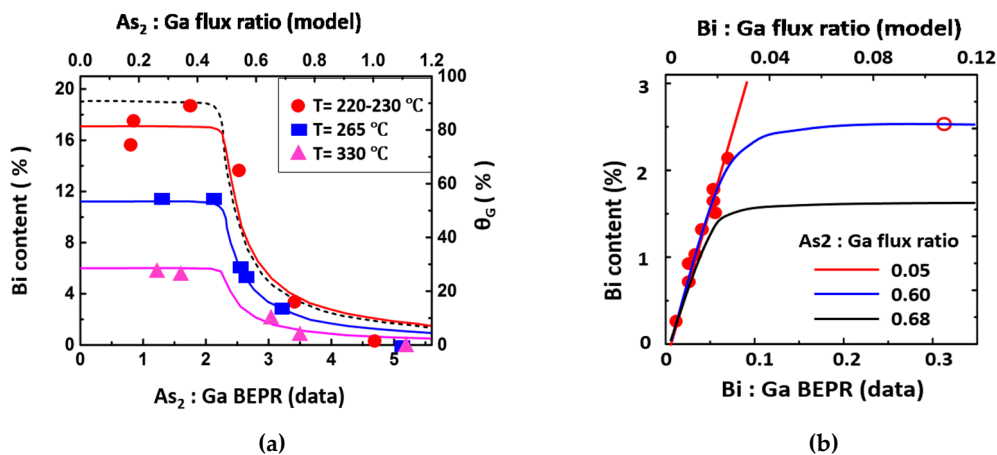


Figure 7. (a) Bi content as a function of As₂:Ga flux ratio. The solid curves are fitted based on the Lewis' model while the broken curve is a plot of θ_G for $P_A = 0.12$ and $P_G = 0.001$; (b) Bi content as a function of Bi:Ga beam equivalent pressure ratio (BEPR). Reproduced from Reference [136].

The Bi content plotted as a function As₂:Ga flux ratio and Bi:Ga BEPR are presented in Figure 7a,b, respectively. Choosing appropriate values of P_A , P_G , U_1 , a_1 and a_2 , the Lewis' model can well fit with experiments. Lewis' model focuses on Bi incorporation under the detail variation of the As₂:Ga flux ratio close to the stoichiometry condition. It is not valid for large As₂:Ga flux ratios as the Ga coverage quickly approaches to zero. In this case, the first process in Lu's model with a Ga atom inserted between a surfactant Bi atom and an As atom must be included.

4.3. Influence of Growth Parameters on Bi Incorporation

Extensive experimental work on exploring how the growth parameters affect Bi incorporation has been carried out, pointing out that different growth conditions can result in a large difference in Bi content and surface quality. The growth parameter window is narrow to compromise a high Bi content and a droplet free surface. This drives the growth conditions in general toward low growth temperature with an accurate control of As, Ga and Bi flux, and inevitably introduces point defects and clusters in the as grown GaAsBi thin films degrading optical and transport properties. We shall examine the dependence of Bi incorporation on growth parameters including As₂:Ga flux ratio, Bi flux, growth temperature and growth rate, respectively. In addition, influence of MBE growth of GaAsBi using As₂ and As₄ will also be elaborated.

4.3.1. As₂:Ga Flux Ratio

The relationship between Bi incorporation and As₂:Ga flux ratio can be qualitatively comprehended like this: both As and Bi are group-V atoms which tend to bond with Ga atoms. It is understandable that an excess As supply will outcompete for Bi since Ga-As bonding is stronger

than that of Ga-Bi bonding. Hence, decreasing As₂:Ga flux ratio will spontaneously enhance the possibility of Ga-Bi bonding and thus increase the Bi content. However, continuously decreasing As₂:Ga flux ratio will not result in a monotonic increase of Bi content, rather risk of forming Ga droplets because excess Ga atoms on the growing GaAsBi surface cannot be evaporated at such a low growth temperature. Once the group-III rich surface is established, it is no longer energetically favorable for Bi atoms to bond with floating Ga atoms due to the weak bonding energy and the large strain introduced. Thus, the Bi content becomes saturated. A careful control of the As₂:Ga flux ratio is essential to achieve a high Bi content and to avoid formation of Ga droplets.

Figure 7 shows the relationship between Bi content and As₂:Ga flux ratio for GaAsBi grown at substrate temperatures of 220–230 °C, 265 °C and 330 °C, respectively. Both the 220–230 °C and the 265 °C samples are grown with Bi:Ga BEPRs of 0.47 and 0.35, respectively, while the 330 °C samples are grown with Bi:Ga BEPRs of 0.09 [136]. The Bi content is measured using high-resolution X-ray diffraction (HRXRD) and a similar behavior can be seen from the three data sets. Bi concentration increases sharply with decreasing As₂:Ga flux ratio and then saturates for the flux ratio below 0.5.

4.3.2. Growth Temperature

Growth temperature is a key parameter in GaAsBi grown by MBE. It affects desorption of surface As and Bi atoms, surface diffusion of As, Ga and Bi atoms, dissociation of Ga-Bi bonds, Bi surface segregation and surface reconstruction. The strong segregation effect of Bi at a high temperature demands a low growth temperature for GaAsBi. Indeed, Bi incorporation is found to increase with decreasing growth temperature and the highest Bi content of 22% is achieved at the lowest growth temperature of 200 °C [136]. A sharp decrease of Bi content at growth temperature above 350 °C occurs which is interpreted as strong Bi desorption at high temperatures. Lu's study [122] found the same relation about dependence of Bi incorporation on growth temperature.

4.3.3. Bi Flux

In both Lu's and Lewis' study, Bi content initially increases with increasing Bi flux if the growth temperature, As and Ga flux are fixed. Further increasing Bi flux leads to saturation of Bi incorporation at about 5% and 2.5%, respectively, as evidenced in Figures 5 and 7, respectively. In both cases, Bi droplets are formed on surface. Such Bi saturation can be easily understood in both models described above when considering $\theta_{Bi} = 1$. In Lu's model, the theoretical value of maximum Bi content will be $= \frac{e^{U1/KT} F_{Ga}}{a F_{As} + e^{U1/KT} F_{Ga}}$. In Lewis' model the maximum Bi content will be $x = \frac{\theta_G e^{U1/KT}}{a_2}$. In the former case, the As₂:Ga flux ratio plays an important role and the maximum value can be reached when the flux ratio is close to 1. In the latter case, the saturated Bi content depends on the Ga surface coverage and will reach a maximum when the whole surface is covered by Ga. Therefore, surface coverage by one monolayer of Ga atoms will eventually stop Bi incorporation, if no access As atoms are provided.

Ptak et al. experimentally found a linear relation between Bi content and Bi flux grown with various growth rates with no Bi saturation as shown in Figure 8. However, Bi droplets formation (not shown here) was not avoided at a low growth rate when Bi flux approaching to a relatively high value. Table 4 summarizes the major growth parameters used in the work of Lu et al., Lewis et al. and Ptak et al. The growth temperature is quite similar, at about 300–330 °C, in all the three experiments. Obviously, the maximum Bi flux used by Ptak et al. is several times smaller compared with the other two groups. This explains why Ptak et al. did not find any Bi droplets for samples grown at a high growth rate, since the incoming Bi flux can be well balanced by incorporation and evaporation. Therefore, Bi content has not reached saturation yet and can be increased with increase of the Bi flux.

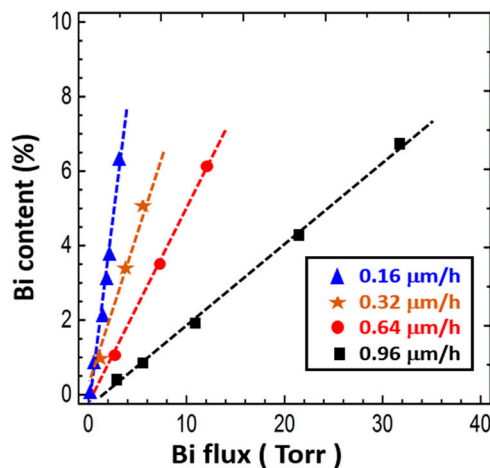


Figure 8. Bi content as a function of Bi flux grown at different growth rates. Reproduced from Reference [129].

Table 4. Comparison of growth parameters used in the three papers.

	Lu	Lewis	Ptak
Growth Temperature	300 °C	330 °C	315 °C
As flux	$2.2 \text{ nm}^{-2} \cdot \text{s}^{-1}$	$\text{As}_2\text{:Ga} = 0.5\text{--}0.68$	$\text{As:Ga} = 1.4$
Growth rate	-	$1 \text{ } \mu\text{m/h}$	$0.16\text{--}2.0 \text{ } \mu\text{m/h}$
Bi flux	$\text{Bi:As} = 0.01\text{--}7$ $4 \times 10^{-9} - 2.8 \times 10^{-7} \text{ Torr}$	$\text{Bi:Ga BEPR} = 0\text{--}0.3$ $(0\text{--}1.2) \times 10^{-7} \text{ Torr}$	$(0\text{--}3.3) \times 10^{-8} \text{ Torr}$

4.3.4. Growth Rate

Growth rate has not been paid much attention for Bi incorporation in early studies of GaAsBi growth. In Lu's study [122], the Bi content scales with the As:Ga flux ratio as seen from Equation (2). If the As flux is fixed, the Bi content will increase with increasing the growth rate, i.e., increasing F_G . For a low growth rate, the Bi content can be kept the same if the As flux changes accordingly to keep the As:Ga flux ratio constant. It turns out to be extremely important in controlling the formation of Bi droplets. With a low growth rate, Bi droplets can be avoided since any excess Bi atoms have enough time to be evaporated. Using a low growth rate of $0.07 \text{ } \mu\text{m/h}$ at $270 \text{ } ^\circ\text{C}$, Lu et al. was able to achieve $x = 10\%$ Bi incorporation with a low density of Bi droplets ($1.7 \times 10^6 \text{ cm}^{-2}$). Lewis et al. tried two different growth rates: 0.13 and $1 \text{ } \mu\text{m/h}$, and found that the $1 \text{ } \mu\text{m/h}$ sample had a higher Bi content than the $0.13 \text{ } \mu\text{m/h}$ sample.

Considering a kinetically limited growth regime of GaAsBi different from Lu's model, Ptak et al. [129] presented a new viewpoint about how growth rate affects GaAsBi growth. This new growth regime can kinetically restrict the Bi accumulation on the surface, meanwhile decreasing Bi droplets and automatically obtaining smooth surface in a wide range of Bi composition. Growth rate is thought to play a critical role in this process. A growth rate dependent Bi incorporation phase diagram with smooth and Bi droplet free surface in a wide range of Bi concentration is facilitated by adjusting Bi fluxes and growth rates. Figure 8 plots the phase diagram showing Bi concentration versus Bi flux at different growth rates. A set of samples grown at a growth rate of 0.16 , 0.32 , 0.64 and $0.96 \text{ } \mu\text{m/h}$, respectively, show the trend that the Bi concentration doubles with doubling the Bi flux, while halves with doubling the growth rate. This implies that Bi incorporation in GaAs behaves as a dopant like Si doping in GaAs. We should emphasize that this kinetically limited growth regime employs a low Bi flux, typically in the range of below $3 \times 10^{-8} \text{ Torr}$, lower than the situation studied in Lu's and Lewis' cases.

An intuitive prediction about certain composition of Bi with smooth surface can be derived from atomic force microscope (AFM) results shown in Figure 9. The presented root-mean-square (RMS) roughness values are determined from $5\ \mu\text{m} \times 5\ \mu\text{m}$ AFM scans with different growth rates and Bi compositions. It is shown that samples grown at the lowest growth rate of $0.16\ \mu\text{m}/\text{h}$ exhibit sub-nm RMS roughness values at a low Bi content below 6%, but Bi droplets for $x > 6\%$. However, for samples grown at a high growth rate of $0.96\ \mu\text{m}/\text{h}$, the trend is reversed. The surface becomes rough at a low Bi content but gets smooth at a higher Bi content with no sign of appearance of Bi droplets. The suppression of Bi droplets at high growth rates can be interpreted by the factor that the high growth rate condition will not provide sufficient time for Bi to diffuse on the surface forming Bi droplets. For the intermediate growth rate of $0.64\ \mu\text{m}/\text{h}$, the surface is smooth for Bi up to 7%. The disagreement about influence of growth rate on surface morphology of GaAsBi growth between Lu's and Ptak's results stems from the Bi surface coverage during the growth. In Lu's case, the Bi flux is very high and the growing surface is covered with Bi droplets. The low growth rate provides enough time for surface Bi atoms to evaporate resulting in a smooth surface and a high Bi content. In Ptak's case, the Bi flux is small and can be efficiently utilized to be incorporated into GaAs film. There is a strong competition between Bi incorporation and Bi surface diffusion forming droplets. In this case, a high growth rate can kinetically suppress the latter process, leading to a high Bi content with no droplets on the surface.

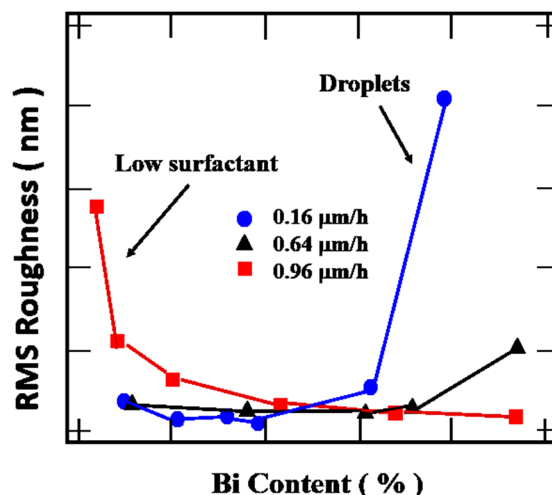


Figure 9. Root-mean-square (RMS) roughness values obtained from atomic force microscope (AFM) measurements for different growth rates and Bi compositions. Reproduced from Reference [129].

Except for the above growth parameters, As specie was also reported to have some influence on MBE growth of GaAsBi [44,135]. The optimum growth control for Bi incorporation in GaAs without forming Ga or Bi droplets is less strict when using As_4 other than As_2 as the As source. Richards et al. [137] made a systematic study upon the influence of As_2 and As_4 on GaAsBi growth and showed that for the same Bi incorporation, the required As_2 :Ga atomic flux ratio is much lower than that of As_4 :Ga. As_2 dimers effectively provide As atoms that can be directly incorporated into GaAs, while for As_4 tetramers the thermal cracking efficiency into As is low and a much broad range of As:Ga flux ratio is permitted for Bi incorporation. This indicates that the optimum growth procedure is easy to achieve under As_4 condition. The measured recovery time for As reconstruction after the Bi shutter being closed is $\sim 340\ \text{s}$ for As_2 and $\sim 800\ \text{s}$ for As_4 . Considering typical growth time of $\sim 1\ \text{s}$ for one monolayer, much shorter than the As reconstruction recovery time, use of different As species will not influence Bi incorporation. In addition, samples grown under As_2 and As_4 exhibited almost no difference in PL spectrum.

4.4. Thermal Stability and Bi diffusion

A low growth temperature and a low V/III flux ratio close to the stoichiometry condition required to effectively incorporate Bi content often result in a considerable amount of point defects and Bi clusters. Even without Bi, GaAs grown at temperatures below 300 °C contains a significant amount of native defects such as As antisites (As_{Ga}) [138] and Ga vacancies (V_{Ga}) [139]. Upon post-growth thermal annealing, the As antisites are converted to As clusters [3] leading to high resistivity [140]. Incorporating Bi into GaAs is believed to diminish the As antisites [141] and enhance PL. Post-growth rapid thermal annealing (RTA) is a common way to minimize point defects and improve optical quality, and in dilute nitrides it can significantly enhance PL intensity by orders of magnitude [142]. It has also practical use for making dilute bismide devices such as laser diodes, as the upper waveguide layer and contact layer above the active QW region are often grown at a temperature much higher than that of GaAsBi. There are a number of annealing studies reported and they are summarized in Table 5 below.

Table 5. Summary of rapid thermal annealing (RTA) on various dilute bismides.

Reference	Material	x_{Bi}	Epitaxy	Growth Temp (°C)	RTA Temp (°C)	RTA Time (s)	PL (λ)	PL Intensity
[143]	GaAsBi (QW)	0.6%–10.9%	MBE	345–400	500–900	600	No shift up to 700 °C	-
[144]	GaAsBi (bulk)	3.5%–6%	MBE	220–330	550–750	30–180	Almost no shift	3×
[145]	GaAsBi (QW)	2.2%–6.5%	MBE	380–420	600–800	30	No shift up to 800 °C	3× for $x_{\text{Bi}} = 4\%$ 2× for $x_{\text{Bi}} = 6.5\%$
[141]	GaAsBi (bulk)	1.29%–1.46%	MBE	220–315	500–800	30	-	-
[146]	GaAsBi (bulk)	2.3%	MBE	200–350	750		No shift	1.3×
[147]	GaAsBi (QW)	3%–5.5%	MBE	-	450–750	-	No shift in PL	2.2×
							60 meV red shift in PR	
[148]	GaAsBi (bulk)	3.7%	MOVPE	420	500–750	60	No shift	10×@10 K
[149]	GaAsBi (bulk)	3.5%	MOVPE	420	550–700	900	No shift in PL	-
							60 meV red shift in PR	
[150]	GaAsNBi (bulk)	3.2%	MBE	365	800	900	8 meV @GaAsBi	1×@GaAsBi
		1.4%@N	MBE			60	27.5 meV @GaAsNBi	>10×@GaAsNBi
[151]	InGaAsBi (QW)	1%	MBE	370–440	650–750	120	65 meV	3×
[152]	InPBi (bulk)	0.1–2.6%	MBE	325	400–800	120	No shift up to 600 °C	1×

Most previous reports focus on RTA of GaAsBi grown by both MBE [141,143–147] and MOCVD [148,149]. The growth temperature used is between 200 and 420 °C measured by a thermocouple. Unlike an infrared pyrometer that can accurately measure growth temperature above 450 °C with a simple calibration, the measured value by a thermocouple depends on the distance from the measured object and is thus overestimated. Post-growth RTA is performed at 500–900 °C for a typical duration of 30–900 sec. The most common assessment methods are HRXRD and PL, while other methods like time-resolved PL [144,146] and PR [149] are sometime used.

Mohmad et al. [145] reported RTA of 10–50 nm thick $\text{GaAs}_{1-x}\text{Bi}_x$ QWs with $x_{\text{Bi}} = 2.2\%$ – 6.5% grown at 380–420 °C and annealed at 600–800 °C for 30 s. Pendellösung fringes are clearly observed for

GaAs_{0.935}Bi_{0.065} up to an annealing temperature of 700 °C, indicating good crystal and interface quality. Puustinen et al. [141] carefully designed a set of 270 nm thick GaAsBi samples with the identical growth condition except using various growth temperatures between 220–315 °C. GaAs reference samples were also grown at similar temperatures. Due to the large amount of As_{Ga} antisites, the GaAs reference samples reveal residual compressive strain which decreases from 128 arcsec to 20 arcsec when increasing growth temperature from 220 °C to 315 °C. After the RTA at 500 °C for 30 s, the strain in the GaAs sample grown at 220 °C decreases to 11 arcsec, i.e., almost relieved. This is due to the diffusion of As_{Ga} antisites to As clusters [3]. For GaAsBi, the estimated Bi content is 1.46%, 1.29% and 1.30% for the samples grown at 220, 270 and 315 °C, respectively. Upon RTA, the strain of the GaAsBi grown at 315 °C remains almost unchanged when increasing annealing temperature from 500 to 800 °C. However, the strain of the GaAsBi grown at 220 °C undergoes a large shift from 438 arcsec for the as-grown to 256 arcsec when annealed at 600 °C. The interference fringes disappear for annealing temperatures above 600 °C. Interestingly, Rutherford backscattering (RBS) confirms the same amount of Bi atoms before and after annealing at 600 °C. Cross section TEM images corroborate the improvement of material quality for both the annealed sample and the GaAsBi grown at 315 °C. These observations led the authors to conclude that the RTA of GaAsBi causes reorganization of Bi atoms towards GaAsBi clusters with a high Bi content grown at very low temperatures in addition to the removal of As_{Ga} antisites, but has little effect on GaAsBi grown at a relatively high temperature of 315 °C. Grant et al. [147] studied RTA of GaAsBi/GaAs single QWs with $x_{Bi} = 3\%$ and 3.5% reaching a similar conclusion that GaAsBi is stable up to an annealing temperature of 650 °C.

Photoluminescence is a widely used means to assess optical quality upon RTA. However, PL measures a light emission related to the extrinsic property. If there exist traps caused by Bi and/or As clustering, alloy and/or strain non-uniformity, carriers can be localized at such traps at low temperatures. The temperature dependent PL will show a typical S-shape behavior with emission energy lower than the predicted values by Varshini's law. As shown in Table 5, for GaAsBi, there is no detectable peak wavelength shift for annealing temperature up to 700 °C and a marginal or no shift for annealing temperature between 700–800 °C. The enhancement of PL intensity at RT is also marginal, up to a maximum of three times, in contrast to the case of dilute GaAsN. Mohamad et al. [145] found that the enhancement factor is a constant of 3 for x_{Bi} up to 5% and then decreases to nearly 1 for $x_{Bi} = 6.5\%$. The PL intensity increases with annealing temperature up to 700 °C and then decreases for $x_{Bi} = 4\%$ and up to 600 °C for $x_{Bi} = 6.5\%$. Both the $x_{Bi} = 4\%$ and the $x_{Bi} = 4.8\%$ samples show an S-shape trend of PL peak energy as a function of temperature and the RTA at 700 °C for 30 s has almost no effect on removal of the S-shape for the $x_{Bi} = 4\%$ sample but slightly mitigates the localization for the $x_{Bi} = 4.8\%$ sample. In another study by Mazzucato et al. [146] with $x_{Bi} = 2.3\%$ in a 200 nm thick GaAsBi, the S-shape behavior appears at a low excitation of 1 mW but disappears at an elevated excitation power of 10 mW, because a high excitation power can saturate the localized traps. After annealing at 750 °C, the S-shape disappears and the PL peak energy shows a blue-shift of 5 meV. This is attributed to the removal of localized states in the annealed sample as evidenced by a reduction of FWHM of about 10–25 meV. They also performed time-resolved PL and found the decay time increases from 130 ps for the as-grown sample to 180 ps for the annealed sample at 750 °C. This indicates a moderate reduction of non-radiative recombination upon thermal annealing. Time-resolved PL was also employed by Butkute et al. [144] to study thin and strained (30–100 nm) and thick and relaxed (0.5–1.5 µm) GaAsBi layers. For thick and relaxed GaAsBi layers, the $x_{Bi} = 3.5\%$ sample shows no obvious change in decay time of tens ps after RTA at 600 °C for 30 s, while the decay time of the $x_{Bi} = 5\%$ sample decreases from tens ps to less than 1 ps after the same RTA process. This is likely due to generation of dislocations in the $x_{Bi} = 5\%$ sample upon annealing. For the thin layers, the decay time was measured to have several hundreds ps.

Moussa et al. [148] reported RTA on 25–50 nm thick GaAs_{0.963}Bi_{0.037} grown by MOCVD. The XRD pattern shows no change up to 700 °C for 900 s while the 10 K PL reveals an enhancement of integrated PL intensity by more than 10 times and a reduction of FWHM from 126 meV to 104 meV. Later, the

same group used PR to evaluate transitions in $\text{GaAs}_{0.965}\text{Bi}_{0.035}$ and found a red-shift of 60 meV after RTA at 600 °C for 900 s [149]. No change in XRD is observed while the 10 K PL shows a peak at a constant energy of 1.36 eV when increasing the annealing temperature to 600 °C. This anomalous red-shift measured by PR is unexpected and the authors attribute it to an internal rearrangement of Bi atoms inside GaAsBi.

In addition to GaAsBi, there are a few reports on RTA in other dilute bismide alloys. Feng et al. [150] investigated RTA on GaAsBi, GaAsN and GaAsNBi ($x_N = 1.4\%$ and $x_{Bi} = 3.2\%$) grown at 365 °C by MBE. The PL intensity for GaAsBi remains nearly unchanged up to 700 °C and then decreases, while for GaAsN, it increases nearly three orders of magnitude after being annealed at 600 °C and remains constant then. For GaAsNBi, it monotonically increases up to 700 °C and then decreases. The peak energy blue-shift is marginal for GaAsBi, up to 8 meV at 700 °C, but is large for GaAsNBi, about 27.5 meV at the same annealing temperature. No obvious change in XRD is seen in GaAsNBi for annealing up to 800 °C, indicating a very stable material. This implies that incorporation of Bi into GaAs has a minor effect on degradation of optical quality and thus RTA has also a minor effect for improving material quality. However, incorporation of N results in significant degradation of PL and RTA can remedy the crystal defects induced by N atoms. Ye et al. [151] reported RTA on 7.5 nm thick InGaAsBi QWs grown by MBE. Incorporation of Bi into InGaAs QW extends PL wavelength from 1.24 μm to 1.29 μm and increases PL intensity at the same time. Upon RTA, the PL intensity in InGaAs QW decreases with annealing temperature and no PL is observed at 700 °C. In the contrary, the PL intensity in InGaAsBi QW increases up to 700 °C and then decreases. However, a large red-shift of PL peak of 60 meV is observed already at 650 °C. This is due to the out-diffusion of Bi atoms from the QW. By cladding the QW with GaAsBi, the red-shift is reduced to be less than 10 meV under the same annealing condition as a result of suppression of Bi diffusion out of the InGaAsBi QW. Wu et al. [152] studied RTA on $\text{InP}_{1-x}\text{Bi}_x$ thin films with $x_{Bi} = 0.1\%–2.6\%$ grown by gas-source MBE. Both XRD and PL show negligible changes in spectral features up to 600 °C. Above 600 °C, Bi content drops and PL shows a blue-shift. The integrated PL intensity is almost unchanged up to 600 °C and decreases afterwards. This critical annealing temperature is lower than 700–750 °C in the case of GaAsBi, which is expected because of the lower In-Bi bonding strength than that of Ga-Bi bonding.

In summary, dilute bismide is a stable material. GaAsBi can withstand thermal impact up to 700–750 °C without any change in crystal quality and PL emission wavelength. The ability to remove non-radiative recombination is, however, rather limited, only having a marginal effect on improving PL intensity. When indium is incorporated, the thermal stability is reduced and the dilute bismide alloy is stable up to 600–650 °C as a result of weak In-Bi bonding. These RTA studies imply that dilute bismide alloy can be a promising active material for laser and detector applications, as most of such devices require a growth temperature no more than 600–650 °C.

5. Other Dilute Bismides

5.1. III-N-Bi

Differing from nitride alloys which mainly have a downward energy shift effect on CB, Bi mainly has an upward effect on VB [153]. Co-doping of both elements is predicted to have more freedom in adjusting bandgap of materials applicable from UV to IR optical range. As the largest and heaviest atom among group-V, Bi exhibits a large difference in atom radius (155 pm) and electro-negativity (1.8) from that of N (75 pm and 3.0), respectively. Consequently, replacing a small amount of N with Bi in GaN, significant changes in physical properties are expected to appear. However, the highly mismatched III-N-Bi alloys are rarely investigated experimentally and theoretically. Up to now, only sporadic studies on GaNBi and AlNBi have been reported in the literature.

5.1.1. GaN_{1-x}Bi_x

The first growth of GaN_{1-x}Bi_x alloy was demonstrated on sapphire substrate by research group from University of Nottingham using MBE method [154]. However, no significant Bi is incorporated into GaN at growth temperature from 600 to 800 °C, and introducing Bi during growth is found to act as a surfactant that can improve surface morphology and reduce RMS roughness values. Lowering the growth temperature from 670 to 100 °C, the same group achieved up to 11% of Bi in GaN detected by Rutherford backscattering (RBS) within the $\pm 5\%$ accuracy. XRD measurement reveals that Bi is distributed in an amorphous GaN_{1-x}Bi_x alloy phase because no other XRD peaks of a new crystalline phase are observed. Despite of the amorphous structure, dramatic absorption energy shift from 3.4 eV in GaN to below 1.2 eV is seen for GaN_{1-x}Bi_x alloy with $x > 0.1$. The decreased absorption energy tail is interpreted as two reasons: downward shift of CB and upward shift of VB resulted from Bi; interaction between the Bi-related states and the extended states of GaN matrix [155].

Similar to growth of other dilute bismide compounds, growth temperature, Bi flux and Ga:N ratio are all found to have an influence on GaN_{1-x}Bi_x growth. The XRD spectra of GaN_{1-x}Bi_x films grown at different growth temperatures attest that, with decreasing growth temperature, the intensity of GaN peaks decreases accompanied by a broad peak width. That is to say, decreasing growth temperature leads to a decreased GaN crystal fraction and size, meanwhile an enhanced Bi incorporation [155]. Microstructure study of GaN_{1-x}Bi_x film by high resolution TEM exhibits a dependence of microstructure on Bi composition and the variation from columnar growth to an almost amorphous structure. For the films with a high Bi content, small crystalline clusters are found to be embedded into the amorphous structure. As for Bi flux influence, electron probe microanalysis (EPMA) and RBS consistently confirm that Bi composition in GaN_{1-x}Bi_x alloy arises with increasing Bi flux. In addition, GaN_{1-x}Bi_x samples grown under different Ga:N ratios show no difference on Bi concentration, but an obvious different effect on optical properties. Under the N-rich grown samples, only a weak absorption tail is observed at low energy region about 1 eV, and at high energy region, a strong absorption edge corresponding to GaN matrix around 3.4 eV appears. Nevertheless, under the Ga-rich growth condition, samples exhibit an enhanced absorption intensity in the low energy tail, indicating a rising substitutional Bi incorporation [156]. Therefore, significant Bi incorporation needs to be close to the stoichiometric or slightly Ga-rich conditions.

5.1.2. AlN_{1-x}Bi_x

To our knowledge, no experimental work on AlN_{1-x}Bi_x has been reported. In [81], ab initio calculation based on pseudopotential method was carried out to predict structural and electronic properties of ZB AlN_{1-x}Bi_x alloys. Calculation results reveal that the lattice parameter of AlN_{1-x}Bi_x for $x < 20\%$ increases with increasing Bi content, but variation in lattice constant does not obey the Vegard's Law. They also predicted a bandgap reduction with increasing Bi concentration and the change from an indirect to a direct bandgap at $x \cong 2\%$. The nonlinear decrease of the bandgap with increasing Bi content suggests an abnormal bandgap bowing effect of AlN_{1-x}Bi_x. Furthermore, effective mass of AlN, AlBi and AlN_{1-x}Bi_x are all calculated. However, no experimental results are available to testify the validity of the calculations.

5.2. III-P-Bi

III-P-Bi are also widely investigated such as GaPBi, InPBi, InGaPBi and InAlPBi. Berding et al. theoretically calculated bond energies, bond lengths, strain coefficients for dilute InSb_{1-x}Bi_x, InAs_{1-x}Bi_x and InP_{1-x}Bi_x in ZB structure, and predicted the miscibility gaps [80]. The bond lengths for InBi, InSb, InAs and InP are 2.880 Å, 2.805 Å, 2.622 Å and 2.541 Å, respectively, i.e., the bond difference between InBi and InP is the largest at 12%, resulting in the largest strain in InPBi. Mixing enthalpy calculation shows that ZB InPBi is the most difficult to be synthesized. However, once InPBi

is successfully realized, it would be the hardest during these three materials due to the inverse relation of the hardness and the bond length.

5.2.1. InPBi

Epitaxial Growth

Due to synthesis challenges, InPBi crystals were first realized by Wang et al. using gas source MBE in 2013 [116] which is 25 years after the theoretical prediction. It shows several abnormal properties comparing with other dilute bismides, especially for its optical property. InPBi has a strong and broad PL spectrum from 1.4 to 2.7 μm at RT [157], which is an attractive candidate for making super luminescence diodes (SLDs) used in optical coherence tomography (OCT).

With a narrow growth parameter window similar to the growth of GaAsBi, growth temperature, PH_3 pressure, growth rate and Bi flux are the most important parameters affecting the crystal qualities of InPBi. Figure 10 shows AFM images of InPBi films grown at 364, 324 and 275 $^\circ\text{C}$, respectively. For high temperature growth (364 $^\circ\text{C}$), Bi cannot be fully incorporated into InP matrix and form micrometer-size (In)Bi metallic droplets leading to a large RMS roughness value of 85 nm. For low temperature growth at 275 $^\circ\text{C}$, the diffusivity of In, P and Bi atoms is significantly reduced, causing excess atoms accumulation on the surface and the growth dynamics will be more complicated. Even the InP reference sample grown at the same temperature shows similar morphology implying that Bi has a negligible effect on surface morphology of InP at this low growth temperature. Combining XRD results and AFM images, the optimum growth temperature for InPBi is about 300–330 $^\circ\text{C}$.

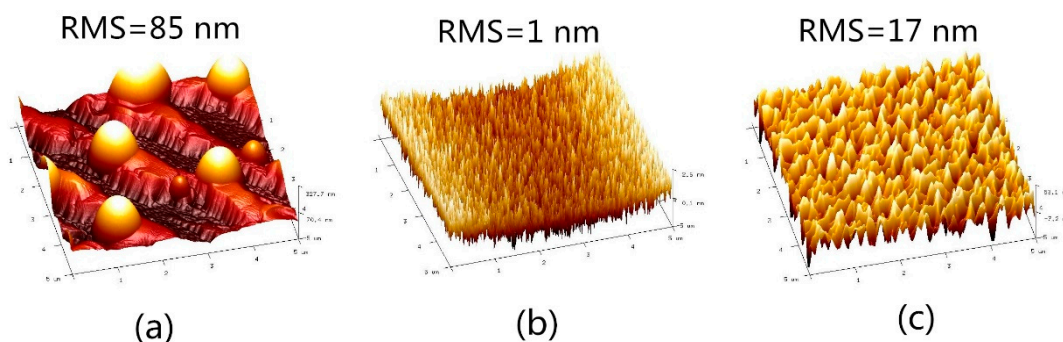


Figure 10. AFM of InPBi films grown at (a) 364 $^\circ\text{C}$; (b) 324 $^\circ\text{C}$ and (c) 275 $^\circ\text{C}$.

For PH_3 pressure, it is usually excessive to avoid formation of In droplets on the surface. However, the case for growth by gas source MBE is different compared with solid source MBE. Experiments have shown that the incorporated Bi concentration is almost independent on PH_3 pressure in a certain range, but the PH_3 pressure will influence the crystal quality. Bi content is found to inversely proportional to the InP growth rate. Meanwhile, the low growth rate can inhibit the formation of surface droplets and improve the uniformity of the distribution of Bi atoms. As for Bi flux, the Bi content is approximately linear to Bi flux as long as no Bi droplets are accumulated on the surface.

Structure Property

Lattice expansion is expected in Bi incorporated InP(Bi) materials due to a large atomic size. The lattice constant for ZB InBi is around 6.5 \AA [116,158], which is quite large comparing to 5.858 \AA of InP. So the lattice constant of InPBi should be between that of InP and InBi. Raman spectrum performed on InPBi at RT reveals four new vibration modes compared to that of InP with two at 149 and 171 cm^{-1} , deduced to be InBi like TO and LO phonon modes, respectively, while the other two are at 311 and 337 cm^{-1} which are not found in the low temperature grown InP reference sample [159]. The integrated Raman intensity of the vibration modes at InBi-like TO, LO and 337 cm^{-1} are linear

to the Bi content at the reported range 0.3%–2.3%. Moreover, the InBi-like TO and LO modes show a strong Raman intensity comparable to that of the InP matrix, which is quite different from other dilute bismides. Wei et al. [160] presented a formula to quantify the relationship between Raman intensity of different vibration modes and the Bi content, which is useful to characterize the Bi concentration not only for InPBi, but also for Bi-related quaternaries such as InGaPBi and InAlPBi.

Optical Property

InPBi shows broad and strong PL at RT, with the PL peak far away from the band edge emission shown in Figure 11a. Theoretical calculations predict that the bandgap reduction by Bi incorporation into InP is about 106 meV/% Bi with 27 meV/% Bi downshift for CB and 79 meV/% Bi upshift for VB [161]. The PL spectrum consists of three peaks originated from two deep levels confirmed by deep level transient spectroscopy (DLTS) [161], in which one is P_{In} antisite related donor level below the CB and the other is Bi related acceptor level above the VB. The three peaks labeled as low energy (LE), middle energy (ME) and high energy (HE), respectively are attributed to recombination between the P_{In} antisite level and the Bi related level, the P_{In} antisite level and VB, and CB and the Bi related level, respectively.

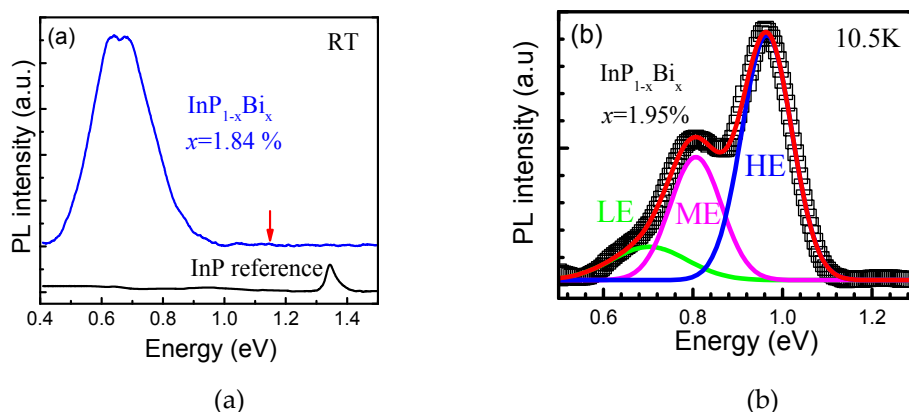


Figure 11. (a) Room temperature photoluminescence (PL) spectra of InPBi and InP. The red arrow is the band edge emission of InPBi bulk material. (b) PL spectrum of InPBi measured at 10.5 K. The frame line is the measured spectrum and the red solid line is the overall fitted spectrum while the green, pink and blue solid lines are fitted spectrum for low energy (LE), middle energy (ME) and high energy (HE), respectively.

InGaPBi and InAlPBi

InGaPBi and InAlPBi have been successfully grown by gas source MBE based on the growth parameter window for InPBi. InAlPBi grown on GaAs substrate has the highest Bi content up to 1.6% and the strain can be controlled from tensile to compressive by adjusting the Al and Bi contents simultaneously. InGaPBi films are grown on GaAs and InP substrates with the highest Bi content of 1.8% and 2.2%, respectively. By adjusting Ga and Bi flux, the strain between the InGaPBi epi-layer and the substrate can also be tuned from tensile to compressive as shown in Figure 12. The as grown InGa(Al)PBi shows strong and broad PL similar to InPBi, which provides a new way to extend the potential application of InGa(Al)P based devices.

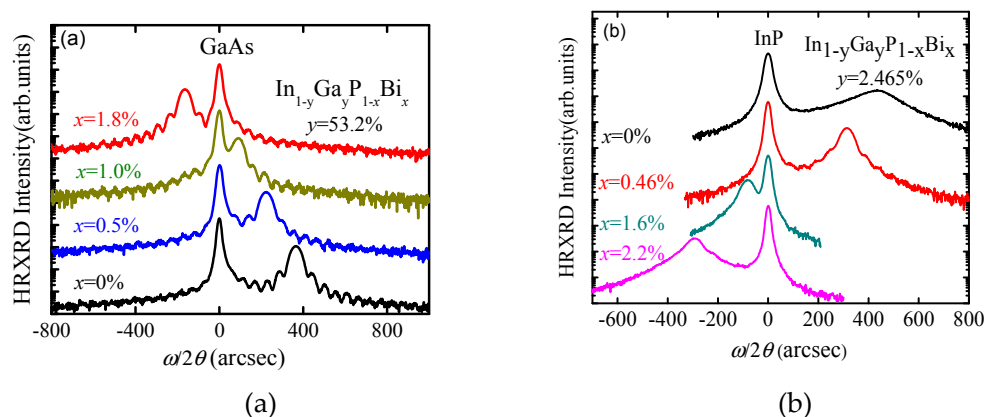


Figure 12. XRD rocking curves of InGaPBi films grown on (a) GaAs, Reproduced from Reference [162], Copyright 2015 by the Japan Society of Applied Physics; and (b) InP, Reproduced from Reference [117].

N-Bi Co-Doping Phosphides

Co-doping of N and Bi atoms can effectively reduce the matrix bandgap, meanwhile improve the carrier mobility reduced by incorporating N alone. Moreover, the lattice mismatch caused by the small atomic size of N atoms substituting group-V could be balanced by the large size of Bi atoms. Kuznetsov et al. affirmed the mutual enhancement in corporation of N and Bi by co-doping both atoms simultaneously in GaP [37]. N and Bi isoelectronic co-doping could be used to benefit the potential application of optoelectronic devices based on GaP, InP, InGaAs and other III-Vs, such as LEDs, lasers and solar cells.

5.3. III-As-Bi

5.3.1. InAsBi

InAs is an attractive semiconductor for application in photodetectors with a direct bandgap energy of 0.36 eV, corresponding to a cutoff wavelength of 3.4 μm . The giant bowing effect and temperature insensitive bandgap of dilute bismide have inspired researchers to synthesize and investigate InAsBi, pushing IR photodetectors operating within the 3–5 μm and 8–12 μm spectral range. The bandgap reduction is reported at a rate of approximately 55 meV% Bi [25]. Thus, theoretically only 6% Bi is required in InAsBi to achieve a bandgap of 0.1 eV, equivalent to a wavelength of 12.4 μm . Nevertheless, the small solubility of Bi in InAs poses a great challenge for InAsBi alloy with a high Bi content. Thermodynamic calculations of the InAs-InBi pseudo-binary phase diagram show that the solid solubility of Bi in InAs is no more than 0.025% [26]. Nonetheless, the first MOCVD growth of InAsBi revealed a Bi concentration as high as 2.6%, far exceeding the theoretical value [25]. Using ultra-low temperature MOCVD method, Ma et al. achieved a Bi concentration up to 6.1% at 275 $^{\circ}\text{C}$, the lowest temperature ever used for InAsBi growth [163]. Before 2012, InAsBi were all grown using MOCVD by two groups: from Oe's group in Japan and Stringfellow's group in USA [25,85], respectively. MBE has been used recently to grow InAsBi alloys [164] and becomes gradually popular.

Epitaxial Growth of InAsBi

InAsBi was first grown by Ma et al. on a (100) InAs substrate by MOCVD [25]. Good surface morphology with a Bi content of 2.6% is achieved at a growth temperature of 400 $^{\circ}\text{C}$. The V/III ratio is considered to be the key factor and only a very narrow range of V/III ratio near 4 (considering only 30% pyrolysis of AsH_3 at 400 $^{\circ}\text{C}$) yields a smooth InAsBi epilayer. Thus, the effective V/III ratio is equivalent to 1.2, approaching to the stoichiometry condition like the case for GaAsBi growth. In contrast, for MBE grown InAsBi, a haze-free surface of InAsBi alloys is realized at an As/In flux ratio of 1:1.1 [164]. This indicates that either MOCVD or MBE growth of InAsBi needs a critical control

of V/III ratio near the stoichiometry of unity. Growth temperature is also a critical factor during growth and affect decomposition rate of As precursor. Commonly, the growth temperature of InAsBi is controlled within 350–400 °C by MOCVD [25,26]. At 375 °C, Ma et al. achieved InAsBi alloy with a Bi content of 4% in 1991 [26]. In the same year, they decreased the growth temperature down to 275 °C and obtained the highest Bi concentration of 6.1% [165].

MOCVD grown InAsBi is a metastable alloy, only an appropriate control of growth conditions can lead to a single-phase crystal. Consequently, growth conditions greatly affect surface morphology. In Okamoto's study [158], three types of surface morphologies: mirror-like, droplets and whiskers, were observed. For the mirror-like samples, the InAsBi epilayer has a smooth surface with the highest InBi content of 3%–4%. Mirror-like surfaces become more obvious at lower InBi contents and the corresponding InBi composition is nearly proportional to the TMBi/V ratio. For samples with droplets on surface, SEM investigation demonstrates three components: a spherical part consisting of metallic Bi, a second plain part with less Bi and a third part with almost the same Bi content as the second part formed by vapor-liquid-solid (VLS) growth with liquid Bi. Whiskers on InAsBi surfaces tend to form when TMBi and TBAs both are at high values. Whiskers are deemed to form by VLS growth when two conditions are satisfied: Bi droplets could not become large limited by the short migration length of decomposed TMBi due to the high As pressure, and the large TMBi pressure makes the Bi droplets small but still larger than the critical nucleus with a high density. A similar whisker surface on InAsBi sample was also found in Ma's study [26]. It is explained as the presence of a liquid InBi phase on the growing surface which can be speculated by the calculated pseudobinary phase diagram for InAs–InBi.

One advantage of the RBS channeling measurement is the possibility of verification of Bi atom positions in an InAs ZB lattice. In Okamoto's study [158], more than 90% of the Bi atoms were substitutionally incorporated into the InAs ZB lattice by replacing As sites. Later, Verma et al. [166] used Raman spectroscopy and confirmed existence of InBi vibrational modes which was proportional to the Bi content. This indicates that with increasing the Bi content, more Bi atoms replace As lattice sites, in agreement well with Okamoto's conclusion.

In 2012, InBi crystals were initially grown by Dominguez et al. [124] using MBE growth. In their study, Bi incorporation in InAsBi/InAs (100) is analyzed through advanced TEM techniques. It is found that samples grown within 350–400 °C result in Bi contents below 3.3%. The Bi content in these samples is distributed inhomogenously. Clear Bi segregation to the InAs/InAsBi/InAs interface is observed, but still no Bi clusters occur. Nevertheless, the sample with more than 4% Bi exhibits rough and spherical clusters in different sizes. Indirect EDX investigations verified the clusters are made of binary InBi in different positions of the epilayer. These InBi clusters occur in Bi-rich samples, probably due to the inability of Bi be totally assimilated by InAs. The InBi clusters are found to be surrounded by an InAsBi matrix with a Bi content as high as 4.8%.

Properties of InAsBi

In 1987, Barnett et al. calculated that the bandgap of InAsBi alloy reduces with increasing Bi concentration at a rate of 20.3 meV/%Bi at 77 K using the quantum dielectric theory [167]. However, experimental results from Ma et al. evidenced a value of 55 meV/% Bi, more than double the value of the theoretical estimation. Figure 13 displays the dependence of PL peak energy on InBi molar fraction at 10 and 300 K, respectively [168].

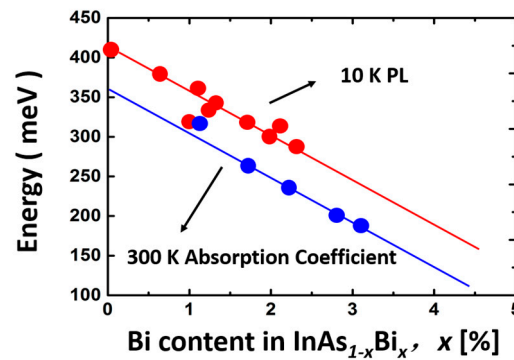


Figure 13. Photoluminescence peak energy and absorption edge vs. Bi composition at 10 and 300 K, respectively. The slopes are close to 55 meV/% Bi for both results. Reproduced from [168] [Photoluminescence of InAsBi and InAsSbBi grown by organometallic vapor phase epitaxy], with the permission of AIP publishing.

Temperature dependent bandgap of InAsBi alloy with a Bi content of 1.8%, 2.2%, 3.2% and 3.7% was investigated in Okamoto's study using optical-transmission measurement [169] shown in Figure 14. Lines are linear fittings between 140 and 340 K. According to the slopes of the fitting lines, one can conclude that the bandgap of InAsBi decreases with enhanced InBi molar fraction. For InAsBi_{0.037} the $\Delta E_g/\Delta T$ is 0.22 meV/K. In spite of the common tendency that a smaller E_g also exhibits a smaller $\Delta E_g/\Delta T$ in nature, the value of 0.22 meV/K is smaller than that of InSb (0.29 meV/K), whose E_g is smaller than that of InAsBi. This indicates that Bi incorporation has an effect on decreasing $\Delta E_g/\Delta T$.

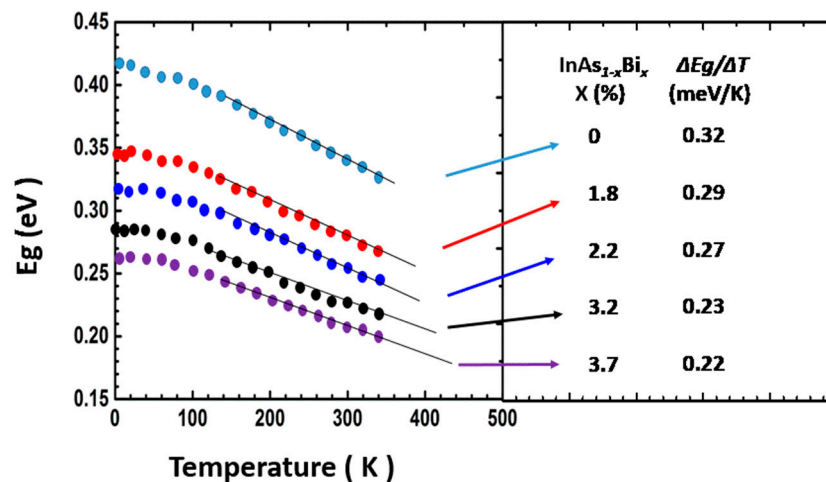


Figure 14. Temperature dependence of the bandgap of various InAsBi layers. Reproduced from Reference [169].

5.3.2. InGaAsBi

InGaAs alloy, which is widely used as a fundamental material in photonic devices, is expected to be turned into a promising temperature-insensitive semiconductor In_xGa_{1-x}As_{1-y}Bi_y with a narrower bandgap than GaAsBi by Bi incorporation. In addition, by adjusting the x, y compositions, one can obtain the desired bandgap suitable for device application and lattice matched to InP substrate at the same time. A theoretical cutoff wavelength of InGaAsBi is predicted to reach as long as 6 μm , further extending the wavelength to the mid-IR regime [64].

Epitaxial Growth of InGaAsBi

In 2005, the first InGaAsBi quaternary alloy was grown on InGaAs buffer layer on an InP substrate by Feng et al. [170] using MBE at 275–350 °C with a growth rate of 0.4 µm/h. Good crystalline quality with 2.5% Bi is confirmed by XRD. Bi atoms are found to be incorporated substitutionally on the InGaAs ZB lattice sites by RBS channeling spectrum. Two years later, the same research group investigated temperature dependence of Bi behavior during MBE growth. A maximum of 6% Bi concentration is achieved at a growth temperature as low as 260 °C. Growth at a high temperature of 450 °C, normal for InGaAs epitaxy growth, reveals no detectable Bi incorporation but the decreased surface roughness from 1.067 to 0.328 nm. Monitoring the growing with and without Bi irradiation by RHEED, they discovered a spotty to streaky RHEED pattern transformation immediately when Bi is supplied during growth, while for samples grown without Bi irradiation, 2–3 min (~30 ML) is needed for this transformation. This confirms that Bi acts as a surfactant, modifying the growth mode from 3D to 2D in the beginning of growth [158]. Up to now, the highest Bi concentration in InGaAsBi is reported to be 7% [171], and a low growth temperature and a moderate As/Bi flux ratio are deemed in favor of Bi incorporation [172].

Properties of InGaAsBi

When Bi is added into InGaAs, a much narrower bandgap is expected to be achieved than GaAsBi [173]. For traditional InP-based InGa(Al)As lasers, the bandgap is larger than the SO split energy which enhances the Auger recombination process involving these energy bands. This is detrimental for device performance [174]. Auger recombination is expected to be suppressed in InGaAsBi by engineering the bandgap and the SO splitting. A bandgap reduction effect of 56 meV/% Bi was first observed by Petropoulos et al. [62] Using VBAC model [126], the bandgap and SO splitting of InGaAsBi alloys latticed-matched to InP can be tuned by adjusting In and Bi compositions and are plotted in [68]. The calculated bandgap of this quaternary material is not linearly dependent on either Bi (x) or In (y) composition, and decreases with increasing Bi or In composition. A theoretical cutoff wavelength of about 6 µm is also predicted.

Continuing an in-depth study on the E_0 and $E_0 + \Delta_{SO}$ transitions of the same InGaAsBi samples [64], Kudrawiec et al. [175] found that the E_0 transition redshifts (~50 meV/% Bi) with Bi content. The observed transitions are explained by VBAC model [126] and common anion rule [131]. According to the VBAC model, Bi incorporation in InGaAs only has an influence on the VB. Thus, the observed transitions are interpreted as that the heavy/light hole band shifts upward, while both the CB and the SO split band keep unchanged as illustrated in Figure 15. These results are also in agreement with the common anion rules, based on which energy gap decreases when light anions are replaced by heavy Bi atoms. Incorporation of heavy Bi atoms into InGaAs host results in a decrease in energy bandgap and an increase in SO split energy, while the sum of the $E_0 + \Delta_{SO}$ transition is kept the same. Such modification of Bi on band structure of InGaAs can effectively eliminates Auger recombination sketched in Figure 15 and make InGaAsBi as an attractive gain medium suitable for temperature-insensitive telecom lasers.

For GaAsBi, the temperature dependence of bandgap is reported to be weaker than that of GaAs [176]. For InGaAsBi alloy, it is controversial. Devenson et al. found a similar trend as in GaAsBi but did not quantify the value [177]. Hosea et al. quantified this value of about 0.33 ± 0.07 meV/K by PL and PR measurements which is independent upon Bi concentration [178]. Contrary to these results, Yi et al. [116] discovered that incorporating Bi into InGaAsBi/GaAs QW could extensively improve PL intensity and emission wavelength, but not the temperature sensitivity of bandgap. This unexpected behavior from the Bi-containing QW is attributed to a small Bi content of only 0.6%. Overall, change of the temperature sensitivity of the InGaAsBi bandgap is relatively small compared with GaAsBi.

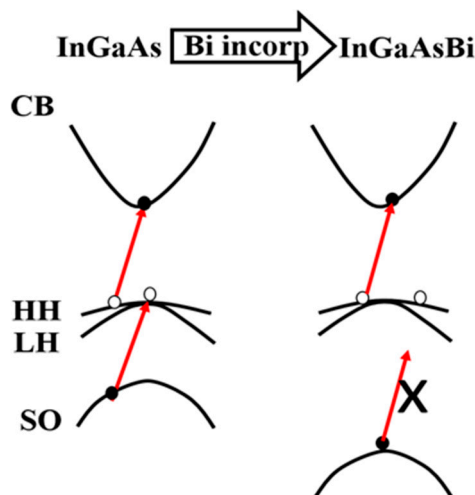


Figure 15. Sketch of Bi-related changes in the band structure of InGaAsBi alloys.

5.4. III-Sb-Bi

5.4.1. InSbBi and Quaternary Alloys

InSbBi is the first studied dilute bismide with the attempt to reach long-wavelength IR (8–12 μm) region where the dominant material choice is HgCdTe. InSbBi has been successfully used as infrared photodetectors with a cutoff wavelength at 10.6 μm [30]. The first synthesis of InSbBi bulk material was realized using Czochralski (CZ) method by Jean-Louis et al. [15] in 1969. In 1981, Oe et al. [21] reported the first MBE growth of InSbBi thin films with smooth surface. The Bi incorporation is increased by slightly reducing the Sb/Ga ratio in the range near unity. Use of a low temperature is found to favor the Bi incorporation. A maximum Bi content of 5% is achieved when grown at 250 $^{\circ}\text{C}$. Song et al. [179] have grown InSbBi films on GaAs substrate using MBE and achieved 2% Bi [180] incorporation. Secondary ion mass spectroscopy (SIMS) measurements demonstrate a high In component in GaSb region and a high Ga component in InSb region as a result of In-Ga intermixing induced by Bi. The bandgap of InSbBi film is confirmed to shift to long wavelengths with Bi content by measuring photovoltaic response of a p - n junction. The bandgap reduction determined by optical absorption measurements is about ~ 35 meV/% Bi [181]. InSbBi is also grown by MOCVD [24,29,182]. Lee et al. [183] used low pressure MOCVD and obtained InSbBi films on InSb substrate. The bandgap of InSbBi is reduced to 0.13 eV (~ 9.3 μm) at 77 K. Besides, Wagener et al. [29,184] found the secondary phases formed during the MOCVD growth and the formation is influenced by the V/III ratio. InBi and In_2Bi phases are formed on surface as the V/III ratio is slightly below the stoichiometry of unity, whereas BiSb phases are formed when it is slightly above the stoichiometry of unity. There are a few reports on the growth of InSbBi by LPE. For example, Iwanowski et al. [28] grew InSbBi layers by LPE with a Bi content of 0.5%. Dixit et al. [181] reported growth of InSbBi with a Bi content up to 4% by LPE on GaAs substrates.

Finally, Ma et al. [25,168] used MOCVD to grow quaternary $\text{InAs}_{1-x-y}\text{Sb}_y\text{Bi}_x$ alloy with $x \leq 0.017$ and $y \leq 0.096$. From PL spectra measured at 10 K, the bandgap reduction of InAsSbBi is determined as 55 meV/% Bi with increasing Bi concentration. Other quaternary alloys like GaInSbBi was reported by Du et al. [185] using MBE on InSb substrates. The introduction of Ga into InSbBi alloy can enhance Bi incorporation, improve lattice-matching to InSb, suppress multiple-phase growth and improve surface morphology. Infrared absorption measurements of $\text{Ga}_{0.04}\text{In}_{0.96}\text{Sb}_{0.97}\text{Bi}_{0.03}$ film performed at 77 K indicate a cutoff wavelength as long as 10.7 μm .

5.4.2. GaSbBi

Researches on GaSbBi materials lag far behind than that of GaAsBi, InAsBi, InGaAsBi and InSbBi. In 2011, GaSbBi alloys were firstly grown by MBE [10] and LPE [186] with a Bi content of 0.8% and 0.4%, respectively. In 2013, Rajpalke et al. [187] acquired GaSbBi films with a Bi content up to 5% by decreasing growth temperature from 350 to 250 °C using MBE. Efforts have been applied to increase Bi incorporation into GaSb including reducing growth rate [188] and increasing Bi flux [166]. Duzik et al. [131] reported GaSbBi films with a Bi content reaching 12%, but very large Sb/Bi droplets segregated on the surface and unintentional incorporation of 9% As are also observed. Rajpalke et al. [166] investigated the effect of growth rate on Bi incorporation and obtained 9.6% Bi content by varying the growth rate from 0.31 to 1.33 $\mu\text{m}/\text{h}$ at 250–275 °C. The Bi content is found to be inversely proportional to the growth rate.

The band structure and optical properties of GaSbBi alloys have been explored by absorbance and PR spectroscopy [189,190]. The bandgap reduction of GaSbBi is deduced as about 30%–36% $\text{meV}/\% \text{Bi}$. Jan et al. [191] investigated temperature-dependent PL spectra of $\text{GaSb}_{1-x}\text{Bi}_x$ layers with $0 < x \leq 0.042$ and observed two peaks. The high energy (HE) peak is related to the bandgap emission in GaSbBi and redshifts at a rate of 29 $\text{meV}/\% \text{Bi}$ at 150 K, in consistent with the bandgap shift determined from PR measurements. The low-energy (LE) peak is due to the optical transition between CB and the native acceptor states observed at low temperatures where acceptor states are not occupied by electrons. For high Bi content GaSbBi alloys, Rajpalke et al. [166] are the only researchers to have reported absorption and PL spectra with a Bi content up to 9.6%. A weak PL from the GaSbBi sample with 9.6% Bi is observed at 4 K with a transition energy of $490 \pm 5 \text{ meV}$. Absorption spectrum measured at RT on the same sample reveals an absorption edge of $410 \pm 40 \text{ meV}$ (corresponding wavelength of 3.0 μm), indicating GaSbBi alloys as a promising candidate for mid-IR applications.

5.5. Other Quarternary Bismides

5.5.1. GaNAsBi

Traditional InGaAsP telecom lasers show a large temperature dependent bandgap and require a cooler to stabilize device temperature and thus the lasing wavelength. GaAsBi alloys are reported to have a smaller temperature coefficient of bandgap than that of GaAs [179]. Together with the large bandgap reduction of 88 $\text{meV}/\% \text{Bi}$ [192], all make GaAsBi a promising material for uncooled telecom lasers on GaAs. However, the large Bi atom makes GaAsBi lattice mismatched to a GaAs substrate and it is difficult for GaAsBi to reach emission wavelength at 1.3 and in particular 1.55 μm . Introducing N into GaAsBi is expected to solve these problems due to its flexibility of strain tuning to lattice matched to GaAs, separate control of electron and hole confinements, and more effective to realize wavelength redshift [193]. GaNAsBi has been successfully grown by MBE with a Bi content of 4% and an N content of 8% in 2004 [194] for the first time. Room temperature emission wavelength at 1.3 μm has been demonstrated from GaNAsBi epilayer lattice matched to GaAs substrate. The highest Bi content of 4.7% in GaNAsBi was achieved by Wei et al. in 2005 [134].

Epitaxial Growth of GaNAsBi

Like GaAsBi, GaNAsBi epitaxy growth is determined by As flux, growth temperature, Bi supplying and growth rate. Up to now, GaNAsBi has been grown mostly by MBE except for Bushell's group who used MOCVD method [195]. In MBE, As flux can be well controlled to guarantee a considerable amount of Bi incorporation as well as a good surface quality judging by RHEED. When As supply is insufficient, a spotty RHEED pattern or only diffusive RHEED background will be observed. Accordingly, the surface of the grown epilayer is hazy and rough. However, excess As will expel Bi incorporation as detected by RBS measurements. In this condition, a ternary GaNAs will be grown instead of GaNAsBi, although a streaky RHEED pattern and a smooth epilayer surface can still be obtained. With the optimized As supply, a (2×4) reconstruction will be seen from the

RHEED pattern during GaAs growth. It changes to a (2×1) streaky pattern during GaNAsBi growth. Huang et al. reported an optimized As flux of $\sim 3.5 \times 10^{-6}$ Torr for a Ga flux of $\sim 2 \times 10^{-7}$ Torr [134]. They also found a mirror surface without any Bi droplets for GaNAsBi epilayers grown with this optimized As flux at 350–400 °C. The GaBi molar fraction decreases linearly with increasing growth temperature when other growth parameters are held constant.

One may question whether the N supply will affect the Bi content or not. In Bushell's work [195], N content was found to increase linearly with increasing N supply. In contrast, Bi concentration was discovered to be independent of N supply and the N content was high in the samples with a low Bi content for a given N:As flux ratio. The independent Bi incorporation upon the N supply was also observed in Huang's study [134].

The growth rate of GaNAsBi is related to Bi supplying during growth. Bushell et al. [195] found a decrease of GaNAsBi growth rate with increasing Bi supply. It is interpreted that an increased Bi surface coverage could decrease the atoms diffuse to the growth surface or the decomposition of precursors. Both would suppress the N incorporation. In addition, an increased Bi and N competition for group V lattice sites also results in reduction of the N incorporation.

Properties of GaNAsBi

A small quantity of N can induce a large downward shift of the CB edge, and dilute Bi atoms can also result in a large upward shift of the VB edge. It is therefore expected that the PL peak energy of GaNAsBi will largely redshift with increasing GaBi and GaN molar fractions. The redshift coefficients of ~ 62 meV/% Bi and ~ 130 meV/% N for GaNAsBi from RT PL peak energy were reported by Huang et al. [134]. By adjusting GaBi and GaN molar fractions, they found $\text{Ga}(\text{N}_{0.33}\text{Bi}_{0.67})_z\text{As}_{1-z}$ to be lattice matched to GaAs substrates and the ratio of GaBi and GaN molar fractions is consistent with theoretical values based on Vegard's Law [196] assuming the lattice constant of GaAs, GaBi [113] and cubic GaN as 5.65, 6.23 and 4.51 Å, respectively. The PL peak energy of $\text{Ga}(\text{N}_{0.33}\text{Bi}_{0.67})_z\text{As}_{1-z}$ alloys at RT can reach 0.8 eV (1550 nm) for $z = 6.5\%$.

Temperature dependence of the PL peak energy for GaNAsBi is found to be small. Figure 16 shows the PL peak energy from GaNAsBi with different Bi compositions of 4.7%, 3.7% and 2.0%, respectively, and the same N content of 2% at 150–300 K [134]. In comparison, an $\text{In}_{0.68}\text{Ga}_{0.32}\text{As}_{0.69}\text{P}_{0.31}$ reference alloy is also plotted. The temperature coefficient of the PL peak energy is determined to be 0.12, 0.14 and 0.16 meV/K for the Bi content of 4.7%, 3.7% and 2.0%, respectively, much smaller than that of $\text{In}_{0.68}\text{Ga}_{0.32}\text{As}_{0.69}\text{P}_{0.31}$. It is therefore deduced that the temperature dependence of bandgap for $\text{GaN}_y\text{As}_{1-x-y}\text{Bi}_x$ is governed by the GaBi molar fraction, irrelevant of the GaN molar fraction.

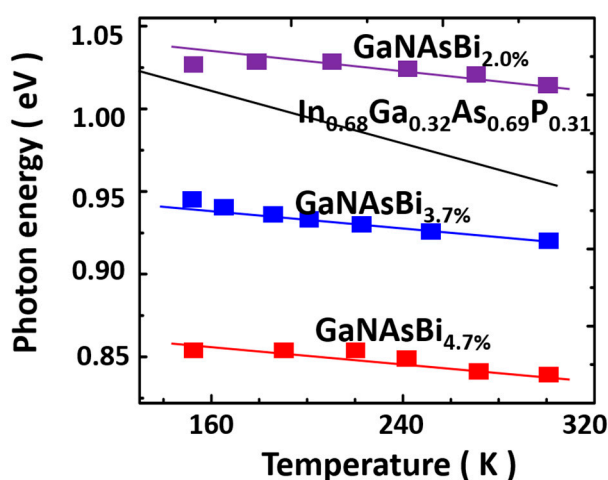


Figure 16. PL peak energy of GaNAsBi and $\text{In}_{0.68}\text{Ga}_{0.32}\text{As}_{0.69}\text{P}_{0.31}$ as a function of measured temperature. Reproduced from Reference [134].

Photoluminescence efficiency of other N-containing materials such as GaNAs and GaInNAs are reported to be significantly affected by the N incorporation. Without exception, it was reported that N incorporation deteriorated PL efficiency for GaNAsBi [195]. The N-related non-radiative defects such as N interstitials and Ga vacancies are thought to account for the PL intensity reduction. Thermal annealing is an effective method to improve PL intensity in GaNAsBi, without notable variation of the PL peak energy [197].

5.5.2. BGaAsBi

Earlier studies have employed N co-doping to reduce strain in GaAsBi [134,195]. However, the introduction of N causes undesirable N-related non-radiative defects which badly affect PL efficiency of GaNAsBi. Boron is the smallest atom in group III and co-doping with Bi in GaAs is expected to compensate strain in GaAsBi, while not inducing notable changes of optoelectronic property. Up to now, there are only two reports about the BGaAsBi quaternary alloy, one on epi-growth of BGaAsBi [198] and the other on theoretical calculations on structural and electronic properties [199].

In 2012, Daniel et al. reported the first successful growth of $B_yGa_{1-y}As_{1-x}Bi_x$ lattice matched to GaAs by solid-source MBE [198]. $B_yGa_{1-y}As_{1-x}Bi_x$ was grown on semi-insulating (001) GaAs substrates at 320 ± 5 °C, favorable for growth of high quality of GaAsBi films [122,129], but not the optimal growth conditions for B incorporation [200]. The Bi content is kept the same as 1.6% while the B content increases from 0 to 1.2%. The compressive strain of BGaAsBi decreases with increasing B content. For $y = 1.2\%$, the $B_yGa_{1-y}As_{1-x}Bi_x$ is lattice match to GaAs substrate. Distinguished fringes are observed in HRXRD indicating that all the epilayers are pseudomorphically strained to the GaAs substrate with a smooth interface. SIMS investigation combined with HRXRD results reveals that most B atoms are substitutional, while excess B atoms are probably interstitial [200], or possibly exist in forms of B-B or B-As complexes [201]. Room temperature PL measurements show no significant change in peak energy with increasing B content. The excess B atoms incorporated at non-substitutional sites lead to a high density of bandgap tail states which affect the temperature dependence of the bandgap in BGaAsBi. Specifically, the ability of Bi-related defects to trap carriers is diminished by increasing B atoms. Thus, a very weak temperature dependence of bandgap is presented in the lattice matched $B_yGa_{1-y}As_{1-x}Bi_x$ alloys.

Aslan et al. presented theoretical calculations on structural and electronic properties of BGaAsBi in 2015 [199]. In this paper, structural and electronic properties of cubic BGaAsBi alloys with a Bi content of 0.0625, 0.125, 0.1875 and 0.25 are studied based on DFT. The calculated results reveal that the lattice constant of BGaAsBi alloys varies linearly with B concentration, whereas the Bi composition variation causes a nonlinear behavior on lattice constant. In addition, effect of Bi and B on bandgap of BGaAsBi alloy is also different. Increasing Bi concentration decreases the bandgap of BGaAsBi while increasing B concentration results in the bandgap of BGaAsBi changing from a direct band to an indirect band mainly due to that B atoms push the X-valley downward. Band offset calculations show that CB offset increases with increasing B and Bi concentrations, but VB offset decreases.

6. Physical Properties of Dilute Bismides

6.1. Surface and Structural Properties

6.1.1. Surfactant Effect and Segregation

Bismuth is widely known as an eminent surfactant to improve morphology of III-V semiconductor compounds during growth at high temperatures. To act as a surfactant, there have to be enough Bi atoms impinged onto the matrix material [202]. If the Bi content is too high or the growth temperature is too low, Bi tends to segregate and even form droplets on the surface, deteriorating the material morphology. Meanwhile, the lattice mismatch will be too large to maintain good crystal quality. Figure 17 shows XRD of InPBi films with various Bi contents. There are clear XRD interference fringes

of InPBi with Bi content of 1.84% and 2.39%. However, no interference fringes are found for both low and high Bi contents.

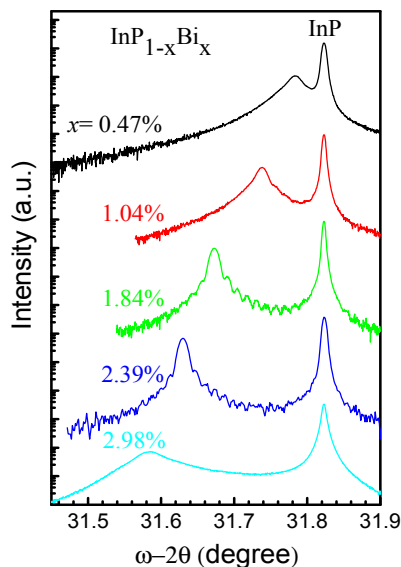


Figure 17. XRD of InPBi with different Bi contents.

There is high chemical driven force for phase segregation and droplet formation in dilute bismides. Even for dilute bismides that are nominally free of droplets on surface, there still may be a high tendency for droplet formation. Sales et al. studied the distribution of Bi in GaAsBi epi layers with a Bi content of 2.65% by STEM. They investigated Bi content column by column and the results indicated that Bi atoms were distributed homogeneously but there were certain areas showing nano-clustering [203]. Sterzer et al. discussed the surface droplets for MOCVD grown GaAsBi [123] and pointed out the droplets were formed during growth, and then migrated and merged with the surrounding Bi droplets to form droplet clusters. The droplets could be Bi and/or Ga-Bi metallic droplets, depending on the As/Bi ratio. The shape, size and distribution of the droplets highly depend on growth temperature. Droplet density is low, but size is large at high growth temperatures due to enhanced surface diffusion.

6.1.2. Lattice Constant

Because Bi has the largest atomic size in the group-V elements, substitution of Bi for other group-V elements will stretch the lattice of the matrix. However, abnormal lattice contraction has been found in GaSbBi [204], GaAsBi [141] and InPBi [205] due to vacancy formed by Bi segregation. To make sure of Bi incorporation, a low growth temperature is necessary. However, there tend to be more defects in material grown at low temperatures, such as VIII antisites and vacancies. These native point defects will assist diffusion of Bi and other group-V elements, causing Bi clusters and/or V clusters.

Takehara et al. deduced the lattice constant for fully relaxed GaAsBi with the relationship of $a_0(\text{\AA}) = 5.6535 + 5.77 \times 10^{-3}x(\%)$ [206]. The lattice constants for GaBi and InBi from different works are list in Table 6. Bismuth is widely believed to substitute group-V in the matrix. However, Kunzer et al. confirmed that about 10 % of the incorporated Bi had occupied the Ga sites in GaAsBi films [207].

Table 6. Lattice constant for GaBi and InBi.

Alloy	GaBi	InBi
	6.23 Å [204]	6.5 Å [158]
	6.272 Å [167]	6.686 Å [203]
	6.33 Å [141]	7.024 Å [26]

6.1.3. Lattice Structure

III-V semiconductors are mostly crystallized in ZB or WZ structures, but the ground state structure of III-Bi alloys is rarely known. First principle studies predict that the light III-Bi alloys such as BBi, AlBi and GaBi stabilize in ZB structure. However, tetragonal PbO structure is the most stable structure for the heavy III-Bi such as TlBi and InBi [104,208]. Still, In-V-Bi compounds could be successfully grown with InBi in ZB structure under a proper growth condition. Wu et al. studied structure of Bi clusters in annealed GaAsBi films [110]. Due to phase separation, Bi-containing clusters are easily formed and the initial Bi rich ZB Ga(As,Bi) could transform to rhombohedral Bi clusters in ZB {111} planes until complete depletion of Bi atoms in the GaAs matrix.

Atomic ordering is an important spontaneous process in semiconductors especially in the III-Vs which is highly related to surface reconstruction. Ordering will affect the band structure due to the Brillouin-zone folding effect, thus changing the physical properties of the material. CuPtB type, CuPtA type and triple-period A (TP-A) ordering are widely observed [209] while triple-period B (TP-B) was first observed in GaAsBi by Wu et al. through HRTEM [210]. The A-variants correspond to the ordering in $[111]$ and $[\bar{1}\bar{1}\bar{1}]$ while the B-variants refer to the ordering in $[\bar{1}11]$ and $[1\bar{1}\bar{1}]$ directions. Reyes et al. studied the ordering in GaAsBi films and pointed out that the ordering would be reduced in the material with decreasing Bi content [211]. Growth of GaAsBi on a (2×1) reconstruction surface is found to be anisotropic, accompanied with a continuous increase of the density of atomic steps which create an undulating surface in the end. Bismuth atoms tend to incorporate in GaAs matrix and stick on the surface on CuPtB ordered and undulated GaAsBi, respectively. Wu et al. found both TP-A and TP-B ordering existed in low temperature grown GaAsBi material [210] while most other work only observed the TP-A ordering. They claimed that the TP-A ordering was dominant with a large size and clear ordering comparing to the TP-B ordering. While the TP-A ordering is related to $(n \times 3)$ surface reconstruction, the coexistence of TP-A and TP-B ordering is deduced to be connected with the mixed $(n \times 3)$ and $(3 \times n)$ surface reconstruction.

Raman spectra are measured on GaAsBi, InAsBi and InPBi films. For GaAsBi and InAsBi grown by MOCVD [212], there is a Bi-related peak at $\sim 140 \text{ cm}^{-1}$ in both spectra, and the intensity of this Bi-related vibration mode is much stronger in GaAsBi than that in InAs. Verma et al. theoretically calculated the GaBi-like TO and LO mode at 196 and 189 cm^{-1} , respectively, and the InBi-like TO and LO mode at 161 and 155 cm^{-1} , respectively, of which all the intensities enhance with increasing Bi content. For InPBi films, two modes at 149 and 171 cm^{-1} are deduced to be InBi-like TO and LO phonon modes, respectively, which are linear to the Bi content at 0.3%–2.3% [159].

6.2. Electronic and Transport Properties, Point Defects

Intensive and extensive studies have been directed to understanding the effects of Bi incorporation on electronic and transport properties III-V alloys, for instance, electronic band structure, mobility, carrier effective masses, impurity states, impurity-host interaction, and their evolution with Bi-concentration.

6.2.1. Electronic Properties

Incorporation of Bi induces a bandgap reduction and strong increase in the SO split. Based on the VBAC model proposed by Alberi et al. [59], the incorporation of Bi into GaAs introduces Bi defect

states, which are located close to the VB edge of GaAs. The interaction between these states with VB results in a splitting of the VB to two sub-bands which are given by

$$E_{C,V}[\text{GaAs}(\text{Bi})] = \frac{E_{C,V}(\text{GaAs}) + E_{Bi} \mp \sqrt{[E_{C,V}(\text{GaAs}) - E_{Bi}]^2 + 4C_{Bi}^2 x}}{2} \quad (6)$$

$$E_V = \begin{cases} E_{V,aV} + \frac{\Delta_{SO}}{3} + \delta E_{hh}, & hh \\ E_{V,aV} + \frac{\Delta_{SO}}{3} + \delta E_{lh}, & lh \end{cases} \quad (7)$$

where $E_{C,V}(\text{GaAs})$ is the energy of the CB minima (CBM) or the VB maxima (VBM) of GaAs, E_{Bi} is the energy of the Bi resonant level, x is the Bi concentration and C_{Bi} is the coupling between the Bi resonant level and the GaAs VBM. The VBAC model treats Bi atoms as isoelectronic impurities to the host anion species. These impurities act as localized states in the host semiconductor. The interaction between these localized trap states and the host semiconductor band brings changes in the band structure. The VBAC model has been extensively used to study the band structures of the $\text{GaAs}_{1-x}\text{Bi}_x$ alloys [58,67,153,213,214]. Prediction has indicated that dilute bismide alloys are promising to realize the SO split energy Δ_{SO} exceeding the bandgap energy E_g for suppressing non-radiative Auger recombination and IVBA [53].

Contactless electroreflectance (CER) spectroscopy is an excellent technique to study the energy gap and the SO splitting in III-V semiconductors. CER spectroscopy has been used to measure energy of the optical transitions in the vicinity of the fundamental bandgap of GaAsBi. Francoeur et al. [192] reported the bandgap of GaAsBi epitaxial layers as a function of Bi concentration up to 3.6% using CER. The bandgap energy decreases at a rate of 88 meV/% Bi, or 83 meV/% Bi for the heavy hole to CB transition for GaAsBi strained to GaAs. The Bi induced upward motion of the heavy and light hole bands leads to the large bandgap reduction. The increasing rate of VB splitting in GaAsBi is faster than that of GaAs under the similar compressive strain.

Photoreflectance (PR) spectroscopy, due to its high sensitivity to critical point transitions in a band structure, is an excellent technique to study band structures of highly mismatched alloys. Polak et al. [189] used PR spectroscopy and ab initio calculations to study electronic band structure of $\text{GaSb}_{1-x}\text{Bi}_x$ alloys with $x_{Bi} < 5\%$. These calculations show that the incorporation of Bi atoms into GaSb host affects both the CB and VB. PR results are in good agreement with the theoretical calculations. The shift rate is -26.0 meV/% Bi for the CB and 9.6 meV/% Bi for the VB, respectively. So, the total bandgap reduction is 35.6 meV/% Bi as shown in Equation 8.

$$E_g^{\text{GaSb}_{1-x}\text{Bi}_x} = (1-x) E_g^{\text{GaSb}} + x E_g^{\text{GaBi}} - b(1-x)x \quad (8)$$

where b is the bowing parameter. From both PR spectroscopy and the theoretical calculations, the bowing parameter is derived as $b = -1.0 \pm 0.1$ eV. The band structure of compressively strained $\text{GaSb}_{1-x}\text{Bi}_x$ layers on GaSb with Bi concentrations between 2.3% and 10.4% has been measured by Batool et al. [63] using PR spectroscopy at RT. Their results show that the strained bandgap E_g equals to Δ_{SO} at a Bi concentration of $9.0\% \pm 0.2\%$. After decoupling the effect of strain, the Bi concentration is estimated as $10.5\% \pm 0.2\%$ to meet the condition of $E_g = \Delta_{SO}$ in free-standing $\text{GaSb}_{1-x}\text{Bi}_x$ layers.

Petropoulos et al. [62] applied the VBAC model to $\text{In}_y\text{Ga}_{1-y}\text{Bi}_x\text{As}_{1-x}$ and discovered that the interaction strength between the Bi resonant level and the VB of InGaAs not only depended on Bi content but also the In content as well. The VBAC model shows that $\text{In}_y\text{Ga}_{1-y}\text{Bi}_x\text{As}_{1-x}$ lattice-matched to InP is possible by varying x and y compositions, with a theoretical cutoff wavelength of $6 \mu\text{m}$. Energies of E_0 and $E_0 + \Delta_{SO}$ transitions in $\text{In}_{0.53}\text{Ga}_{0.47}\text{Bi}_x\text{As}_{1-x}$ alloys with $0 < x \leq 0.036$ have been studied by CER spectroscopy at RT [175]. The Bi related bandgap narrowing and the increase in SO splitting are equal. For $\text{In}_{0.53}\text{Ga}_{0.47}\text{Bi}_x\text{As}_{1-x}$ layers with $x > 3\%$, the SO splitting is very close to the energy gap. The VB nature of III-V semiconductors can be characterized primarily by the anion (V) species, while the CB can be explained primarily by the cation (III) species. The SO splitting, therefore,

changes very significantly with changes in anion species. The Bi related changes in the band structure are caused by a shift of heavy- and light-hole bands towards the CB, resulting in the reduction of bandgap and the increase of the SO splitting.

The band structures of $\text{InP}_{1-x}\text{Bi}_x$ alloys with $0 < x \leq 0.034$ are studied using CER spectroscopy and ab initio calculations [161]. The E_0 transition shifts to long wavelengths very significantly ($-83 \text{ meV}/\% \text{ Bi}$), while the $E_0 \pm \Delta_{\text{SO}}$ transition shifts very weakly ($-13 \text{ meV}/\% \text{ Bi}$) with increasing Bi concentration. These Bi-related changes in the band structure are in a good agreement with the VBAC and the ab initio calculations. Shifts of E_0 and $E_0 \pm \Delta_{\text{SO}}$ transitions studied by the ab-initio calculations are -106 and $-20 \text{ meV}/\% \text{ Bi}$, respectively. The incorporation of Bi atoms into an InP host affects both the CB and VB by $-27 \text{ meV}/\% \text{ Bi}$ and $79 \text{ meV}/\% \text{ Bi}$, respectively. By fitting the CER data with the bandgap function similar to Equation (8), the bowing parameter is determined as $8.5 \pm 0.5 \text{ eV}$.

6.2.2. Effective Mass

Bismuth incorporation into III–V alloys induces changes in effective mass. The value of electron and hole effective mass is very important for understanding electronic property of dilute bismides. Measuring electron and hole effective masses provides a potential to unveil physics of hybridization of the Bi-related state with VB and CB. Pettinari et al. [215] reported that the exciton mass of $\text{GaAs}_{0.981}\text{Bi}_{0.019}$ was derived as $0.088m_0$ from magnetic field dependent PL. They considered that both hole and electron effective masses increased and inferred that the localized potential of Bi atoms strongly affected both VB and CB. They also measured the Bi composition dependence of the exciton reduced mass, μ_{exc} , of $\text{GaAs}_{1-x}\text{Bi}_x$ in a very large Bi concentration range ($x = 0\%–10.6\%$) [216]. The magnetic field dependent PL shows an unusual compositional behavior. The value of μ_{exc} first increases rapidly by 50% for $0 \leq x \leq 1.5\%$, then fluctuates around $0.08m_0$ ($1.5\% < x < 6\%$), and decreases to below the GaAs value for $x > 8\%$. Such a dependence reveals existence of different concentration intervals, which means that continuum states of the VB and CB hybridize with the Bi-related levels to different extents. The Bi hybridization presents an impurity-like behavior for $x < 6\%$ and a band-like character for $x > 8\%$.

6.2.3. Impact of Alloy Disorder on the Band Structure

In the GaAsBi band structure, the large variation of atomic potential creates a localized level near the VBM of GaAs. Bismuth localized potential and the surrounding lattice relaxation disturb the GaAs electronic band structure. The Bi localized states attract holes from VB. Although the isolated Bi energy level is believed to reside below the VBM, there exists evidence that randomly formed few-atom clusters result in localized states. These localized states can trap excitons, preventing them from diffusing to non-radiative defects, which could explain the strong PL observed in these low-temperature grown bismide materials. Localized states are also consistent with the observed broad PL linewidth. Lu et al. [217] have measured RT PL spectra for $\text{GaAs}_{1-x}\text{Bi}_x$ alloys with x in the range of $0.2\%–10.6\%$. The PL peak energy increases with PL pump intensity. Besides, the PL intensity is found to increase with Bi concentration for small x_{Bi} , peaking at $x_{\text{Bi}} = 4.5\%$. The excitation intensity has a significant effect on the PL peak energy and linewidth. They attributed these phenomena to the shallow localized states induced by Bi clusters near the top of the VB. At low excitation intensity, only the localized states with the highest binding energies participate in PL. In this case, the PL peak energy is the smallest. With increasing excitation intensity, the recombination lifetime is reduced. In this case the holes have less time to thermalize down into the localized states before they recombine, so that the corresponding PL peak shifts higher in energy. The temperature dependent PL of $\text{GaAs}_{1-x}\text{Bi}_x$ alloys shows an S-shape behavior due to the localized states [218].

Usman et al. [69] have investigated alloy disorder effects on the electronic structure of GaAsBi by comparing atomistic TB results with RT PR measurements. The disorder effects have a significant influence for low Bi compositions (2.3% and 4.5%) even in large supercells. At high Bi compositions (8.5% and 10.4%), the effect of atomistic randomness is less marked at the VBM, because the E_{v1} energy is shifted well above the pair/cluster state energies. CER and PR measurements for GaAsBi alloys show broadening of E_0 and $E_0 + \Delta_{SO}$ transitions in contrast to that of GaAs [175,219]. The broadening mainly results from the alloy inhomogeneity and tail of density of states that appears due to point defects, Bi pairs and other atom complexes.

6.2.4. Transport Properties

Electron mobility of GaAsBi does not show significant degradation with Bi alloying [50,51,220,221], which is the opposite of the case of N incorporation in GaAs where the electron mobility is significantly degraded due to strong carrier scattering at the localized states formed by isolated N and N-clusters [222,223]. Bismuth incorporation causes degradation of hole mobility in GaAs. This can be explained that the isolated Bi and pairs (clusters) generate potential trap states for holes, leading to a decrease in hole mobility by scattering at these states.

Pettinari et al. [220,224] studied transport properties of $\text{GaAs}_{1-x}\text{Bi}_x$ films. The undoped GaAsBi epilayers demonstrates p -type conductivity in a wide range of Bi-concentrations ($0.6\% \leq x \leq 10.6\%$). The increase of conductivity with increasing x is paralleled by an increase in the density of free holes by more than three orders of magnitude. The p -type conductivity results from holes thermally excited from Bi-induced acceptor levels lying at 26.8 meV above the VBM of $\text{GaAs}_{1-x}\text{Bi}_x$ with a concentration up to $2.4 \times 10^{17} \text{ cm}^{-3}$ at $x = 10.6\%$. The free hole concentration increases with Bi concentration, while the free hole mobility decreases due to the hybridization of the Bi-induced localized states. Kini et al. [221] also studied the effect of Bi incorporation on hole mobility in $\text{GaAs}_{1-x}\text{Bi}_x$ using Hall and PL techniques. Different from the results of Pettinari et al., they found that the hole concentration decreases with Bi concentration. They considered that Bi_{Ga} antisite defects compensate the background acceptors, leading to the reduction of the effective hole concentration.

For $\text{In}_y\text{Ga}_{1-y}\text{Bi}_x\text{As}_{1-x}$ films grown on InP:Fe substrate, the electrical conductivity is n -type [62]. When the Bi concentration increases from 1.1% to 3.6%, electron concentration increases from 1 to $6 \times 10^{16} \text{ cm}^{-3}$ and electron mobility decreases from 7400 to $350 \text{ cm}^2/\text{Vs}$.

6.2.5. Impurity States

Since dilute bismides are metastable alloys and low temperature growth ($<400^\circ\text{C}$) is essential for realizing Bi incorporation in the epilayer, it may cause defects in epilayers. Deep-level transient spectroscopy (DLTS) is a powerful tool to investigate deep levels. The majority-carrier deep levels induced by Bi incorporation are at 0.43 and 0.23 eV above the VBM for p -type $\text{GaAs}_{1-x}\text{Bi}_x$ grown at 370°C with $x = 1.2\%$ and $x = 3.4\%$, respectively [8]. The deep-level trap concentration is on the order of 10^{15} cm^{-3} . Bismuth atoms facilitate migration of constituent atoms and prevent them from forming point defects. The possible origin of the hole traps is related to As antisite, As_{Ga} , Bi antisite, Bi_{Ga} , and relevant clusters of point defects.

Deep-level transient spectroscopy has been applied to study electron and hole traps in InPBi alloys with $x = 2.2\%$ and 2.4% [225]. One donor-like trap with an activation energy of 0.45–0.47 eV below the CB and one acceptor-like trap with an activation energy of 0.08 eV above the VBM have been identified. The acceptor trap is due to incorporation of Bi into the InP host. The donor trap is related to the isolated P_{In} defect, which is typical for low temperature grown InP. The acceptor trap contributes to the partial compensation of native free electron density in InPBi layers.

6.3. Optical Properties

In the past decade, dilute bismides have been studied by several spectroscopy methods. In this Section we primarily review the optical properties that respond to the electronic band structure change induced by Bi effects. First we give a brief introduction for the frequently-used spectroscopy methods in dilute bismides, to nail down the prominent features of each spectroscopy and what electronic and optical properties they reveal.

Absorption as a conventional pathway indicates the effective optical bandgap of semiconductors. The theoretical absorption coefficient $\alpha(E)$ around the optical bandgap (E_g) is proportional to $(E - E_g)^{1/2}$ where E is photon energy for the direct gap interband transition under effective mass approximation [226]. Experimentally, the absorption edge is influenced by the shallow defect levels and phonon scattering. Photoluminescence is another important spectroscopy that plays a crucial role in optical characterization. The laser pumping produces electrons in CB and holes in VB. Those electrons and holes relax and distribute around CB bottom and VBM, respectively, and then recombine radiatively [227]. PL is sensitive to the band edge electronic transition and the shallow impurities and/or defect levels. For some narrow gap dilute bismides like InAsBi and InSbBi, the available PL is located in mid-IR region, which is overwhelmed by the strong environment black-body emission. Modulation PL technique based on the step-scan Fourier transform infrared (FTIR) spectrometer is therefore employed [228,229]. In addition, photoreflectance (PR) spectroscopy is a distinctive method for optical properties and electronic structure of dilute bismides. The photo-induced carriers modulate the built-in electric field and/or carrier density, which emphasize the weak transitions between critical points and eliminate the unwanted static background [58]. PR is sensitive to both the band edge structure and the above-bandgap transitions [230–232]. The optical transition characterization for the excited state is hence available. The FTIR-based PR technique covers a wide wavelength range from 0.5 to 20 μm [233,234], which is serviceable for most III-V-Bi alloys.

6.3.1. Optical Bandgap

Since Bi incorporation mainly raises the VBM and narrows the bandgap in dilute bismides, determining the shrinkage extent of bandgap is of significant for designing the cut-off wavelength of devices. Early work on the optical bandgap of $\text{InSb}_{1-x}\text{Bi}_x$ epitaxial film grown by multitarget sputtering system was studied by absorption at 20 K, which deduced a linear bandgap narrowing rate as about 17 meV/% Bi and suggested the semiconductor-semimetal transition of $\text{InSb}_{0.89}\text{Bi}_{0.11}$ [20]. Later, Ma et al. performed the 10 K PL on InAsBi and As-rich InAsSbBi grown by MOCVD, to determine the bandgap narrowing rate as 55 meV/% and 46 meV/%, respectively [25]. However, recent reports for the MBE grown InSbBi and InAsBi showed very different bandgap narrowing rate. Svensson et al. obtained a narrowing rate of 38 meV/% for InAsBi by 77 K PL method [164] whereas the RT absorption by Rajpalke et al. gave a narrowing rate of about 35 meV/% for InSbBi [180], about twice as that in Reference [20]. In a report of Feng et al. [150], they investigated the thermal annealing influence on optical band edge for GaNAsBi. The results show that the PL energy shifts in a scale of tens meV with various annealing temperatures. They suggested that the PL energy shift is attributed to modification of the band tail induced by the micro-scale changes in bismides. This finding gives a hint that the effective optical bandgap of dilute bismides is remarkably affected by the distribution of band tail states. The determination of bandgap narrowing rate for dilute bismides hence disperses to a certain extent. We summarize the experimental bandgap narrowing rate for several III-V-Bi ternaries probed by different optical methods, as shown in Figure 18.

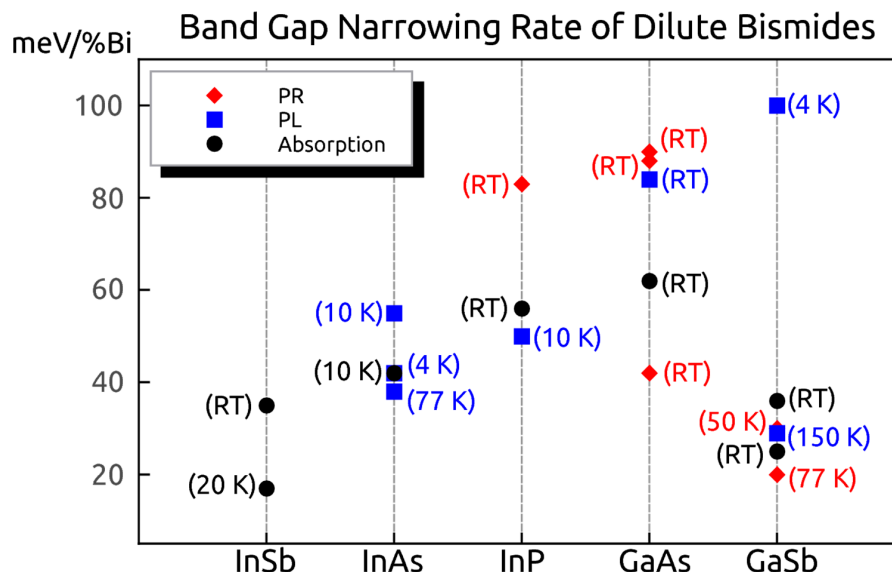


Figure 18. Summary of bandgap narrowing rate for several III-V-Bi ternaries probed by different optical spectroscopy methods. The III-V matrixes of bismides are illustrated in the bottom. The relevant references are Ref. [20,21,25,29,44,74,149,161,165,168,185,188,190,205,212,235–237].

By performing temperature-dependent PL [164], Oe and Okamoto reported that the thermally induced bandgap redshift in GaAsBi is much less sensitive than that in GaAs [32]. Yoshida et al. obtained the same results with PR measurements later [48]. In their view, GaAsBi consists of GaAs semiconductor and GaBi semimetal components and the latter's bandgap manifests the positive temperature coefficient, which leads to the temperature-insensitive bandgap of GaAsBi. But Francoeur's PL work at about the same time did not sustain that conclusion [192]. The temperature-dependent PR measurements by Kudrawiec et al. about one decade later showed that the temperature-bandgap coefficient is independent on Bi content in InGaAsBi and GaSbBi [190,238]. The authors argued that the PL in Reference [32] was influenced by carrier localization and the PR in Reference [48] was interfered by Franz-Keldysh oscillation. However, the recent high excitation PL work with the localization elimination by Pettinari et al. re-supported the Bi-induced bandgap insensitivity against temperature [239]. In the above studies, different groups obtain various results for the bandgap-temperature sensitivity of dilute bismides, although the band tail effect has been considered. This issue is under debate and more investigations are required.

6.3.2. Spectral Broadening in Dilute Bismides

In some reports on the spectral investigation of dilute bismides [180,217,239,240], the spectral lineshape broadens as Bi content increases at the low-content region, for either absorption, PL or PR measurements. The inhomogeneous distribution of Bi atoms [241] and the Bi pairs/clusters-related acceptor levels near the VBM [67,221] are the dominant reasons for the spectral broadening in thin-film bismides. In addition, the Bi-induced interface change plays another important role in spectral broadening in the quantum structure. Chen et al. studied PL of GaSb/AlGaSb and GaSbBi/AlGaSb single QW grown at different temperatures, down to a low temperature of 3.8 K and up to a high magnetic field of 10 T [174]. They found that the PL with a broad linewidth of GaSbBi QW essentially consists of multiple detailed PL features. The discrimination of the detailed PL features is reinforced at high magnetic field because of the shrinkage of the exciton radius (see in Figure 19). Among those detailed PL features, one of them is located at a higher energy than the effective bandgap of GaSb QW. By comparing the reduced effective mass and exciton radius of each PL process, they clarified that the interface of GaSbBi/AlGaSb QW is a terrace-like structure, due to the Bi-induced interfacial Al/Ga inter-diffusion.

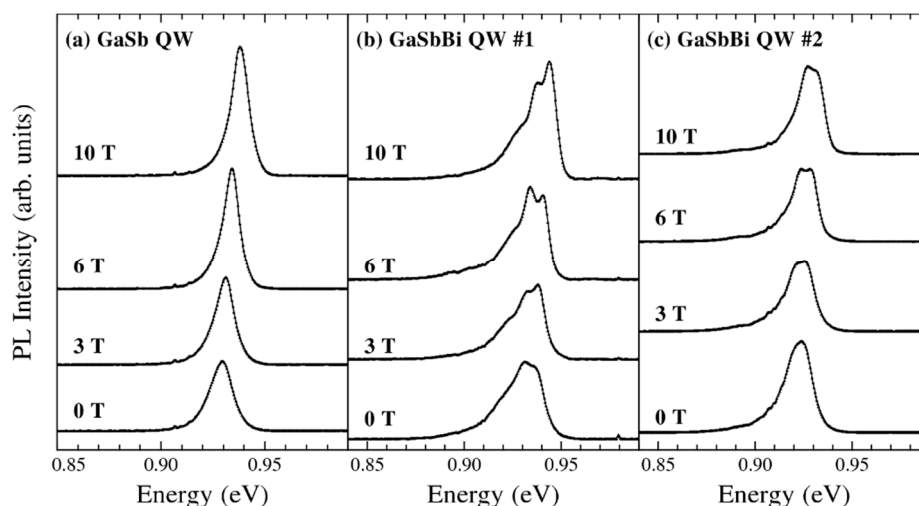


Figure 19. PL spectra of GaSb quantum well (QW) and GaSbBi QW in various magnetic fields. The detailed PL features in GaSbBi QW are present. A detailed PL feature being located at a higher energy than the effective bandgap of GaSb QW is shown in GaSbBi QW #2.

Interestingly, Beaton et al. [242] found that PL was not inherently broad in GaAsBi. Using a partial Bi wetting layer, they achieved a measured spectral linewidth as low as 14 and 22 meV under dark and illuminated condition at 6 K, respectively from GaAsBi with a Bi content less than 0.6%, less than a quarter of the best value (~60 meV) reported previously [135,215,243]. Under this circumstance, the Bi surfactant layer provides the required amount of Bi for incorporation without excess Bi on the surface risking for droplet appearance. This improvement of optical behavior encourages GaAsBi for practical utility in optoelectronic devices.

6.3.3. Photoluminescence Intensity

As PL intensity reflects the radiative recombination capability, it is a key property for revealing the carriers' optical activity in optoelectronic materials. Several works have utilized the surfactant effect of Bi to reduce defects and to enhance PL intensity [112,113,244]. In dilute bismides, the Bi induced PL intensity change is a hot topic at present. Oe's work showed that the RT PL intensity reduces as Bi content increases in $\text{GaAs}_{1-x}\text{Bi}_x$ ($x < 0.026$) [245], which implied that the Bi incorporation increases the non-radiative recombination centers. But Lu's work gave a different non-monotonous phenomenon: the RT PL intensity enhances more than two orders of magnitude with Bi content up to about 4.5% and significantly drops down for high Bi contents [217]. They suggested that the PL enhancement is attributed to the Bi induced localized electronic states near the VBM to promote formation of bound holes. The influences of the bound holes surpass the PL degradation due to the non-radiative centers. Later, Mohmad et al. reported a similar non-monotonous result at 10 K and confirmed the low-temperature PL originating from localization [243]. Their PL intensity at RT showed saturation rather than significant degradation. They attributed the saturation to the large GaAsBi/GaAs VB offset to avoid holes thermally escaping into GaAs substrate from the GaAsBi film.

Imhof et al. reported that the PL intensity quenching of GaAsBi is controlled by a two-scale band-tail accounting for cluster localization and alloy disorder effects [246]. Later, Shakfa et al. further suggested that the two components with exponential- and/or Gaussian-type density of localized states (DOLSs) are independent [247]. Their results showed that the position of the second component DOLS shifts to the band edge meanwhile the width of the first component reduces as Bi content increases. The authors guessed that the change of DOLS in GaAsBi may be due to the interactions between neighboring localized centers, the lattice distortion and the formation of impurity band. Hence the PL intensity of dilute bismides at a finite temperature is significantly dependent on the

distribution of the DOLS, and improving the DOLS should be an effective routine to improve the PL efficiency. Unfortunately, the Bi-related localized defects in GaAsBi are hardly reduced by annealing method [150]. Although Moussa et al. reported that the PL intensity of GaAsBi enhances about one order of magnitude with an annealing temperature of about 700 °C [148], they suggested that the PL intensity improvement is dominated by the reduction of non-Bi-related defects [145]. Nevertheless, GaAsBi laser diodes [248,249] and LEDs [250] have been realized, suggesting the promising application of dilute bismides on optoelectronic devices.

7. Impact of Bismuth on Nanostructures

Bismuth can have an impact on semiconductor nanostructures in two different ways: as a constituent and as a surfactant. So far there have only been a few studies about Bi's influence on InAs quantum dots (QDs) as summarized in Table 7 [112,114,251–253] while Bi incorporation in nanowires (NWs) has just been reported recently [254]. Owing to δ -like density of states and excellent carrier confinement in QDs, InAs QD lasers possess a number of favorable device performance such as low threshold current density, high temperature stability and large differential gain, making them attractive for high-speed telecom laser applications. For self-assembled InAs QDs grown on GaAs substrates via Stranski-Krastanov (S-K) growth mode, although light emission above 1.6 μm at RT has been demonstrated [255], the longest lasing wavelength is still limited to 1.5 μm [256]. One intrinsic problem for limiting the wavelength extension of the emitted light from InAs QDs is the selection of barrier material surrounding the InAs QDs. InGaAs is commonly used to extend emission wavelength, but the bandgap reduction with In content is not effective, i.e., around 15 meV/%In. In addition, the band offset of InGaAs/InAs mainly lies in the CB, making holes easily leaking out of the valence QW. Adding Bi in InGaAs can effectively lower the barrier and extend emission wavelength. Moreover, the VB offset of InAs/(In)GaAsBi is less affected than that of InAs/InGaAs, making efficient trapping of holes in InAs QDs. Bismuth incorporation in InAs QDs has a similar effect to extend emission wavelength.

Bismuth is a well-known surfactant for III-V materials at a normal growth temperature. Since Bi is isoelectronic with As, even a considerable amount of Bi incorporation into InAs will not cause any change in background carrier density theoretically. In this Section, we will first present results on influence of Bi as surfactant on InAs QD morphology and optical property. Then some examples of Bi alloyed III-V nanostructures will be presented.

Table 7. Summary of reports about Bi influence on quantum dots (QDs).

Ref.	Epitaxy Method	Growth Condition	Bi Influence	PL
[251]	MOCVD	5 ML InAs @ 510–530 °C, Bi = 0.01–0.1 ML	Surfactant effect $L_D \downarrow$	0.93 eV @ 77 K 1.46 μm @ 300 K
[114]	MOCVD	InAs/InGaAs DWELL @400 °C calibrated T_g	Surfactant effect $L_D \uparrow$	I_{PL} & λ improved
[112]	MBE	2.5 ML@480 °C Bi = 8×10^{-8} Torr	Surfactant effect $L_D \uparrow$	I_{PL} improved
[252]	MBE	2.2 ML@400 °C Bi = 0.015–0.06 ML/s	Surfactant effect, Incorporation effect	I_{PL} & λ improved
[253]	MBE	2.3–3.3 ML@500 °C Bi = 5×10^{-8} Torr	Surfactant effect $L_D \downarrow$	I_{PL} , FWHM & λ improved

7.1. Bismuth Surfactant Effect on InAs QDs

Quantum dot coalescence is one of the most serious problems during epitaxial growth of large size coherent InAs QDs for long wavelength light emission. It results in inhomogeneous QD size, density decreasing and dislocated QDs, which deteriorate morphology and optical properties. Inspired by previous works using As as a surfactant in the growth of Ge/Si heterostructures [257], Bi in

SnGe/Ge [258], researchers turn their focus on the Bi surfactant effect to solve the coalescence problem during the InAs QDs growth. Surfactant effect means initiation of InAs QDs is delayed. However, it is unclear whether surface diffusion of adatoms will be enhanced or not.

In 2000, Zvonkov et al. [251] firstly reported the Bi surfactant effect on InAs QDs grown on GaAs by MOCVD. With Bi supplying during growth, QDs distribute homogeneously with a lateral size and a height much smaller than that of QDs grown without Bi. Large dislocated QDs are also avoided. PL spectrum shows a narrower FWHM compared with QDs grown without Bi. They attributed the improved QDs' morphology and PL to that massive Bi atoms would reduce surface mobility of In atoms, therefore suppressing coalescence of large dislocated InAs QDs. In addition, they obtained the longest emission wavelength of 1.33 μm at 77 K, and claimed the RT emission wavelength of 1.46 μm but the PL spectrum is not found in their paper.

The second report came by Okamoto et al. [114] 10 years later also using MOCVD. This time they designed a dot-in-well structure, i.e., InAs QDs embedded in an InGaAs QW, introducing Bi during both the QDs and QW growth. An enhanced PL intensity and peak wavelength are achieved due to the higher QDs' height compared with those grown without Bi. SIMIS measurement reveals no evidence of Bi incorporation. They therefore contributed the increased QD height to that Bi surfactant effect increases In adatoms surface diffusion length. Fan et al. [112] hold the same view that In adatoms diffusion length is enhanced by Bi surfactant effect.

Dasika et al. [253] reconciled the above discrepancy about In adatoms surface diffusion. A set of QDs are grown with InAs thickness varying from 2.3–3.3 ML. AFM results reveal that for InAs deposition thickness <2.6 ML, QDs grown with Bi have a smaller density than samples without Bi. Further increasing the deposition thickness >2.6 ML, the QD density with Bi exceeds those grown without Bi. This QD density varying phenomenon can be interpreted as follows. Typically, InAs QDs are grown in an S-K mode, and InAs initially forms a two-dimensional wetting layer (WL) on the growing surface. The accumulated strain in the WL increases with its thickness. At a critical thickness, QDs are formed and the overall strain is relieved. When Bi is brought to QD growth, Bi atoms act as a surfactant to reduce In surface mobility and lower the surface energy. In this case, the InAs critical thickness is enhanced and formation of QDs will be delayed. The QD density is lower than the density of Bi-free QDs for an InAs deposition thickness below 2.6 ML. Further increasing InAs deposition results in an eventually formation of QDs. The increase of QD density is due to the increasing availability of additional In atoms as well as the suppressed In surface diffusion by presence of Bi. This provides growers a clue to achieve large QDs size and uniformity without decreasing a QD density.

Because of the even worse solubility of Bi in InAs than in GaAs, growth of InAsBi nanostructure is more challenging. In this sense, Bi-mediated InAs QD growth focusing on Bi incorporation in QDs is seldom explored. Discovery of PL modification from Bi clusters in GaAsBi [132,259] has inspired scientists to relate the PL changes in InAs QDs with Bi incorporation effect. Reyes et al. [252] reported that PL enhancement of InAs QDs is not only related to the Bi surfactant effect but also to the Bi incorporation. 2.2 ML InAs(Bi) was grown on GaAs with/without a Bi flux at a low growth rate of 0.06 ML/s at 400 °C and capped by 50 nm thick GaAs. PL from the InAs(Bi) QDs shows 68 times higher intensity at peak wavelength of 1227 nm compared with that from Bi-free InAs QDs at 1055 nm. Z-contrast TEM investigation shows that Bi atoms distribute mainly in the core of InAs QDs, exhibiting Bi cluster formation.

7.2. Bismuth Catalyzed Growth of GaAsBi Nanowires

Recently, Bi was reported by Ishikawa's group to be a catalyst for growth of GaAsBi NWs using MOCVD [254]. The authors initially deposited Bi nano-islands on GaAs substrate at 420 °C and then reduced temperature to 385 or 400 °C for growth of GaAsBi NWs. The GaAsBi NWs exhibit columnar structures with Bi particles on top of the NWs. Both substrate temperature and flow rate of TMBi are deemed as two vital parameters that can vary GaAsBi NWs differently. Doubling the flow rate of

TMBi results in a decrease in NW density and change in geometrical shape. With an optimized growth condition of 400 °C and TMBi flow rate of 2.5 ML/s, they obtained a uniform straight NW distribution with length and diameter at about 1 µm and 150 nm, respectively. Other growth conditions cause the “V” shape NWs with a short length. SEM investigation of Bi droplets deposited on GaAs substrate reveals dissolution of GaAs in Bi droplets. Bismuth nano-particles are regarded as the nucleation point for the GaAsBi NWs, i.e., Bi catalyzes the growth of GaAsBi NWs.

8. Device Application

8.1. Telecom and MIR Lasers

Current 1.3 and 1.55 µm InGaAsP QW telecom lasers based on InP reveal drawbacks that their threshold current and internal optical loss tend to increase strongly with increasing ambient temperature, especially above RT, due largely to a combination of two intrinsic loss mechanisms: Auger recombination involving CHSH and IVBA [260]. These commercial lasers need to be operated using a thermoelectric cooler for many applications, significantly increasing the overall energy budget associated with their operation.

In 2012, Sweeney and Jin presented systematical calculations on band parameters of GaAsBiN on GaAs, such as bandgap, SO splitting energy, band offsets and strain [53]. It is shown that the quaternary alloy covers a wide energy range from 0.2 eV to 1.4 eV for Bi up to 12% and N up to 6%, while it is nearly lattice matched to GaAs. The Bi containing alloys offer a large Δ_{SO} (2.2 eV for GaBi) and incorporation of Bi has the potential of achieving $\Delta_{SO} \geq E_g$. In this case, the non-radiative Auger recombination of CHSH type and IVBA are suppressed, and characteristic temperature of laser diodes is expected to be enhanced. This is of significant importance for designing Auger and leakage free long-wavelength lasers. For GaAsBiN/GaAs with Bi up to 12% and N up to 6%, which is within acceptable strain for making photonic devices, the optimum band structure with $\Delta_{SO} \geq E_g$ is achievable for the energy range of ~450–850 meV (~1.5–2.7 µm). They determined that GaAs-BiN alloys have the potential to cover a wide spectral range from near- to mid-IR with a flexible control of the band offsets and SO splitting.

Lewis et al. reported the first GaAsBi LEDs with $x_{Bi} = 1.8\%$ emitting at 987 nm [250]. From electroluminescence (EL) measurements at different temperatures, it is obtained that the peak wavelength is independent of temperature in the range of 100–300 K while the GaAs peak varies. The temperature insensitivity of the GaAsBi EL peak is explained by two competing processes: the bandgap change and the emission from lower energy states. GaAs_{1-x}Bi_x/GaAs LEDs were also demonstrated by Sweeney et al. [261]. The device consists of a 50 nm GaAs_{0.986}Bi_{0.014} active layer between two 25 nm GaAs spacer layers, further sandwiched between a 1000 nm *p*-doped and a 1000 nm *n*-doped GaAs waveguide layers. The emission wavelength is measured to be ~936 nm at 260 K. The temperature dependence of the emission wavelength is measured to be 0.19 ± 0.01 nm/K in 80–260 K. The emission efficiency decreases rapidly with increasing temperature, implying that some non-radiative loss mechanism is significant.

In 2010, a photo-pumped GaAsBi/GaAs Fabry-Perot (FP) laser was realized for the first time by Yoshimoto et al. [262]. A GaAs_{0.975}Bi_{0.025} active layer is grown at 350 °C by MBE. At RT, a narrow lasing spectrum of 982.8 nm is demonstrated with a pumping density above 2.5 mJ/cm². The characteristic temperature of the laser is 83 K between 160 and 240 K. The lasing energy decreases at a constant rate of ~0.18 meV/K, which is only 40% of the temperature coefficient of the GaAs bandgap in the same temperature range. The lasing wavelength of photo-pumped GaAsBi lasers was later extended to 1204 nm at RT by the same research team in 2013 [263]. The characteristic temperature between 20 and 80 °C is $T_0 \sim 100$ K, slightly larger than $T_0 \sim 66$ K of the reported 1.3 µm InGaAsP FP lasers.

The first electrically pumped GaAsBi QW lasers were demonstrated by Luderwig et al. in 2013 [54]. The active region consists of a 6.4 nm thick GaAsBi ($x_{Bi} = 2.2\%$) QW between two 150 nm thick AlGaAs barriers for electrical confinement and further sandwiched between a 1400 nm

p-doped and a 1400 nm *n*-doped AlGaAs waveguide layers. Electrically pumped lasing at RT is demonstrated under pulsed excitation with a threshold current density of 1.56 kA/cm² for a 1 mm long cavity at an emission wavelength of 947 nm. Later in 2014, Yoshimoto et al. reported lasing oscillation up to 1045 nm at RT from electrically pumped GaAs_{1-x}Bi_x FP lasers ($x_{Bi} \leq 4\%$) [264]. For GaAs_{0.97}Bi_{0.03} QW lasers, the characteristic temperature in the temperature range of 15–40 °C is 125 K, higher than that in a typical 1.3 μm InGaAsP FP laser. Electrically pumped GaAsBi/GaAs laser is also presented by Sweeney et al. [265] grown by MOCVD. For GaAs_{0.956}Bi_{0.044} FP lasers, lasing at 1038 nm is demonstrated at 180 K. In 2015, Mawst et al. reported GaAsBi QW lasers with GaAsP as strain compensated barriers grown by MOCVD [266]. The DFT calculations show that GaAsP is an effective barrier material for electron confinement in GaAsBi QWs with comparable band offset to that employing Al_xGa_{1-x}As ($x < 0.2$) barriers. Ridge waveguide lasers are fabricated and broad EL emission at around 923 nm at 60 K is observed from the GaAs_{0.97}Bi_{0.03} active region. However, lasing is not observed up to the maximum current injection of 4 kA·cm⁻².

In_{0.53}Ga_{0.47}As lattice-matched to InP possesses a direct bandgap of 0.74 eV (1.68 μm). Adding a small amount of Bi can push emission wavelength beyond 2 μm, thus entering mid-IR range. In 2011, Zide et al. presented studies on the optical and electrical properties of InGaAsBi (lattice-matched to InP) grown by MBE using solid sources of In, Ga and Bi, and a valved As cracker [62]. From optical transmission measurements, they estimated a bandgap reduction rate of about 56.1 meV/% Bi. The lowest bandgap energy of 0.496 eV is measured for $x_{Bi} = 3.18\%$, corresponding to a peak wavelength of about 2.5 μm and a strain value of about 0.75% with respect to InP substrate. The VBAC model is applied to simulate InGaAsBi lattice-matched to InP with varied In and Bi concentrations and a theoretical cutoff wavelength of 6 μm is obtained.

Sweeney et al. also systemically investigated band parameters and strain of InGaAsBi on InP based on recent experimental data [61,267]. Based on the VBAC model including strain effect, they calculated bandgap and SO splitting energy of InGaAsBi and found a cross-over similar to the case of GaAsBi. Such a cross-over, i.e., $\Delta_{SO} \geq E_g$, is estimated to occur for a Bi content between 2.5%–6%, smaller than about 10% for GaAsBi. The strain of InGaAsBi is also calculated and can be designed with zero or a small strain depending on In and Bi concentrations. Furthermore, they studied optical properties of In_{0.53}Ga_{0.47}Bi_xAs_{1-x}/InP samples for $x \leq 3.2\%$ [64,178]. The PR results resolve clear E_g and $E_g + \Delta_{SO}$ features, with $E_g \approx \Delta_{SO}$ near $x = 3.2\%$ at RT.

8.2. Photodetectors

One practical application for exploring dilute bismides in early days is to extend absorption wavelength of III-Vs to the long wavelength mid-IR (LW-MIR) regime (8–12 μm). In 1998, Razeghi et al. [30] successfully demonstrated RT operation of 8–12 μm InSbBi LW-MIR photodetectors. The InSbBi/InSb heterostructures are grown on GaAs by low pressure MOCVD. The responsivity at 10.6 μm is about 1.9 mV/W at RT and the corresponding Johnson noise limited detectivity is about 1.2×10^6 cmHz^{1/2}/W. The carrier lifetime is estimated to be about 0.7 ns from the bias voltage dependent responsivity measurements.

In 2014, Sandall et al. reported InAsBi photodetectors [267] aiming at further extending detection wavelength beyond InAs which has been demonstrated to operate as an excellent avalanche photodiode with single carrier multiplication and low excess noise. The sample is grown on an *n*+ InAs substrate at 500 °C using an Omicron MBE system. The photodiode active region is 1000 nm thick and consists of ten periods of 90 nm InAs_{0.98}Bi_{0.02} QWs. Absorption spectrum of InAsBi photodiode with the longest cutoff wavelength of 3.95 μm is obtained at 225 K, compared with a cutoff wavelength of 3.41 μm from the reference InAs photodiode at the same temperature. Temperature dependence of the bandgap is found to be 0.19 meV/K, smaller than that of InAs. In 2016, Gu et al. [268] reported an InGaAsBi detector, in which the whole structure is nearly lattice-matched to InP substrate. The Bi content is about 3.2% in the absorption layer and the cut-off wavelength is extended to 2.1 μm at RT, corresponding to

a Bi-induced bandgap reduction of about 180 meV. The dark current is found to be lower than that in InGaAs detectors with a similar cut-off wavelength.

Low-temperature grown (LTG) GaAsBi can possess properties such as a very large resistivity and an ultra-short carrier lifetime, which make it as a prospective material for near-IR laser activated terahertz (THz) radiation emitters and detectors [269]. In 2012, a research group from Lithuania reported application of using GaAsBi for radiation detection in THz frequency. Photoexcited carrier relaxation in LTG GaBiAs layers is studied by optical pump–THz probe technique and the electron lifetime is estimated to be 1 ps in the GaAsBi layer grown at 280 °C. The LTG GaAsBi layer with the short carrier lifetime is used for manufacturing photo-conductive antennas and for generating THz pulses. The THz transient and its Fourier spectrum are measured when the emitter is biased at 10 V. Spectrum of the transient reaches frequencies larger than 3 THz, while its amplitude is comparable to that of THz transients obtained from LTG GaAs components under the same bias voltage. In 2015, the same group reported another photo-conductive THz detector fabricated by GaInAsBi on GaAs substrate [270]. Bismuth composition of GaInAs_{1-x}Bi_x is characterized by XRD and EDX and reach unexpectedly high of about 10%. Compared with their previous GaAsBi photo-conductive THz detector, this one can be activated by a wide range of optical wavelength including 1.55 μm with a comparable detection sensitivity. In addition, this quaternary GaInAsBi detector exhibits good signal-to-noise ratio (SNR) of ~50 dB with the THz pulse spectrum extended to 3.5 THz.

8.3. Other Devices

Beside applications in near-IR and mid-IR lasers and photodetectors, dilute bismides have also been reported in solar cell and thermoelectric applications. Because GaAs_{0.94}Bi_{0.06} yields a direct bandgap at 1 eV with only 0.7% strain when grown on GaAs, it has been considered to be a promising candidate material for 1 eV sub-cells in multi-junction solar cells [271]. As GaAsBi has relatively high absorption coefficient, it could generate sufficient current to match the sub-cell photocurrent from the other sub-cells of a standard multi-junction solar cell.

As Bi being a heavy atom, the thermal conductivity is expected to be small. This implies that InGaAsBi can be as a promising material for thermoelectric application, argued by Zide et al. [272]. The InGaAsBi samples are grown with different Bi concentrations on (001) InP:Fe substrates using the OSEMI NextGen MBE system. The Seebeck coefficient and thermoelectric power factor (TPF) varied with carrier concentration are studied. At 1.6% Bi, there is an improvement in Seebeck coefficient and TPF, relative to Si:InGaAs, especially at low to moderate carrier concentrations of *n*-InGaAsBi. For example, at a carrier concentration of $\sim 1.4 \times 10^{18} \text{ cm}^{-3}$, a 49.6% improvement in TPF is obtained from Si:InGaAs ($1.37 \times 10^{-3} \text{ Wm}^{-1}\cdot\text{K}^{-1}$) to Si:InGaAsBi ($2.05 \times 10^{-3} \text{ Wm}^{-1}\cdot\text{K}^{-1}$). The improvement results from a large Seebeck coefficient, which is coupled to a complex CB profile in these materials. A peak *ZT*-value of 0.23 is achieved for InGaAsBi (1.6% Bi), which is significant for III-V materials.

9. Summary

The ever-increasing interest in exploring dilute bismide has resulted in this material being closely integrated to classical III-V compound semiconductors as a new family member. The unique physical properties including a large energy bowing effect, large SO split energy, temperature insensitive bandgap, negligible influence on electron and hole mobility for small Bi incorporation and surfactant effect open the possibility for various device applications. High quality bismide thin films and nanostructures have been successfully grown by MBE and MOCVD. The Bi composition is well above the doping level and in many alloys far beyond the solubility limit predicted by thermodynamics, and strictly speaking, bismide is no longer dilute rather in a form of alloy. The weak III-Bi bonding nature indicates a metastable phase for bismide alloys. Results from thermal annealing reveal stable Ga-Bi bonding up to at least 700 °C and In-Bi bonding to 600 °C, suitable for epitaxial growth of most optoelectronic devices. Near IR LEDs and laser diodes have been demonstrated showing good characteristic temperature and temperature insensitive lasing wavelength. However, the lasing

wavelength at RT is still limited to about 1.1 μm . A very exciting breakthrough would be pushing the lasing wavelength beyond 1.3 μm to the telecom regime. Dilute InGaAsBi and InAsSbBi are also promising material candidates for mid-IR photodetectors compared with traditional HgCdTe. The large SO splitting in bismide points future directions toward potential spintronic device applications. We expect this novel bismide will attract more and more academic attentions for both fundamental material and physics research as well as practical device applications.

Conflicts of Interest: The authors declare no conflict of interest.

References

1. Bismuth. Available online: <https://en.wikipedia.org/wiki/Bismuth> (accessed on 16 February 2017).
2. Rao, M.L.N.; Shimada, S.; Yamazaki, O.; Tanaka, M. Cross-coupling reaction of organobismuth dialkoxides with aryl bromides and iodides catalyzed by $\text{Pd}(\text{PPh}_3)_4$. *J. Organomet. Chem.* **2002**, *659*, 117–120. [CrossRef]
3. Krabbe, S.W.; Angeles, V.V.; Mohan, R.S. Bismuth (III) bromide in organic synthesis. A catalytic method for the allylation of tetrahydrofuran and tetrahydropyran ethers. *Tetrahedron Lett.* **2010**, *51*, 5643–5645. [CrossRef]
4. Rohr, O. Bismuth—The new ecologically green metal for modern lubricating engineering. *Ind. Lubr. Tribol.* **2002**, *54*, 153–164. [CrossRef]
5. Binnie, W.P. The structural crystallography of indium bismuthide. *Acta Crystallogr.* **1956**, *9*, 686–687. [CrossRef]
6. Hashimoto, K. Electrical properties of SnTe, SnSe and InBi at low temperatures. *J. Phys. Soc. Jpn.* **1957**, *12*, 1423. [CrossRef]
7. Dietz, R.E.; Thomas, D.G.; Hopfield, J.J. “Mirror” absorption and fluorescence in ZnTe. *Phys. Rev. Lett.* **1962**, *8*, 391–393. [CrossRef]
8. Thomas, D.G.; Hopfield, J.J.; Frosch, C.J. Isoelectronic traps due to nitrogen in gallium phosphide. *Phys. Rev. Lett.* **1965**, *15*, 857–860. [CrossRef]
9. Trumbore, F.A. Luminescence due to the isoelectronic substitution of bismuth for phosphorus in gallium phosphide. *Appl. Phys. Lett.* **1966**, *9*, 4–6. [CrossRef]
10. Dean, P.J.; White, A.M.; Williams, E.W.; Astles, M.G. The isoelectronic trap bismuth in indium phosphide. *Solid State Commun.* **1971**, *9*, 1555–1558. [CrossRef]
11. Armand, V.D. IEEE annals of the history of computing. *IEEE Comput. Soc.* **2010**, *32*, 72–79.
12. Avery, D.G.; Goodwin, D.W.; Lawson, W.D.; Moss, T.S. Optical and photo-electrical properties of indium antimonide. *Proc. Phys. Soc.* **1954**, *67*, 761. [CrossRef]
13. Lawson, W.D.; Nielsen, S.; Putley, E.H.; Young, A.S. Preparation and properties of HgTe and mixed crystals of HgTe–CdTe. *J. Phys. Chem. Solids* **1959**, *9*, 325–329. [CrossRef]
14. Jean-Louis, A.M.; Hamon, C. Propriétés des alliages $\text{InSb}_{1-x}\text{Bi}_x$ I. mesures électriques. *Phys. Status Solidi (b)* **1969**, *34*, 329–340. [CrossRef]
15. Jean-Louis, A.M.; Ayrault, B.; Vargas, J. Propriétés des alliages $\text{InSb}_{1-x}\text{Bi}_x$. II. absorption optique. *Phys. Status Solidi (b)* **1969**, *34*, 341–350. [CrossRef]
16. Joukoff, B.; Jean-Louis, A.M. Growth of $\text{InSb}_{1-x}\text{Bi}_x$ single-crystals by Czochralski method. *J. Cryst. Growth* **1972**, *12*, 169. [CrossRef]
17. Bugakov, V.L.; Gitsu, D.V.; Dolma, V.A.; Loisher, A.M.; Kotrubenko, B.P.; Laptev, A.V.; Akad, I. *Nauk Mold. SSSR Ser. Fiz-Tech. Mat. Nauk* **1976**, *3*, 29.
18. Velikanova, T.; Turchanin, M.; Lukas, H.L. Bismuth–Indium–Antimony. In *Landolt-Bornstein—Group IV Physical Chemistry*; Springer: Berlin, Germany, 2007; pp. 168–190.
19. Zilko, J.L.; Greene, J.E. Growth of metastable $\text{InSb}_{1-x}\text{Bi}_x$ thin films by multitarget sputtering. *Appl. Phys. Lett.* **1978**, *33*, 254–256. [CrossRef]
20. Zilko, J.L.; Greene, J.E. Growth and phase stability of epitaxial metastable $\text{InSb}_{1-x}\text{Bi}_x$ films on GaAs. I. Crystal growth. *J. Appl. Phys.* **1980**, *51*, 1549–1559. [CrossRef]
21. Oe, K.; Ando, S.; Sugiyama, K. $\text{InSb}_{1-x}\text{Bi}_x$ films grown by molecular-beam epitaxy. *Jpn. J. Appl. Phys.* **1981**, *20*, L303–L306. [CrossRef]

22. Noreika, A.J. Indium antimonide-bismuth compositions grown by molecular beam epitaxy. *J. Appl. Phys.* **1982**, *53*, 4932–4937. [\[CrossRef\]](#)
23. Noreika, A.J.; Gregg, J., Jr.; Takei, W.J.; Francombe, M.H. Properties of MBE grown InSb and InSb_{1-x}Bi_x. *J. Vac. Sci. Technol. A* **1983**, *1*, 558–561. [\[CrossRef\]](#)
24. Humphreys, T.P.; Chiang, P.K.; Bedair, S.M.; Parikh, N.R. Metalorganic chemical vapor deposition and characterization of the In-As-Sb-Bi material system for infrared detection. *Appl. Phys. Lett.* **1988**, *53*, 142–144. [\[CrossRef\]](#)
25. Ma, K.Y.; Fang, Z.M.; Jaw, D.H.; Cohen, R.M.; Stringfellow, G.B.; Kosar, W.P.; Brown, D.W. Organometallic vapor phase epitaxial growth and characterization of InAsBi and InAsSbBi. *Appl. Phys. Lett.* **1989**, *55*, 2420–2422. [\[CrossRef\]](#)
26. Ma, K.Y.; Fang, Z.M.; Cohen, R.M.; Stringfellow, G.B. Organometallic vapor-phase epitaxy growth and characterization of Bi-containing III/V alloys. *J. Appl. Phys.* **1990**, *68*, 4586–4591. [\[CrossRef\]](#)
27. Elayech, N.; Fitouri, H.; Essouda, Y.; Rebey, A.; El Jani, B. Thermodynamic study of the ternary system gallium-arsenic-bismuth. *Phys. Status Solidi (c)* **2015**, *12*, 138–141. [\[CrossRef\]](#)
28. Huang, K.T.; Chiu, C.T.; Cohen, R.M.; Stringfellow, G.B. InAsSbBi alloys grown by organometallic vapor-phase epitaxy. *J. Appl. Phys.* **1994**, *75*, 2857. [\[CrossRef\]](#)
29. Wagener, M.C.; Botha, J.R.; Leitch, A.W.R. Characterization of secondary phases formed during MOVPE growth of InSbBi mixed crystals. *J. Cryst. Growth* **2000**, *213*, 51–56. [\[CrossRef\]](#)
30. Lee, J.J.; Kim, J.D.; Razeghi, M. Room temperature operation of 8–12 μm InSbBi infrared photodetectors on GaAs substrates. *Appl. Phys. Lett.* **1998**, *73*, 602–604. [\[CrossRef\]](#)
31. Razeghi, M. Overview of antimonide based III-V semiconductor epitaxial layers and their applications at the center for quantum devices. *Eur. Phys. J. Appl. Phys.* **2003**, *23*, 149–205. [\[CrossRef\]](#)
32. Oe, K.; Okamoto, H. New semiconductor alloy GaAs_{1-x}Bi_x grown by metal organic vapor phase epitaxy. *Jpn. J. Appl. Phys. Part 2* **1998**, *37*, L1283–L1285. [\[CrossRef\]](#)
33. Zinovev, V.; Morgun, A.I.; Ufimtsev, V.B.; Arshavskii, A. Photoluminescence of epitaxial GaAsBi films. *Semiconductors* **1986**, *20*, 209–210.
34. Germogenov, V.P.; Otman, Y.I.; Chaldyshev, V.V. Appearance of natural acceptors in GaSb due to isovalent doping with bismuth. *Semiconductors* **1990**, *24*, 689–693.
35. Chaldyshev, V.V.; Germogenov, V.P.; Shmartsev, Y.V. Photoluminescence of bismuth doped GaSb. *Key Eng. Mater.* **1992**, *65*, 109–116.
36. Gladkov, P.; Monova, E.; Weber, J. Liquid phase epitaxy and photoluminescence characterization of p-type GaSb layers grown from Bi based melts. *J. Cryst. Growth* **1995**, *146*, 319–325. [\[CrossRef\]](#)
37. Mascarenhas, A.; Zhang, Y.; Verley, J.; Seong, M.J. Overcoming limitations in semiconductor alloy design. *Superlattices Microstructures* **2001**, *29*, 395–404. [\[CrossRef\]](#)
38. Weyers, M.; Sato, M.; Ando, H. Red shift of photoluminescence and absorption in dilute GaAsN alloy layers. *Jpn. J. Appl. Phys.* **1992**, *31*, L853–L855. [\[CrossRef\]](#)
39. Baillargeon, J.N.; Cheng, K.Y.; Hofler, G.E.; Pearah, P.J.; Hsieh, K.C. Luminescence quenching and the formation of the GaP_{1-x}N_x alloy in GaP with increasing nitrogen content. *Appl. Phys. Lett.* **1992**, *60*, 2540–2542. [\[CrossRef\]](#)
40. Kondow, M.; Uomi, K.; Niwa, A.; Kitatani, T.; Watahiki, S.; Yazawa, Y. GaInNAs: A novel material for long-wavelength-range laser diodes with excellent high-temperature performance. *Jpn. J. Appl. Phys.* **1996**, *35*, 1273–1275. [\[CrossRef\]](#)
41. Kitatani, T.; Nakahara, K.; Kondow, M.; Uomi, K.; Tanaka, T. A 1.3- μm single-quantum-well laser diode with a high characteristic temperature over 200 K. *Jpn. J. Appl. Phys.* **2000**, *39*, 86–87. [\[CrossRef\]](#)
42. Young, D.L.; Geisz, J.F.; Coutts, T.J. Nitrogen-induced decrease of the electron effective mass in GaAs_{1-x}N_x thin films measured by thermomagnetic transport phenomena. *Appl. Phys. Lett.* **2003**, *82*, 1236–1238. [\[CrossRef\]](#)
43. Wang, S.M.; Adolfsson, G.; Zhao, H.; Wei, Y.Q.; Gustavsson, J.; Zhao, Q.X.; Sadeghi, M.; Larsson, A. Growth of GaInNAs and 1.3 μm edge emitting lasers by molecular beam epitaxy. *J. Cryst. Growth* **2009**, *311*, 1863–1867. [\[CrossRef\]](#)
44. Tixier, S.; Adamcyk, M.; Tiedje, T.; Francoeur, S.; Mascarenhas, A.; Wei, P.; Schiettekatte, F. Molecular beam epitaxy growth of GaAs_{1-x}Bi_x. *Appl. Phys. Lett.* **2003**, *82*, 2245. [\[CrossRef\]](#)
45. Li, H.; Wang, Z.M. *Bismuth-Containing Compounds*; Springer: Chengdu, China, 2013.

46. Carrier, P.; Wei, S.-H. Calculated spin-orbit splitting of all diamondlike and zinc-blende semiconductors: Effects of $p_{1/2}$ local orbitals and chemical trends. *Phys. Rev. B* **2004**, *70*, 035212. [[CrossRef](#)]
47. Fluegel, B.; Francoeur, S.; Mascarenhas, A.; Tixier, S.; Young, E.C.; Tiedje, T. Giant spin-orbit bowing in $\text{GaAs}_{1-x}\text{Bi}_x$. *Phys. Rev. Lett.* **2006**, *97*, 067205. [[CrossRef](#)] [[PubMed](#)]
48. Yoshida, J.; Kita, T.; Wada, O.; Oe, K. Temperature dependence of $\text{GaAs}_{1-x}\text{Bi}_x$ band gap studied by photoreflectance spectroscopy. *Jpn. J. Appl. Phys.* **2003**, *42*, 371–374. [[CrossRef](#)]
49. Hossain, N.; Marko, I.P.; Jin, S.R.; Hild, K.; Sweeney, S.J.; Lewis, R.B.; Beaton, D.A.; Tiedje, T. Recombination mechanisms and band alignment of $\text{GaAs}_{1-x}\text{Bi}_x/\text{GaAs}$ light emitting diodes. *Appl. Phys. Lett.* **2012**, *100*, 051105. [[CrossRef](#)]
50. Kini, R.N.; Bhusal, L.; Ptak, A.J.; France, R.; Mascarenhas, A. Electron Hall mobility in GaAsBi . *J. Appl. Phys.* **2009**, *106*, 043705. [[CrossRef](#)]
51. Beaton, D.A.; Lewis, R.B.; Masnadi-Shirazi, M.; Tiedje, T. Temperature dependence of hole mobility in $\text{GaAs}_{1-x}\text{Bi}_x$ alloys. *J. Appl. Phys.* **2010**, *108*, 083708. [[CrossRef](#)]
52. Pillai, M.R.; Kim, S.S.; Ho, S.T.; Barnett, S.A. Growth of $\text{In}_x\text{Ga}_{1-x}\text{As}/\text{GaAs}$ heterostructures using Bi as a surfactant. *J. Vac. Sci. Technol. B* **2000**, *18*, 1232–1236. [[CrossRef](#)]
53. Sweeney, S.J.; Jin, S.R. Bismide-nitride alloys: Promising for efficient light emitting devices in the near- and mid-infrared. *J. Appl. Phys.* **2013**, *113*, 043110. [[CrossRef](#)]
54. Ludwig, P.; Knaub, N.; Hossain, N.; Reinhard, S.; Nattermann, L.; Marko, I.P.; Jin, S.R.; Hild, K.; Chatterjee, S.; Stolz, W.; et al. Electrical injection $\text{Ga}(\text{AsBi})/(\text{AlGa})\text{As}$ single quantum well laser. *Appl. Phys. Lett.* **2013**, *102*, 242115. [[CrossRef](#)]
55. Vurgaftman, I.; Meyer, J.R.; Ram-Mohan, L.R. Band parameters for III–V compound semiconductors and their alloys. *J. Appl. Phys.* **2001**, *89*, 5815. [[CrossRef](#)]
56. Smith, D.L.; Mailhot, C. Theory of semiconductor superlattice electronic structure. *Rev. Modern Phys.* **1990**, *62*, 173–234. [[CrossRef](#)]
57. Burt, M.G. The justification for applying the effective-mass approximation to microstructures. *J. Phys.-Condens. Matter* **1992**, *4*, 6651–6690. [[CrossRef](#)]
58. Broderick, C.A.; Usman, M.; Sweeney, S.J.; O'Reilly, E.P. Band engineering in dilute nitride and bismide semiconductor lasers. *Semicond. Sci. Technol.* **2012**, *27*, 094011. [[CrossRef](#)]
59. Alberi, K.; Dubon, O.D.; Walukiewicz, W.; Yu, K.M.; Bertulis, K.; Krotkus, A. Valence band anticrossing in $\text{GaBi}_x\text{As}_{1-x}$. *Appl. Phys. Lett.* **2007**, *91*, 051909. [[CrossRef](#)]
60. Deng, H.-X.; Li, J.; Li, S.-S.; Peng, H.; Xia, J.-B.; Wang, L.-W.; Wei, S.-H. Band crossing in isovalent semiconductor alloys with large size mismatch: First-principles calculations of the electronic structure of Bi and N incorporated GaAs . *Phys. Rev. B* **2010**, *82*, 193204. [[CrossRef](#)]
61. Jin, S.; Sweeney, S.J. InGaAsBi alloys on InP for efficient near- and mid-infrared light emitting devices. *J. Appl. Phys.* **2013**, *114*, 213103. [[CrossRef](#)]
62. Petropoulos, J.P.; Zhong, Y.; Zide, J.M.O. Optical and electrical characterization of InGaBiAs for use as a mid-infrared optoelectronic material. *Appl. Phys. Lett.* **2011**, *99*, 031110. [[CrossRef](#)]
63. Batool, Z.; Hild, K.; Hosea, T.J.C.; Lu, X.; Tiedje, T.; Sweeney, S.J. The electronic band structure of $\text{GaBiAs}/\text{GaAs}$ layers: Influence of strain and band anti-crossing. *J. Appl. Phys.* **2012**, *111*, 113108. [[CrossRef](#)]
64. Marko, I.P.; Batool, Z.; Hild, K.; Jin, S.R.; Hossain, N.; Hosea, T.J.C.; Petropoulos, J.P.; Zhong, Y.; Dongmo, P.B.; Zide, J.M.O.; et al. Temperature and Bi-concentration dependence of the bandgap and spin-orbit splitting in $\text{InGaBiAs}/\text{InP}$ semiconductors for mid-infrared applications. *Appl. Phys. Lett.* **2012**, *101*, 221108. [[CrossRef](#)]
65. Wu, L.Y.; Han, L.H.; Li, X.Y.; Lu, P.F.; Wang, S.M. *Asia Communications and Photonics Conference (ACP 2015); Hong Kong, China, November 19–23 2015*; OSA publishing: Washington, DC, USA, 2015; ASu2A. 16.
66. Samajdar, D.P.; Dhar, S. Valence band structure of $\text{InAs}_{1-x}\text{Bi}_x$ and $\text{InSb}_{1-x}\text{Bi}_x$ alloy semiconductors calculated using valence band anticrossing model. *Sci. World J.* **2014**, *2014*, 704830. [[CrossRef](#)] [[PubMed](#)]
67. Usman, M.; Broderick, C.A.; Lindsay, A.; O'Reilly, E.P. Tight-binding analysis of the electronic structure of dilute bismide alloys of GaP and GaAs . *Phys. Rev. B* **2011**, *84*, 245202. [[CrossRef](#)]
68. Virkkala, V.; Havu, V.; Tuomisto, F.; Puska, M.J. Modeling Bi-induced changes in the electronic structure of $\text{GaAs}_{1-x}\text{Bi}_x$ alloys. *Phys. Rev. B* **2013**, *88*, 235201. [[CrossRef](#)]
69. Usman, M.; Broderick, C.A.; Batool, Z.; Hild, K.; Hosea, T.J.C.; Sweeney, S.J.; O'Reilly, E.P. Impact of alloy disorder on the band structure of compressively strained $\text{GaBi}_x\text{As}_{1-x}$. *Phys. Rev. B* **2013**, *87*, 115104. [[CrossRef](#)]

70. Fluegel, B.; Kini, R.N.; Ptak, A.J.; Beaton, D.; Alberi, K.; Mascarenhas, A. Shubnikov-de Haas measurement of electron effective mass in $\text{GaAs}_{1-x}\text{Bi}_x$. *Appl. Phys. Lett.* **2011**, *99*, 162108. [CrossRef]
71. Lindsay, A.; Tomić, S.; O'Reilly, E.P. Derivation of a 10-band model for dilute nitride semiconductors. *Solid State Electron.* **2003**, *47*, 443–446. [CrossRef]
72. Broderick, C.A.; Usman, M.; O'Reilly, E.P. 12-band $\mathbf{k}\cdot\mathbf{p}$ model for dilute bismide alloys of (In)GaAs derived from supercell calculations. *Phys. Status Solidi (b)* **2013**, *250*, 773–778. [CrossRef]
73. Broderick, C.A.; Usman, M.; O'Reilly, E.P. Derivation of 12- and 14-band $\mathbf{k}\cdot\mathbf{p}$ Hamiltonians for dilute bismide and bismide-nitride semiconductors. *Semicond. Sci. Technol.* **2013**, *28*, 125025. [CrossRef]
74. Samajdar, D.P.; Das, T.D.; Dhar, S. Calculation of direct E_0 energy gaps for III-V-Bi alloys using quantum dielectric theory. In *The Book Physics of Semiconductor Devices*; Springer International Publishing: Cham, Switzerland, 2014; pp. 779–781.
75. Belabbès, A.; Zaoui, A.; Ferhat, M. Lattice dynamics study of bismuth III–V compounds. *J. Phys.* **2008**, *20*, 415221. [CrossRef]
76. Madouri, D.; Ferhat, M. How do electronic properties of conventional III-V semiconductors hold for the III-V boron bismuth BBi compound? *Phys. Status Solidi (b)* **2005**, *242*, 2856–2863. [CrossRef]
77. Reshak, A.H.; Kamarudin, H.; Auluck, S.; Kityk, I.V. Bismuth in gallium arsenide: Structural and electronic properties of $\text{GaAs}_{1-x}\text{Bi}_x$ alloys. *J. Solid State Chem.* **2012**, *186*, 47–53. [CrossRef]
78. Abdiche, A.; Abid, H.; Riane, R.; Bouaza, A. Structural and electronic properties of zinc blend $\text{GaAs}_{1-x}\text{Bi}_x$ solid solutions. *Physica B* **2010**, *405*, 2311–2316. [CrossRef]
79. Jacobsen, H.; Puchala, B.; Kuech, T.F.; Morgan, D. *Ab initio* study of the strain dependent thermodynamics of Bi doping in GaAs. *Phys. Rev. B* **2012**, *86*, 085207. [CrossRef]
80. Berding, M.A.; Sher, A.; Chen, A.B.; Miller, W.E. Structural properties of bismuth-bearing semiconductor alloys. *J. Appl. Phys.* **1988**, *63*, 107–115. [CrossRef]
81. Mbarki, M.; Alaya, R.; Rebey, A. *Ab initio* investigation of structural and electronic properties of zinc blende $\text{AlN}_{1-x}\text{Bi}_x$ alloys. *Solid State Commun.* **2013**, *155*, 12–15. [CrossRef]
82. Mbarki, M.; Rebey, A. First principles calculations of structural and electronic properties of $\text{GaN}_{1-x}\text{Bi}_x$ alloys. *J. Alloys Compd.* **2012**, *530*, 36–39. [CrossRef]
83. Wu, L.; Lu, P.; Yang, C.; Liang, D.; Zhang, C.; Wang, S. The effect of BiIn hetero-antisite defects in $\text{In}_{1-x}\text{PBi}_x$ alloy. *J. Alloys Compd.* **2016**, *674*, 21–25. [CrossRef]
84. Punkkinen, M.P.J.; Laukkanen, P.; Komsa, H.P.; Ahola-Tuomi, M.; Räsänen, N.; Kokko, K.; Kuzmin, M.; Adell, J.; Sadowski, J.; Perälä, R.E.; et al. Bismuth-stabilized (2×1) and (2×4) reconstructions on GaAs(100) surfaces: Combined first-principles, photoemission, and scanning tunneling microscopy study. *Phys. Rev. B* **2008**, *78*, 195304. [CrossRef]
85. Murase, I.; Akiyama, T.; Nakamura, K.; Ito, T. *Ab initio*-based approach to initial incorporation of Bi on GaAs (001)- $c(4 \times 4)$ α surface. *J. Cryst. Growth* **2013**, *378*, 21–24. [CrossRef]
86. Achour, H.; Louhibi, S.; Amrani, B.; Tebboune, A.; Sekkal, N. Structural and electronic properties of GaAsBi. *Superlattices Microstructures* **2008**, *44*, 223–229. [CrossRef]
87. Qi, J.S.; Shi, D.S.; Zhao, J.J.; Jiang, X.F. Stable structures and electronic properties of the oriented Bi nanowires and nanotubes from first-principle calculations. *J. Phys. Chem.* **2008**, *112*, 10745–10753. [CrossRef]
88. Gupta, U.; Reveles, J.U.; Melko, J.J.; Khanna, S.N.; Castleman, A.W., Jr. Electron delocalization in a non-cyclic all-metal III–V cluster. *Chem. Phys. Lett.* **2009**, *480*, 189–192. [CrossRef]
89. Gupta, U.; Reveles, J.U.; Melko, J.J.; Khanna, S.N.; Castleman, A.W., Jr. Electronic structure of Bi_3Ga_y semiconductor clusters and the special stability of Bi_3Ga_2 —A gas phase Zintl analogue. *Chem. Phys. Lett.* **2009**, *467*, 223–229. [CrossRef]
90. Gupta, U.; Reveles, J.U.; Melko, J.J.; Khanna, S.N.; Castleman, A.W., Jr. Origins of stability in mixed bismuth-indium clusters. *J. Phys. Chem. C* **2010**, *114*, 15963–15972. [CrossRef]
91. Akola, J.; Atodiresi, N.; Kalikka, J.; Larrucea, J.; Jones, R.O. Structure and dynamics in liquid bismuth and Bi(n) clusters: A density functional study. *J. Chem. Phys.* **2014**, *141*, 194503. [CrossRef] [PubMed]
92. Amrani, B.; Achour, H.; Louhibi, S.; Tebboune, A.; Sekkal, N. First principles study of AlBi. *Solid State Commun.* **2008**, *148*, 59–62. [CrossRef]
93. Mbarki, M.; Rebey, A. First-principles calculation of the physical properties of $\text{GaAs}_{1-x}\text{Bi}_x$ alloys. *Semicond. Sci. Technol.* **2011**, *26*, 105020. [CrossRef]

94. Ding, L.; Lu, P.; Cao, H.; Cai, N.; Yu, Z.; Gao, T.; Wang, S. Bismuth alloying properties in GaAs nanowires. *J. Solid State Chem.* **2013**, *205*, 44–48. [[CrossRef](#)]
95. Belabbes, A.; Zaoui, A.; Laref, S.; Ferhat, M. Imposing changes of band and spin–orbit gaps in GaNBi. *Solid State Commun.* **2012**, *152*, 1700–1702. [[CrossRef](#)]
96. Madouri, D.; Boukra, A.; Zaoui, A.; Ferhat, M. Bismuth alloying in GaAs: A first-principles study. *Comput. Mater. Sci.* **2008**, *43*, 818–822. [[CrossRef](#)]
97. Yu, L.; Li, D.; Zhao, S.; Li, G.; Yang, K. First principles study on electronic structure and optical properties of ternary GaAs:Bi alloy. *Materials* **2012**, *5*, 2486–2497. [[CrossRef](#)]
98. Nikulin, V.K.; Guschina, N.A. Single-electron charge transfer and excitations at collisions between Bi⁴⁺ ions in the kiloelectronvolt energy range. *Tech. Phys.* **2007**, *52*, 148–158. [[CrossRef](#)]
99. Dai, J.; Manson, J.R. Theoretical analysis for the determination of surface composition in molten Ga–Bi metal alloys by rare gas scattering. *J. Chem. Phys.* **2003**, *119*, 9842. [[CrossRef](#)]
100. Imhof, S.; Wagner, C.; Chernikov, A.; Koch, M.; Kolata, K.; Köster, N.S.; Chatterjee, S.; Koch, S.W.; Lu, X.; Johnson, S.R.; et al. Evidence of two disorder scales in Ga(AsBi). *Phys. Status Solidi (b)* **2011**, *248*, 851–854. [[CrossRef](#)]
101. Keen, B.; Makin, R.; Stampe, P.A.; Kennedy, R.J.; Sallis, S.; Piper, L.J.; McCombe, B.; Durbin, S.M. Growth parameters for thin film InBi grown by molecular beam epitaxy. *J. Electron. Mater.* **2014**, *43*, 914–920. [[CrossRef](#)]
102. Ferhat, M.; Zaoui, A. Structural and electronic properties of III–V bismuth compounds. *Phys. Rev. B* **2006**, *73*, 115107. [[CrossRef](#)]
103. Wang, S.Q.; Ye, H.Q. Plane-wave pseudopotential study on mechanical and electronic properties for IV and III–V crystalline phases with zinc-blende structure. *Phys. Rev. B* **2002**, *66*, 235111. [[CrossRef](#)]
104. Zaoui, A.; Madouri, D.; Ferhat, M. First-principles study of the ground state stability of III–V bismuth compounds. *Philos. Mag. Lett.* **2009**, *89*, 807–813. [[CrossRef](#)]
105. Duzik, A.; Thomas, J.C.; Millunchick, J.M.; Lång, J.; Punkkinen, M.P.J.; Laukkanen, P. Surface structure of bismuth terminated GaAs surfaces grown with molecular beam epitaxy. *Surf. Sci.* **2012**, *606*, 1203–1207. [[CrossRef](#)]
106. Masnadi-Shirazi, M.; Beaton, D.A.; Lewis, R.B.; Lu, X.; Tiedje, T. Surface reconstructions during growth of GaAs_{1–x}Bi_x alloys by molecular beam epitaxy. *J. Cryst. Growth* **2012**, *338*, 80–84. [[CrossRef](#)]
107. Norman, A.G.; France, R.; Ptak, A.J. Atomic ordering and phase separation in MBE GaAs_{1–x}Bi_x. *J. Vac. Sci. Technol. B* **2011**, *29*, 03C121. [[CrossRef](#)]
108. Ahola-Tuomi, M.; Laukkanen, P.; Perälä, R.E.; Kuzmin, M.; Pakarinen, J.; Väyrynen, I.J.; Adell, M. Structural properties of Bi-terminated GaAs (001) surface. *Surf. Sci.* **2006**, *600*, 2349–2354. [[CrossRef](#)]
109. Bastiman, F.; Cullis, A.G.; David, J.P.R.; Sweeney, S.J. Bi incorporation in GaAs(100)-2 × 1 and 4 × 3 reconstructions investigated by RHEED and STM. *J. Cryst. Growth* **2012**, *341*, 19–23. [[CrossRef](#)]
110. Wu, M.; Luna, E.; Puustinen, J.; Guina, M.; Trampert, A. Formation and phase transformation of Bi-containing QD-like clusters in annealed GaAsBi. *Nanotechnology* **2014**, *25*, 205605. [[CrossRef](#)] [[PubMed](#)]
111. Morgan, J.A.; Nathanson, G.M. Atom scattering from atomic surfactants: Collisions of argon with a dilute Bi:Ga solution. *J. Chem. Phys.* **2001**, *114*, 1958–1961. [[CrossRef](#)]
112. Fan, D.; Zeng, Z.; Dorogan, V.G.; Hirono, Y.; Li, C.; Mazur, Y.I.; Yu, S.-Q.; Johnson, S.R.; Wang, Z.M.; Salamo, G.J. Bismuth surfactant mediated growth of InAs quantum dots by molecular beam epitaxy. *J. Mater. Sci.* **2012**, *24*, 1635–1639. [[CrossRef](#)]
113. Tixier, S.; Adamczyk, M.; Young, E.C.; Schmid, J.H.; Tiedje, T. Surfactant enhanced growth of GaNAs and InGaNAs using bismuth. *J. Cryst. Growth* **2003**, *251*, 449–454. [[CrossRef](#)]
114. Okamoto, H.; Tawara, T.; Gotoh, H.; Kamada, H.; Sogawa, T. Growth and characterization of telecommunication-wavelength quantum dots using Bi as a surfactant. *Jpn. J. Appl. Phys.* **2010**, *49*, 06GJ01. [[CrossRef](#)]
115. Gu, Y.; Zhang, Y.-G.; Song, Y.-X.; Ye, H.; Cao, Y.-Y.; Li, A.-Z.; Wang, S.-M. Optical properties of InGaAsBi/GaAs strained quantum wells studied by temperature-dependent photoluminescence. *Chin. Phys. B* **2013**, *22*, 037802. [[CrossRef](#)]
116. Wang, K.; Gu, Y.; Zhou, H.F.; Zhang, L.Y.; Kang, C.Z.; Wu, M.J.; Pan, W.W.; Lu, P.F.; Gong, Q.; Wang, S.M. InPBi single crystals grown by molecular beam epitaxy. *Sci. Rep.* **2014**, *4*, 5449. [[CrossRef](#)] [[PubMed](#)]

117. Wang, K.; Wang, P.; Pan, W.W.; Wu, X.Y.; Yue, L.; Gong, Q.; Wang, S.M. Growth of semiconductor alloy InGaPBi on InP by molecular beam epitaxy. *Semicond. Sci. Technol.* **2015**, *30*, 094006. [[CrossRef](#)]
118. Wang, S.M. Dilute III-PBi and III-SbBi for IR applications. In Proceedings of the 18th International Conference on Transparent Optical Networks ICTON 2016, Trento, Italy, 10–14 July 2016.
119. Jiang, W.Y.; Liu, J.Q.; So, M.G.; Myrtle, K.; Kavanagh, K.L.; Watkins, S.P. Surface modifications induced by bismuth on (001) GaAs surfaces. *J. Cryst. Growth* **2005**, *277*, 85–90. [[CrossRef](#)]
120. Fitouri, H.; Moussa, I.; Rebey, A.; El Jani, B. Surface analysis of different oriented GaAs substrates annealed under bismuth flow. *J. Cryst. Growth* **2007**, *300*, 347–352. [[CrossRef](#)]
121. Huber, P.; Shpyrko, O.G.; Pershan, P.S.; Ocko, B.M.; Di Masi, E.; Deutsch, M. Tetra point wetting at the free surface of liquid Ga-Bi. *Phys. Rev. Lett.* **2002**, *89*, 035502. [[CrossRef](#)] [[PubMed](#)]
122. Lu, X.; Beaton, D.A.; Lewis, R.B.; Tiedje, T.; Whitwick, M.B. Effect of molecular beam epitaxy growth conditions on the Bi content of GaAs_{1-x}Bi_x. *Appl. Phys. Lett.* **2008**, *92*, 192110. [[CrossRef](#)]
123. Sterzer, E.; Knaub, N.; Ludewig, P.; Straubinger, R.; Beyer, A.; Volz, K. Investigation of the microstructure of metallic droplets on Ga(AsBi)/GaAs. *J. Cryst. Growth* **2014**, *408*, 71–77. [[CrossRef](#)]
124. Dominguez, L.; Reyes, D.F.; Bastiman, F.; Sales, D.L.; Richards, R.D.; Mendes, D.; David, J.P.R.; Gonzalez, D. Formation of tetragonal InBi clusters in InAsBi/InAs(100) heterostructures grown by molecular beam epitaxy. *Appl. Phys. Express* **2013**, *6*, 112601. [[CrossRef](#)]
125. Young, E.C.; Whitwick, M.B.; Tiedje, T.; Beaton, D.A. Bismuth incorporation in GaAs_{1-x}Bi_x grown by molecular beam epitaxy with *in-situ* light scattering. *Phys. Status Solidi (c)* **2007**, *4*, 1707–1710. [[CrossRef](#)]
126. Reyes, K.; Smereka, P.; Nothorn, D.; Millunchick, J.M.; Bietti, S.; Somaschini, C.; Sanguinetti, S.; Frigeri, C. Unified model of droplet epitaxy for compound semiconductor nanostructures: Experiments and theory. *Phys. Rev. B* **2013**, *87*, 165406. [[CrossRef](#)]
127. Vardar, G.; Paleg, S. W.; Warren, M. V.; Kang, M.; Jeon, S.; Goldman, R.S. Mechanisms of droplet formation and Bi incorporation during molecular beam epitaxy of GaAsBi. *Appl. Phys. Lett.* **2013**, *102*, 042106. [[CrossRef](#)]
128. Fitouri, H.; Moussa, I.; Rebey, A.; El Jani, B. Study of GaAsBi MOVPE growth on (100) GaAs substrate under high Bi flow rate by high resolution X-ray diffraction. *Microelectron. Eng.* **2011**, *88*, 476–479. [[CrossRef](#)]
129. Ptak, A.J.; France, R.; Beaton, D.A.; Alberi, K.; Simon, J.; Mascarenhas, A.; Jiang, C.S. Kinetically limited growth of GaAsBi by molecular-beam epitaxy. *J. Cryst. Growth* **2012**, *338*, 107–110. [[CrossRef](#)]
130. Pačebutas, V.; Butkutė, R.; Čechavičius, B.; Kavaliauskas, J.; Krotkus, A. Photoluminescence investigation of GaAs_{1-x}Bi_x/GaAs heterostructures. *Thin Solid Films* **2012**, *520*, 6415–6418. [[CrossRef](#)]
131. Duzik, A.; Millunchick, J.M. Surface morphology and Bi incorporation in GaSbBi(As)/GaSb films. *J. Cryst. Growth* **2014**, *390*, 5–11. [[CrossRef](#)]
132. Ciatto, G.; Thomasset, M.; Glas, F.; Lu, X.; Tiedje, T. Formation and vanishing of short range ordering in GaAs_{1-x}Bi_x thin films. *Phys. Rev. B* **2010**, *82*, 201304. [[CrossRef](#)]
133. Young, E.C.; Tixier, S.; Tiedje, T. Bismuth surfactant growth of the dilute nitride GaN_xAs_{1-x}. *J. Cryst. Growth* **2005**, *279*, 316–320. [[CrossRef](#)]
134. Huang, W.; Oe, K.; Feng, G.; Yoshimoto, M. Molecular-beam epitaxy and characteristics of GaN_yAs_{1-x-y}Bi_x. *J. Appl. Phys.* **2005**, *98*, 053505. [[CrossRef](#)]
135. Bastiman, F.; Mohmad, A.R.B.; Ng, J.S.; David, J.P.R.; Sweeny, S.J. Non-stoichiometric GaAsBi/GaAs (100) molecular beam epitaxy growth. *J. Cryst. Growth* **2012**, *338*, 57–61. [[CrossRef](#)]
136. Lewis, R. B.; Masnadi-Shirazi, M.; Tiedje, T. Growth of high Bi concentration GaAs_{1-x}Bi_x by molecular beam epitaxy. *Appl. Phys. Lett.* **2012**, *101*, 082112. [[CrossRef](#)]
137. Richards, R.D.; Bastiman, F.; Hunter, C.J.; Mendes, D.F.; Mohmad, A.R.; Roberts, J.S.; David, J.P.R. Molecular beam epitaxy growth of GaAsBi using As₂ and As₄. *J. Cryst. Growth* **2014**, *290*, 120–124. [[CrossRef](#)]
138. Liu, X.; Prasad, A.; Nishio, J.; Weber, E. R.; Liliental-Weber, Z.; Walukiewicz, W. Native point defects in low-temperature-grown GaAs. *Appl. Phys. Lett.* **1995**, *67*, 279–281. [[CrossRef](#)]
139. Gebauer, J.; Krause-Rehberg, R.; Eichler, S.; Luysberg, M.; Sohn, H.; Weber, E.R. Ga vacancies in low-temperature-grown GaAs identified by slow positrons. *Appl. Phys. Lett.* **1997**, *71*, 638–640. [[CrossRef](#)]
140. Warren, A.C.; Woodail, J.M.; Freeouf, J.L.; Grischkowsky, J.L.D.; McInturff, D.T. Arsenic precipitates and the semi-insulating properties of GaAs buffer layers grown by low temperature molecular beam epitaxy. *Appl. Phys. Lett.* **1990**, *57*, 1331–1333. [[CrossRef](#)]

141. Puustinen, J.; Wu, M.; Luna, E.; Schramm, A.; Laukkanen, P.; Laitinen, M.; Sajavaara, T.; Guina, M. Variation of lattice constant and cluster formation in GaAsBi. *J. Appl. Phys.* **2013**, *114*, 243504. [\[CrossRef\]](#)
142. Kesaria, M.; Birindelli, S.; Velichko, A. V.; Zhuang, Q. D.; Patane, A.; Capizzi, M.; Krier, A. In(AsN) mid-infrared emission enhanced by rapid thermal annealing. *Infrared Phys. Technol.* **2015**, *68*, 138–142. [\[CrossRef\]](#)
143. Tominaga, Y.; Kinoshita, Y.; Oe, K.; Yoshimoto, M. Structural investigation of GaAs_{1-x}Bi_x/GaAs multiquantum wells. *Appl. Phys. Lett.* **2008**, *93*, 131915. [\[CrossRef\]](#)
144. Butkutė, R.; Pačebutas, V.; Čechavičius, B.; Adomavičius, R.; Koroliov, A.; Krotkus, A. Thermal annealing effect on the properties of GaBiAs. *Phys. Status Solidi (c)* **2012**, *9*, 1614–1616. [\[CrossRef\]](#)
145. Mohmad, A.R.; Bastiman, F.; Hunter, C.J.; Richards, R.; Sweeney, S.J.; Ng, J.S.; David, J.P.R. Effects of rapid thermal annealing on GaAs_{1-x}Bi_x alloys. *Appl. Phys. Lett.* **2012**, *101*, 012106. [\[CrossRef\]](#)
146. Mazzucato, S.; Boonpeng, P.; Carrère, H.; Lagarde, D.; Arnoult, A.; Lacoste, G.; Zhang, T.; Balocchi, A.; Amand, T.; Marie, X.; et al. Reduction of defect density by rapid thermal annealing in GaAsBi studied by time-resolved photoluminescence. *Semicond. Sci. Technol.* **2013**, *28*, 022001. [\[CrossRef\]](#)
147. Grant, P.C.; Fan, D.; Mosleh, A.; Yu, S.Q.; Dorogan, V.G.; Hawkridge, M.E.; Mazur, Y.I.; Benamara, M.; Salamo, G.J.; Johnson, S.R. Rapid thermal annealing effect on GaAsBi/GaAs single quantum wells grown by molecular beam epitaxy. *J. Vac. Sci. Technol. B* **2014**, *32*, 02C119. [\[CrossRef\]](#)
148. Moussa, I.; Fitouri, H.; Chine, Z.; Rebey, A.; El Jani, B. Effect of thermal annealing on structural and optical properties of the GaAs_{0.963}Bi_{0.037} alloy. *Semicond. Sci. Technol.* **2008**, *23*, 125034. [\[CrossRef\]](#)
149. Chine, Z.; Fitouri, H.; Zaied, I.; Rebey, A.; El Jani, B. Photoreflectance and photoluminescence study of annealing effects on GaAsBi layers grown by metalorganic vapor phase epitaxy. *Semicond. Sci. Technol.* **2010**, *25*, 065009. [\[CrossRef\]](#)
150. Feng, G.; Oe, K.; Yoshimoto, M. Influence of thermal annealing treatment on the luminescence properties of dilute GaNAs-bismide alloy. *Jpn. J. Appl. Phys.* **2007**, *46*, L764–L766. [\[CrossRef\]](#)
151. Ye, H.; Song, Y.; Gu, Y.; Wang, S. Light emission from InGaAs:Bi/GaAs quantum wells at 1.3 μm. *AIP Adv.* **2012**, *2*, 042158. [\[CrossRef\]](#)
152. Wu, X.Y.; Wang, K.; Pan, W.W.; Wang, P.; Li, Y.Y.; Song, Y.X.; Gu, Y.; Yue, L.; Xu, H.; Zhang, Z.P.; et al. Effect of rapid thermal annealing on InP_{1-x}Bi_x grown by molecular beam epitaxy. *Semicond. Sci. Technol.* **2015**, *30*, 094014. [\[CrossRef\]](#)
153. Nacer, S.; Aissat, A.; Ferdjani, K. Band gap and band offsets of GaNAsBi lattice matched to GaAs substrate. *Opt. Quantum Electron.* **2008**, *40*, 677–683. [\[CrossRef\]](#)
154. Novikova, S.V.; Winsera, A.J.; Lia, T.; Campiona, R.; Harrison, I.; Foxon, C.T. Bismuth a new dopant for GaN films grown by molecular beam epitaxy—surfactant effects, formation of GaN_{1-x}Bi_x alloys and co-doping with arsenic. *J. Cryst. Growth* **2003**, *247*, 35–41. [\[CrossRef\]](#)
155. Levander, A.X.; Yu, K.M.; Novikov, S.V.; Tseng, A.; Foxon, C.T.; Dubon, O.D.; Wu, J.; Walukiewicz, W. GaN_{1-x}Bi_x: Extremely mismatched semiconductor alloys. *Appl. Phys. Lett.* **2010**, *97*, 141919. [\[CrossRef\]](#)
156. Novikov, S.V.; Yu, K.M.; Levander, A.X.; Liliental-Weber, Z.; dos Reis, R.; Kent, A.J.; Tseng, A.; Dubon, O.D.; Wu, J.; Denlinger, J.; et al. Molecular beam epitaxy of GaN_{1-x}Bi_x alloys with high bismuth content. *Phys. Status Solidi (a)* **2012**, *209*, 419–423. [\[CrossRef\]](#)
157. Gu, Y.; Wang, K.; Zhou, H.F.; Li, Y.Y.; Cao, C.F.; Zhang, L.Y.; Zhang, Y.G.; Gong, Q.; Wang, S.M. Structural and optical characterizations of InPBi thin films grown by molecular beam epitaxy. *Nanoscale Res. Lett.* **2014**, *9*, 24. [\[CrossRef\]](#) [\[PubMed\]](#)
158. Okamoto, H.; Oe, K. Growth of metastable alloy InAsBi by low-pressure MOVPE. *Jpn. J. Appl. Phys.* **1998**, *37*, 1608–1613. [\[CrossRef\]](#)
159. Pan, W.; Steele, J.A.; Wang, P.; Wang, K.; Song, Y.; Yue, L.; Wu, X.; Xu, H.; Zhang, Z.; Xu, S.; et al. Raman scattering studies of dilute InP_{1-x}Bi_x alloys reveal unusually strong oscillator strength for Bi-induced modes. *Semicond. Sci. Technol.* **2015**, *30*, 094003. [\[CrossRef\]](#)
160. Wei, G.N.; Tan, Q.H.; Dai, X.; Feng, Q.; Luo, W.G.; Sheng, Y.; Wang, K.; Pan, W.W.; Zhang, L.Y. Bismuth-content dependent polarized Raman spectrum of InPBi alloy. *Chin. Phys. B* **2016**, *25*, 066301. [\[CrossRef\]](#)
161. Kopaczek, J.; Kudrawiec, R.; Polak, M.P.; Scharoch, P.; Birkett, M.; Veal, T.D.; Wang, K.; Gu, Y.; Gong, Q.; Wang, S. Contactless electoreflectance and theoretical studies of band gap and spin-orbit splitting in InP_{1-x}Bi_x dilute bismide with $x \leq 0.034$. *Appl. Phys. Lett.* **2014**, *105*, 222104. [\[CrossRef\]](#)

162. Yue, L.; Wang, P.; Wang, K.; Wu, X.Y.; Pan, W.W.; Li, Y.Y.; Song, Y.X.; Gu, Y.; Gong, Q.; Wang, S.M.; et al. Novel InGaPBi single crystal grown by molecular beam epitaxy. *Appl. Phys. Express* **2015**, *8*, 041201. [[CrossRef](#)]
163. Ma, K.Y.; Fang, Z.M.; Cohen, R.M. Ultra-low temperature OMVPE of InAs and InAsBi. *J. Electron. Mater.* **1992**, *21*, 143. [[CrossRef](#)]
164. Svensson, S.P.; Hier, H.; Sarney, W.L.; Donetsky, D.; Wang, D.; Belenky, G. Molecular beam epitaxy control and photoluminescence properties of InAsBi. *J. Vac. Sci. Technol. B* **2012**, *30*, 02B109. [[CrossRef](#)]
165. Forghani, K.; Anand, A.; Mawst, L.J.; Kuech, T.F. Low temperature growth of GaAs_{1-y}Bi_y epitaxial layers. *J. Cryst. Growth* **2013**, *380*, 23–27. [[CrossRef](#)]
166. Rajpalke, M.K.; Linhart, W.M.; Birkett, M.; Yu, K.M.; Alaria, J.; Kopaczek, J.; Kudrawiec, R.; Jones, T.S.; Ashwin, M.J.; Veal, T.D. High Bi content GaSbBi alloys. *J. Appl. Phys.* **2014**, *116*, 043511. [[CrossRef](#)]
167. Barnett, S.A. Direct E₀ energy gaps of bismuth-containing III–V alloys predicted using quantum dielectric theory. *J. Vac. Sci. Technol. A* **1987**, *5*, 2845. [[CrossRef](#)]
168. Fang, Z.M.; Ma, K.Y.; Cohen, R.M.; Stringfellow, G.B. Photoluminescence of InAsBi and InAsSbBi grown by organometallic vapor phase epitaxy. *J. Appl. Phys.* **1990**, *68*, 1187–1191. [[CrossRef](#)]
169. Okamoto, H.; Oe, K. Structural and energy-gap characterization of metalorganic-vapor-phase-epitaxy-grown InAsBi. *Jpn. J. Appl. Phys.* **1999**, *38*, 1022–1025. [[CrossRef](#)]
170. Feng, G.; Yoshimoto, M.; Oe, K.; Chayahara, A.; Horino, Y. New III–V semiconductor InGaAsBi alloy grown by molecular beam epitaxy. *Jpn. J. Appl. Phys.* **2005**, *44*, L1161–L1163. [[CrossRef](#)]
171. Devenson, J.; Pačebutas, V.; Butkutė, R.; Baranov, A.; Krotkus, A. Structure and optical properties of InGaAsBi with up to 7% bismuth. *Appl. Phys. Express* **2012**, *5*, 015503. [[CrossRef](#)]
172. Zhong, Y.; Dongmo, P.B.; Petropoulos, J.P.; Zide, J.M.O. Effects of molecular beam epitaxy growth conditions on composition and optical properties of In_xGa_{1-x}Bi_yAs_{1-y}. *Appl. Phys. Lett.* **2012**, *100*, 112110. [[CrossRef](#)]
173. Halka, V.; Freyland, W. Thermal stability of surface freezing films in Ga-based alloys: An X-ray photoelectron spectroscopy and scanning tunneling microscopy study. *J. Chem. Phys.* **2007**, *127*, 034702. [[CrossRef](#)] [[PubMed](#)]
174. Chen, X.; Song, Y.; Zhu, L.; Wang, S. M.; Lu, W.; Guo, S.; Shao, J. Shallow-terrace-like interface in dilute-bismuth GaSb/AlGaSb single quantum wells evidenced by photoluminescence. *J. Appl. Phys.* **2013**, *113*, 153505. [[CrossRef](#)]
175. Kudrawiec, R.; Kopaczek, J.; Misiewicz, J.; Petropoulos, J.P.; Zhong, Y.; Zide, J.M.O. Contactless electroreflectance study of E₀ and E₀+Δ_{SO} transitions in In_{0.53}Ga_{0.47}Bi_xAs_{1-x} alloys. *Appl. Phys. Lett.* **2011**, *99*, 251906. [[CrossRef](#)]
176. Zaied, I.; Fitouri, H.; Chine, Z.; Rebey, A.; El Jani, B. Atmospheric-pressure metal-organic vapor-phase epitaxy of GaAsBi alloys on high-index GaAs substrates. *J. Phys. Chem. Solids* **2014**, *75*, 244–251. [[CrossRef](#)]
177. Mazur, Y.I.; Dorogan, V.G.; Benamara, M.; Ware, M.E.; Schmidbauer, M.; Tarasov, G.G.; Johnson, S.R.; Lu, X.; Yu, S.Q.; Tiedje, T.; et al. Effects of spatial confinement and layer disorder in photoluminescence of GaAs_{1-x}Bi_x/GaAs heterostructures. *J. Phys. D* **2013**, *46*, 065306. [[CrossRef](#)]
178. Hosea, T.J.C.; Marko, I.P.; Batool, Z.; Hild, K.; Jin, S.R.; Hossain, T.; Chai, G.M.T.; Sweeney, S.J.; Petropoulos, J.P.; Zhong, Y.; et al. InGaBiAs/InP semiconductors for mid-infrared applications: Dependence of bandgap and spin-orbit splitting on temperature and bismuth content. In Proceedings of the IEEE 3rd International Conference on Photonics, Penang, Malaysia, 1–3 October 2012; pp. 154–158.
179. Song, Y.; Wang, S.; Saha Roy, I.; Shi, P.; Hallen, A.; Lai, Z. Molecular beam epitaxy growth of InSb_{1-x}Bi_x thin films. *J. Cryst. Growth* **2013**, *378*, 323–328. [[CrossRef](#)]
180. Rajpalke, M.K.; Linhart, W.M.; Yu, K.M.; Birkett, M.; Alaria, J.; Bomphrey, J.J.; Sallis, S.; Piper, L.F.J.; Jones, T.S.; Ashwin, M.J.; et al. Bi-induced band gap reduction in epitaxial InSbBi alloys. *Appl. Phys. Lett.* **2014**, *105*, 212101. [[CrossRef](#)]
181. Dixita, V.K.; Keerthia, K.S.; Berab, P.; Bhata, H.L. Growth of InBi_xSb_{1-x} films on GaAs (001) substrates using liquid phase epitaxy and their characterization. *J. Cryst. Growth* **2002**, *241*, 171–176. [[CrossRef](#)]
182. Ma, K.Y.; Fang, Z.M.; Cohen, R.M.; Stringfellow, G.B. OMVPE growth and characterization of Bi-containing III–V alloys. *J. Cryst. Growth* **1991**, *107*, 416–421. [[CrossRef](#)]
183. Lee, J.J.; Kim, J.D.; Razeghi, M. Growth and characterization of InSbBi for long wavelength infrared photodetectors. *Appl. Phys. Lett.* **1997**, *70*, 3266. [[CrossRef](#)]
184. Wagener, M.C.; Kroon, R.E.; Botha, J.R.; Leitch, A.W.R. Analysis of secondary phases in InSbBi thin films. *Phys. B-Condens. Matter* **1999**, *273–274*, 919–922. [[CrossRef](#)]

185. Du, Q.; Alperin, J.; Wang, W.I. Molecular beam epitaxial growth of GaInSbBi for infrared detector applications. *J. Cryst. Growth* **1997**, *175/176*, 849–852. [[CrossRef](#)]
186. Das, S.K.; Das, T.D.; Dhar, S.; de la Mare, M.; Krier, A. Near infrared photoluminescence observed in dilute GaSbBi alloys grown by liquid phase epitaxy. *Infrared Phys. Technol.* **2012**, *55*, 156–160. [[CrossRef](#)]
187. Rajpalke, M.K.; Linhart, W.M.; Birkett, M.; Yu, K.M.; Scanlon, D.O.; Buckeridge, J.; Jones, T.S.; Ashwin, M.J.; Veal, T.D. Growth and properties of GaSbBi alloys. *Appl. Phys. Lett.* **2013**, *103*, 142106. [[CrossRef](#)]
188. Rajpalke, M.K.; Linhart, W.M.; Yu, K.M.; Jones, T.S.; Ashwin, M.J.; Veal, T.D. Bi flux-dependent MBE growth of GaSbBi alloys. *J. Cryst. Growth* **2015**, *425*, 241–244. [[CrossRef](#)]
189. Polak, M.P.; Scharoch, P.; Kudrawiec, R.; Kopaczek, J.; Winiarski, M.J.; Linhart, W.M.; Rajpalke, M.K.; Yu, K.M.; Jones, T.S.; Ashwin, M.J. Theoretical and experimental studies of electronic band structure for GaSb_{1-x}Bi_x in the dilute Bi regime. *J. Phys. D* **2014**, *47*, 355107.
190. Kopaczek, J.; Kudrawiec, R.; Linhart, W.M.; Rajpalke, M.K.; Yu, K.M.; Jones, T.S.; Ashwin, M.J.; Misiewicz, J.; Veal, T.D. Temperature dependence of the band gap of GaSb_{1-x}Bi_x alloys with $0 < x \leq 0.042$ determined by photorefectance. *Appl. Phys. Lett.* **2013**, *103*, 261907.
191. Kopaczek, J.; Kudrawiec, R.; Linhart, W.; Rajpalke, M.; Jones, T.; Ashwin, M.; Veal, T. Low- and high-energy photoluminescence from GaSb_{1-x}Bi_x with $0 < x \leq 0.042$. *Appl. Phys. Express* **2014**, *7*, 111202.
192. Francoeur, S.; Seong, M. J.; Mascarenhas, A.; Tixier, S.; Adamczyk, M.; Tiedje, T. Band gap of GaAs_{1-x}Bi_x, $0 < x < 3.6\%$. *Appl. Phys. Lett.* **2003**, *82*, 3874.
193. Wei, P.; Tixier, S.; Chicoine, M.; Francoeur, S.; Mascarenhas, A.; Tiedje, T.; Schiettekatte, F. Ion beam characterization of GaAs_{1-x-y}N_xBi_y epitaxial layers. *Nucl. Instrum. Methods Phys. Res. Sect. B* **2004**, *219–220*, 671–675. [[CrossRef](#)]
194. Yoshimoto, M.; Huang, W.; Takehara, Y.; Saraie, J.; Chayahara, A.; Horino, Y.; Oe, K. New semiconductor GaNAsBi alloy grown by molecular beam epitaxy. *Jpn. J. Appl. Phys.* **2004**, *43*, L845–L847. [[CrossRef](#)]
195. Bushell, Z.L.; Ludewig, P.; Knaub, N.; Batool, Z.; Hild, K.; Stolz, W.; Sweeney, S.J.; Volz, K. Growth and characterisation of Ga(NAsBi) alloy by metal-organic vapour phase epitaxy. *J. Cryst. Growth* **2014**, *396*, 79–84. [[CrossRef](#)]
196. Denton, A.R.; Ashcroft, N.W. Vegard's law. *Phys. Rev. A* **1991**, *43*, 3161–3164. [[CrossRef](#)] [[PubMed](#)]
197. Yoshimoto, M.; Huang, W.; Feng, G.; Oe, K. New semiconductor alloy GaNAsBi with temperature-insensitive bandgap. *Phys. Status Solidi (b)* **2006**, *243*, 1421–1425. [[CrossRef](#)]
198. Beaton, D.A.; Ptak, A.J.; Alberi, K.; Mascarenhas, A. Quaternary bismide alloy lattice matched to GaAs. *J. Cryst. Growth* **2012**, *351*, 37–40. [[CrossRef](#)]
199. Aslan, M.; Yalcin, B. G.; Ustundag, M.; Bagci, S. Theoretical calculations on structural and electronic properties of BGaAsBi alloys. *Eur. Phys. J. B* **2015**, *88*, 1–4. [[CrossRef](#)]
200. Groenert, M.E.; Averbeck, R.; Hösler, W.; Schuster, M.; Riechert, H. Optimized growth of BGaAs by molecular beam epitaxy. *J. Cryst. Growth* **2004**, *264*, 123–127. [[CrossRef](#)]
201. Hoke, W.E. Molecular-beam epitaxial growth of boron-doped GaAs films. *J. Vac. Sci. Technol. B* **1993**, *11*, 902. [[CrossRef](#)]
202. Wu, X.; Chen, X.; Pan, W.; Wang, P.; Zhang, L.; Li, Y.; Wang, H.; Wang, K.; Shao, J.; Wang, S. Anomalous photoluminescence in InP_{1-x}Bi_x. *Sci. Rep.* **2016**, *6*, 27867. [[CrossRef](#)] [[PubMed](#)]
203. Sales, D.L.; Guerrero, E.; Rodrigo, J.F.; Galindo, P.L.; Yáñez, A.; Shafi, M.; Khatab, A.; Mari, R.H.; Henini, M.; Novikov, S.; et al. Distribution of bismuth atoms in epitaxial GaAsBi. *Appl. Phys. Lett.* **2011**, *98*, 101902. [[CrossRef](#)]
204. Song, Y.; Wang, S.; Saha Roy, I.; Shi, P.; Hallen, A. Growth of GaSb_{1-x}Bi_x by molecular beam epitaxy. *J. Vac. Sci. Technol. B* **2012**, *30*, 02B114.
205. Das, T.D. The effect of Bi composition on the properties of InP_{1-x}Bi_x grown by liquid phase epitaxy. *J. Appl. Phys.* **2014**, *115*, 173107. [[CrossRef](#)]
206. Takehara, Y.; Yoshimoto, M.; Huang, W.; Saraie, J.; Oe, K.; Chayahara, A.; Horino, Y. Lattice distortion of GaAsBi alloy grown on GaAs by molecular beam epitaxy. *Jpn. J. Appl. Phys.* **2006**, *45*, 67–69. [[CrossRef](#)]
207. Kunzer, M.; Jost, W.; Kaufmann, U.; Hobgood, H.M.; Thomas, R.N. Identification of the Bi_{Ga} heteroantisite defect in GaAs:Bi. *Phys. Rev. B* **1993**, *48*, 4437–4441. [[CrossRef](#)]
208. Ferhat, M.; Zaoui, A. Do all III-V compounds have the zinc-blende or wurtzite ground state structure? *Appl. Phys. Lett.* **2006**, *88*, 161902. [[CrossRef](#)]
209. Mascarenhas, A. *Spontaneous Ordering in Semiconductor Alloys*; Springer: Berlin, Germany, 2002.

210. Wu, M.; Luna, E.; Puustinen, J.; Guina, M.; Trampert, A. Observation of atomic ordering of triple-period-A and -B type in GaAsBi. *Appl. Phys. Lett.* **2014**, *105*, 041602. [[CrossRef](#)]
211. Reyes, D.F.; Bastiman, F.; Hunter, C.; Sales, D.L.; Sanchez, A.M.; David, J.P.R.; González, D. Bismuth incorporation and the role of ordering in GaAsBi/GaAs structures. *Nanoscale Res. Lett.* **2014**, *9*, 23. [[CrossRef](#)] [[PubMed](#)]
212. Verma, P.; Oe, K.; Yamada, M.; Harima, H.; Herms, M.; Irmer, G. Raman Studies on GaAs_{1-x}Bi_x and InAs_{1-x}Bi_x. *J. Appl. Phys.* **2001**, *89*, 1657. [[CrossRef](#)]
213. Janotti, A.; Wei, S.-H.; Zhang, S.B. Theoretical study of the effects of isovalent coalloing of Bi and N in GaAs. *Phys. Rev. B* **2002**, *65*, 115203. [[CrossRef](#)]
214. Alberi, K.; Wu, J.; Walukiewicz, W.; Yu, K.M.; Dubon, O.D.; Watkins, S.P.; Wang, C.X.; Liu, X.; Cho, Y.J.; Furdyna, J. Valence-band anticrossing in mismatched III-V semiconductor alloys. *Phys. Rev. B* **2007**, *75*, 045203. [[CrossRef](#)]
215. Pettinari, G.; Polimeni, A.; Capizzi, M.; Blokland, J.H.; Christianen, P.C.M.; Maan, J.C.; Young, E.C.; Tiedje, T. Influence of bismuth incorporation on the valence and conduction band edges of GaAs_{1-x}Bi_x. *Appl. Phys. Lett.* **2008**, *92*, 262105. [[CrossRef](#)]
216. Pettinari, G.; Polimeni, A.; Blokland, J.H.; Trotta, R.; Christianen, P.C.M.; Capizzi, M.; Maan, J.C.; Lu, X.; Young, E.C.; Tiedje, T. Compositional dependence of the exciton reduced mass in GaAs_{1-x}Bi_x ($x = 0\%–10\%$). *Phys. Rev. B* **2010**, *81*, 235211. [[CrossRef](#)]
217. Lu, X.; Beaton, D.A.; Lewis, R.B.; Tiedje, T.; Zhang, Y. Composition dependence of photoluminescence of GaAs_{1-x}Bi_x alloys. *Appl. Phys. Lett.* **2009**, *95*, 041903. [[CrossRef](#)]
218. Mohmad, A.R.; Bastiman, F.; Hunter, C.J.; Richards, R.D.; Sweeney, S.J.; Ng, J.S.; David, J.P.R.; Majlis, B.Y. Localization effects and band gap of GaAsBi alloys. *Phys. Status Solidi (b)* **2014**, *251*, 1276–1281. [[CrossRef](#)]
219. Kudrawiec, R.; Kopaczek, J.; Sitarek, P.; Misiewicz, J.; Henini, M.; Novikov, S.V. Unusual broadening of E_0 and $E_0 + \Delta_{SO}$ transitions in GaAsBi studied by electromodulation spectroscopy. *J. Appl. Phys.* **2012**, *111*, 066103. [[CrossRef](#)]
220. Pettinari, G.; Patanè, A.; Polimeni, A.; Capizzi, M.; Lu, X.; Tiedje, T. Bi-induced p-type conductivity in nominally undoped Ga(AsBi). *Appl. Phys. Lett.* **2012**, *100*, 092109. [[CrossRef](#)]
221. Kini, R.N.; Ptak, A.J.; Fluegel, B.; France, R.; Reedy, R.C.; Mascarenhas, A. Effect of Bi alloying on the hole transport in the dilute bismide alloy GaAs_{1-x}Bi_x. *Phys. Rev. B* **2011**, *83*, 075307. [[CrossRef](#)]
222. Cooke, D.G.; Hegmann, F.A.; Young, E.C.; Tiedje, T. Electron mobility in dilute GaAs bismide and nitride alloys measured by time-resolved terahertz spectroscopy. *Appl. Phys. Lett.* **2006**, *89*, 122103. [[CrossRef](#)]
223. Fahy, S.; Lindsay, A.; Ouerdane, H.; O'Reilly, E.P. Alloy scattering of n-type carriers in GaN_xAs_{1-x}. *Phys. Rev. B* **2006**, *74*, 035203. [[CrossRef](#)]
224. Pettinari, G.; Polimeni, A.; Capizzi, M.; Engelkamp, H.; Christianen, P.C.M.; Maan, J.C.; Patanè, A.; Tiedje, T. Effects of Bi incorporation on the electronic properties of GaAs: Carrier masses, hole mobility, and Bi-induced acceptor states. *Phys. Status Solidi (b)* **2013**, *250*, 779–786. [[CrossRef](#)]
225. Gelczuk, Ł.; Stokowski, H.; Kopaczek, J.; Zhang, L.; Li, Y.; Wang, K.; Wang, P.; Wang, S.; Kudrawiec, R. Bi-induced acceptor level responsible for partial compensation of native free electron density in InP_{1-x}Bi_x dilute bismide alloys. *J. Phys. D* **2016**, *49*, 115107. [[CrossRef](#)]
226. Schäfer, W.; Wegener, M. *Semiconductor Optics and Transport Phenomena*; Springer: Berlin, Germany, 2013.
227. Gilliland, G.D. Photoluminescence spectroscopy of crystalline semiconductors. *Mater. Sci. Eng.* **1997**, *18*, 99–440. [[CrossRef](#)]
228. Shao, J.; Lu, W.; Lü, X.; Yue, F.; Li, Z.; Guo, S.; Chu, J. Erratum: “Modulated photoluminescence spectroscopy with a step-scan Fourier transform infrared spectrometer” [Review of Scientific Instruments **2006**, *77*, 063104]. *Rev. Sci. Instrum.* **2007**, *78*, 029901. [[CrossRef](#)]
229. Shao, J.; Lu, W.; Tsen, G.K.O.; Guo, S.; Dell, J.M. Mechanisms of infrared photoluminescence in HgTe/HgCdTe superlattice. *J. Appl. Phys.* **2012**, *112*, 063512. [[CrossRef](#)]
230. Shao, J.; Lü, X.; Guo, S.; Lu, W.; Chen, L.; Wei, Y.; Yang, J.; He, L.; Chu, J. Impurity levels and bandedge electronic structure in as-grown arsenic-doped HgCdTe by infrared photoreflectance spectroscopy. *Phys. Rev. B* **2009**, *80*, 155125. [[CrossRef](#)]
231. Shao, J.; Lu, W.; Sadeghi, M.; Lü, X.; Wang, S.M.; Ma, L.; Larsson, A. Evolution of valence-band alignment with nitrogen content in GaNAs/GaAs single quantum wells. *Appl. Phys. Lett.* **2008**, *93*, 031904. [[CrossRef](#)]

232. Chen, X.; Jung, J.; Qi, Z.; Zhu, L.; Park, S.; Zhu, L.; Yoon, E.; Shao, J. Infrared photoreflectance investigation of resonant levels and band edge structure in InSb. *Opt. Lett.* **2015**, *40*, 5295–5298. [[CrossRef](#)] [[PubMed](#)]
233. Shao, J.; Chen, L.; Lü, X.; Lu, W.; He, L.; Guo, S.; Chu, J. Realization of photoreflectance spectroscopy in very-long wave infrared of up to 20 μm . *Appl. Phys. Lett.* **2009**, *95*, 041908. [[CrossRef](#)]
234. Shao, J.; Lu, W.; Yue, F.; Lu, X.; Huang, W.; Li, Z.; Guo, S.; Chu, J. Photoreflectance spectroscopy with a step-scan Fourier-transform infrared spectrometer: Technique and applications. *Rev. Sci. Instrum.* **2007**, *78*, 013111. [[CrossRef](#)] [[PubMed](#)]
235. Huang, K.T.; Chiu, C.T.; Cohen, R.M.; Stringfellow, G.B. InAsBi alloys grown by organometallic vapor phase epitaxy. *J. Cryst. Growth* **1993**, *134*, 29–34. [[CrossRef](#)]
236. Pačebutas, V.; Bertulis, K.; Dapkus, L.; Aleksejenko, G.; Krotkus, A.; Yu, K.M.; Walukiewicz, W. Characterization of low-temperature molecular-beam-epitaxy grown GaBiAs layers. *Semicond. Sci. Technol.* **2007**, *22*, 819–823. [[CrossRef](#)]
237. Chen, X.-R.; Song, Y.-X.; Zhu, L.-Q.; Qi, Z.; Zhu, L.; Zha, F.-X.; Guo, S.-L.; Wang, S.-M.; Shao, J. Bismuth effects on electronic levels in GaSb(Bi)/AlGaSb quantum wells probed by infrared photoreflectance. *Chin. Phys. Lett.* **2015**, *32*, 067301. [[CrossRef](#)]
238. Kudrawiec, R.; Kopaczek, J.; Misiewicz, J.; Walukiewicz, W.; Petropoulos, J.P.; Zhong, Y.; Dongmo, P.B.; Zide, J.M.O. Temperature dependence of E_0 and $E_0 + \Delta_{SO}$ transitions in $\text{In}_{0.53}\text{Ga}_{0.47}\text{Bi}_x\text{As}_{1-x}$ alloys studied by photoreflectance. *J. Appl. Phys.* **2012**, *112*, 113508. [[CrossRef](#)]
239. Pettinari, G.; Capizzi, M.; Polimeni, A. Carrier masses and band-gap temperature sensitivity in Ga(AsBi) alloys. *Semicond. Sci. Technol.* **2015**, *30*, 094002. [[CrossRef](#)]
240. Fitouri, H.; Essouda, Y.; Zaied, I.; Rebey, A.; El Jani, B. Photoreflectance and photoluminescence study of localization effects in GaAsBi alloys. *Opt. Mater.* **2015**, *42*, 67–71. [[CrossRef](#)]
241. Mohmad, A.R.; Bastiman, F.; Hunter, C.J.; Harun, F.; Reyes, D.F.; Sales, D.L.; Gonzalez, D.; Richards, R.D.; David, J.P.R.; Majlis, B.Y. Bismuth concentration inhomogeneity in GaAsBi bulk and quantum well structures. *Semicond. Sci. Technol.* **2015**, *30*, 094018. [[CrossRef](#)]
242. Beaton, D.A.; Mascarenhas, A.; Alberi, K. Insight into epitaxy growth of high optical quality $\text{GaAs}_{1-x}\text{Bi}_x$. *J. Appl. Phys.* **2015**, *118*, 235701. [[CrossRef](#)]
243. Mohmad, A.R.; Bastiman, F.; Hunter, C.J.; Ng, J.S.; Sweeney, S.J.; David, J.P.R. The effect of Bi composition to the optical quality of $\text{GaAs}_{1-x}\text{Bi}_x$. *Appl. Phys. Lett.* **2011**, *99*, 042107. [[CrossRef](#)]
244. Gu, Y.; Zhang, Y.G.; Chen, X.Y.; Xi, S.P.; Du, B.; Ma, Y.J. Effect of bismuth surfactant on InP-based highly strained InAs/InGaAs triangular quantum wells. *Appl. Phys. Lett.* **2015**, *107*, 212104. [[CrossRef](#)]
245. Oe, K. Characteristics of semiconductor alloy $\text{GaAs}_{1-x}\text{Bi}_x$. *Jpn. J. Appl. Phys.* **2002**, *41*, 2801–2806. [[CrossRef](#)]
246. Imhof, S.; Thränhardt, A.; Chernikov, A.; Koch, M.; Köster, N.S.; Kolata, K.; Chatterjee, S.; Koch, S.W.; Lu, X.; Johnson, S.R.; et al. Clustering effects in Ga(AsBi). *Appl. Phys. Lett.* **2010**, *96*, 131115. [[CrossRef](#)]
247. Shakfa, M.K.; Wiemer, M.; Ludewig, P.; Jandieri, K.; Volz, K.; Stolz, W.; Baranovskii, S.D.; Koch, M. Thermal quenching of photoluminescence in Ga(AsBi). *J. Appl. Phys.* **2015**, *117*, 025709. [[CrossRef](#)]
248. Seonga, M.J.; Francoeura, S.; Yoon, S.; Mascarenhas, A.; Tixierb, S.; Adamczyk, M.; Tiedje, T. Bi-induced vibrational modes in GaAsBi. *Superlattices Microstructures* **2005**, *37*, 394–400. [[CrossRef](#)]
249. Marko, I.P.; Jin, S.R.; Hild, K.; Batool, Z.; Bushell, Z.L.; Ludewig, P.; Stolz, W.; Volz, K.; Butkutė, R.; Pačebutas, V.; et al. Properties of hybrid MOVPE/MBE grown GaAsBi/GaAs based near-infrared emitting quantum well lasers. *Semicond. Sci. Technol.* **2015**, *30*, 094008. [[CrossRef](#)]
250. Lewis, R.B.; Beaton, D.A.; Lu, X.; Tiedje, T. $\text{GaAs}_{1-x}\text{Bi}_x$ light emitting diodes. *J. Cryst. Growth* **2009**, *311*, 1872–1875. [[CrossRef](#)]
251. Zvonkov, B.N.; Karpovich, I.A.; Baidus, N.V.; Filatov, D.O.; Morozov, S.V.; Gushina, Y.Y. Surfactant effect of bismuth in the MOVPE growth of the InAs quantum dots on GaAs. *Nanotechnology* **2000**, *11*, 221–226. [[CrossRef](#)]
252. Reyes, D.F.; González, D.; Bastiman, F.; Dominguez, L.; Hunter, C.J.; Guerrero, E.; Roldan, M.A.; Mayoral, A.; David, J.P.R.; Sales, D.L. Photoluminescence enhancement of InAs(Bi) quantum dots by Bi clustering. *Appl. Phys. Express* **2013**, *6*, 042103. [[CrossRef](#)]
253. Dasika, V.D.; Krivoy, E.M.; Nair, H.P.; Maddox, S.J.; Park, K.W.; Jung, D.; Lee, M.L.; Yu, E.T.; Bank, S.R. Increased InAs quantum dot size and density using bismuth as a surfactant. *Appl. Phys. Lett.* **2014**, *105*, 253104. [[CrossRef](#)]

254. Essouda, Y.; Fitouri, H.; Boussaha, R.; Elayech, N.; Rebey, A.; Jani, B.E. Bismuth catalyzed growth of GaAsBi nanowires by metalorganic vapor phase epitaxy. *Mater. Lett.* **2015**, *152*, 298–301. [[CrossRef](#)]
255. Shimomura, K.; Kamiya, I. Strain engineering of quantum dots for long wavelength emission: Photoluminescence from self-assembled InAs quantum dots grown on GaAs(001) at wavelengths over 1.55 μm . *Appl. Phys. Lett.* **2015**, *106*, 082103. [[CrossRef](#)]
256. Bimberg, D. Quantum dots for lasers, amplifiers and computing. *J. Phys. D* **2005**, *38*, 2055–2058. [[CrossRef](#)]
257. Copel, M.; Reuter, M.C.; Kaxiras, E.; Tromp, R.M. Surfactants in epitaxial growth. *Phys. Rev. Lett.* **1989**, *63*, 632–635. [[CrossRef](#)] [[PubMed](#)]
258. Lyman, P.F.; Bedzyk, M.J. Surfactant-mediated epitaxy of metastable SnGe alloys. *Appl. Phys. Lett.* **1996**, *69*, 978–980. [[CrossRef](#)]
259. Ciatto, G.; Young, E.C.; Glas, F.; Chen, J.; Mori, R.A.; Tiedje, T. Spatial correlation between Bi atoms in dilute $\text{GaAs}_{1-x}\text{Bi}_x$: From random distribution to Bi pairing and clustering. *Phys. Rev. B* **2008**, *78*, 035325. [[CrossRef](#)]
260. Sweeney, S.J.; Adams, A.R.; Silver, M.; O'Reilly, E.P.; Watling, J.R.; Walker, A.B.; Thijs, P.J.A. Dependence of threshold current on QW position and on pressure in 1.5 μm InGaAs(P) lasers. *Phys. Status Solidi (b)* **1999**, *211*, 525–531. [[CrossRef](#)]
261. Hunter, C.J.; Bastiman, F.; Mohmad, A.R.; Richards, R.; Ng, J.S.; Sweeney, S.J.; David, J.P. Absorption characteristics of diodes in the near-infrared. *IEEE Photonics Technol. Lett.* **2012**, *24*, 2191–2194. [[CrossRef](#)]
262. Tominaga, Y.; Oe, K.; Yoshimoto, M. Low temperature dependence of oscillation wavelength in $\text{GaAs}_{1-x}\text{Bi}_x$ laser by photo-pumping. *Appl. Phys. Express* **2010**, *3*, 062201. [[CrossRef](#)]
263. Fuyuki, T.; Yoshioka, R.; Yoshida, K.; Yoshimoto, M. Long-wavelength emission in photo-pumped $\text{GaAs}_{1-x}\text{Bi}_x$ laser with low temperature dependence of lasing wavelength. *Appl. Phys. Lett.* **2013**, *103*, 202105. [[CrossRef](#)]
264. Fuyuki, T.; Yoshida, K.; Yoshioka, R.; Yoshimoto, M. Electrically pumped room-temperature operation of $\text{GaAs}_{1-x}\text{Bi}_x$ laser diodes with low-temperature dependence of oscillation wavelength. *Appl. Phys. Express* **2014**, *7*, 082101. [[CrossRef](#)]
265. Marko, I. P.; Ludewig, P.; Bushell, Z. L.; Jin, S. R.; Hild, K.; Batool, Z.; Reinhard, S.; Nattermann, L.; Stolz, W.; Volz, K.; Sweeney, S.J. Physical properties and optimization of GaBiAs/(Al)GaAs based near-infrared laser diodes grown by MOVPE with up to 4.4% Bi. *J. Phys. D* **2014**, *47*, 345103. [[CrossRef](#)]
266. Kim, H.; Forghani, K.; Guan, Y.; Luo, G.; Anand, A.; Morgan, D.; Kuech, T.F.; Mawst, L.J.; Lingley, Z.R.; Foran, B.J.; et al. Strain-compensated $\text{GaAs}_{1-y}\text{Py}/\text{GaAs}_{1-z}\text{Biz}/\text{GaAs}_{1-y}\text{Py}$ quantum wells for laser applications. *Semicond. Sci. Technol.* **2015**, *30*, 094011. [[CrossRef](#)]
267. Sandall, I.C.; White, B.; Richards, R.; Mendes, D.; David, J.P.R.; Tan, C.H. Demonstration of InAsBi photoresponse beyond 3.5 μm . *Appl. Phys. Lett.* **2014**, *104*, 171109. [[CrossRef](#)]
268. Gu, Y.; Zhang, Y.G.; Chen, X.Y.; Ma, Y.J.; Xi, S.P.; Du, B.; Li, H. Nearly lattice-matched short-wave infrared InGaAsBi detectors on InP. *Appl. Phys. Lett.* **2016**, *108*, 032102. [[CrossRef](#)]
269. Arlauskas, A.; Svidovsky, P.; Bertulis, K.; Adomavičius, R.; Krotkus, A. GaAsBi photoconductive terahertz detector sensitivity at long excitation wavelengths. *Appl. Phys. Express* **2012**, *5*, 022601. [[CrossRef](#)]
270. Pačebutas, V.; Urbanowicz, A.; Cicėnas, P.; Stanionytė, S.; Bičiūnas, A.; Nevinskas, I.; Krotkus, A. Growth and characterization of quaternary (GaIn)(AsBi) layers for optoelectronic terahertz detector applications. *Semicond. Sci. Technol.* **2015**, *30*, 094012. [[CrossRef](#)]
271. Thomas, T.; Mellor, A.; Hylton, N.P.; Führer, M.; Alonso-Álvarez, D.; Braun, A.; Ekins-Daukes, N.J.; David, J.P.R.; Sweeney, S.J. Requirements for a GaAsBi 1 eV sub-cell in a GaAs-based multi-junction solar cell. *Semicond. Sci. Technol.* **2015**, *30*, 094010. [[CrossRef](#)]
272. Dongmo, P.; Zhong, Y.; Attia, P.; Bomberger, C.; Cheaito, R.; Ihlefeld, J.F.; Hopkins, P.E.; Zide, J. Enhanced room temperature electronic and thermoelectric properties of the dilute bismuthide InGaBiAs. *J. Appl. Phys.* **2012**, *112*, 093710. [[CrossRef](#)]

